Stony Brook University

Nonlinear Analyses of Functional MRI Time-Series in Brain-Based Disorders

A Dissertation Presented

by

Sanja Nedic

to

The Graduate School

in Partial Fulfillment of the

Requirements

for the Degree of

Doctor of Philosophy

in

Biomedical Engineering

Stony Brook University

August 2017

Stony Brook University

The Graduate School

Sanja Nedic

We, the dissertation committee for the above candidate for the

Doctor of Philosophy degree, hereby recommend

acceptance of this dissertation.

Dr. Lilianne R. Mujica-Parodi - Dissertation Advisor
Associate Professor, Biomedical Engineering

Dr. Paul Vaska - Chairperson of Defense
Professor, Biomedical Engineering

Dr. Helmut Strey
Associate Professor, Biomedical Engineering

Dr. Jin Wang
Professor, Chemistry

This dissertation is accepted by the Graduate School

Charles Taber

Dean of the Graduate School

Abstract of the Dissertation

Nonlinear Analyses of Functional MRI Time-Series in Brain-Based Disorders

by

Sanja Nedic

Doctor of Philosophy

in

Biomedical Engineering

Stony Brook University

2017

Functional magnetic resonance imaging (fMRI) is a non-invasive neuroimaging modality used to measure brain activity in vivo, capable of providing three-dimensional coverage of the brain at a high spatial resolution. While fMRI has advanced our understanding of the brain, it has had limited applications in medical practice due to 1) analytic approaches predominantly focused on either contrasting signal amplitudes from clearly defined conditions in simplistic task stimuli (to localize "activations") or on computing time-course cross-correlations between pairs of brain regions to infer the strength of functional "connectivity" between them in resting-state fMRI studies, and 2) low signal-to-noise ratio/difficulty separating signal due to relevant neuronal fluctuations from signal due to noise. Consequently, research findings typically need to be averaged over many trials and subjects. On the other hand, clinical diagnostics are necessarily based upon a single subject, thus requiring high quality data and methods sensitive to abnormalities in network dynamics.

To address the first issue, work presented here is driven by the hypothesis that the most sensitive biomarker of dysregulation may not be the amplitude of activation or strength of connections between two regions, but rather the complexity of the signal, reflecting the underlying (deviations in) dynamics. We introduce and apply an entropic measure of regulation and feedback (the autocorrelation function) to identify focal regions in patients with medication-resistant epilepsy. Precise localization of foci is crucial for successful surgery. To address the second issue, we introduce a new quantitative measure to accurately assess the integrity of fMRI time-series – *signal fluctuation sensitivity (SFS)*. We show that SFS correlates with time-series integrity and that higher SFS is associated with enhanced sensitivity to detection of known local and long-range connections in resting-state (task-free) fMRI. We further show that this measure reliably identifies task-induced activations in three different tasks employing highly complex naturalistic stimuli, which still represent a challenge from the data-analysis perspective. Finally, we incorporate high quality fMRI data with machine learning to build models capable of predicting subjects' dynamic state of mind from fMRI signals of relevant brain networks at an individual-subject level.

Table of Contents

Chapter 1 General Introduction 1

Chapter 2 Using Network Dynamic fMRI for Detection of Epileptogenic Foci 5

Abstract 5
Introduction 6
Methods 10
Participants 10
Data Acquisition 11
fMRI Data Preprocessing 11
Autocorrelation Function (ACF) Method 13
Classification 15
Functional Connectivity 15
Graph-Theoretic Analyses 16
Results 16
Left Temporal Lobe Epilepsy Patients Show Constrained Dynamics of Left Temporal Pole 16
Classification Analyses Achieve 100% Accuracy in Distinguishing Patients vs. Controls 17
Constrained Dynamics are Linked with Locally Dense/Long-Range Sparse Connectivity 19
Connectivity Abnormalities Correlate with Epilepsy Duration 20
Connectivity Abnormalities Correlate with Verbal Memory Task Performance 21
Clusters with Constrained Dynamics Form a Less Efficient Network in Patients 22
Discussion 22
Limitations and Future Directions 25
Conclusions 26

Chapter 3 Signal Fluctuation Sensitivity: An Improved Metric for Optimizing Detection of Resting-State fMRI Networks 27

Abstract 27
Introduction 28
Methods 30
Using the Dynamic Phantom to Test SFS and tSNR 31
Human Scanning 33
Computation of SFS, tSNR, ALFF, ReHo and Long-Range (mPFC-PCC) Connectivity 35
Results 36
Dynamic Phantom Assessment of SFS vs tSNR in Predicting Dynamic Integrity 36
Human Subjects Assessment of SFS vs. tSNR in Detecting Resting-State Connectivity 38
SFS and tSNR Values Between Acquisition Sets 41
Discussion 44

Chapter 4 Signal Fluctuation Sensitivity Identifies Brain Activity in Naturalistic-Task fMRI 47

Abstract 47
Introduction 48
Methods 52
Overview 52
Participants and Task Descriptions 53
fMRI Acquisition Parameters and Data Preprocessing 54

Computation of SFS, Sliding-Window SFS, and Statistical Analyses on SFS Maps 56
Inter-Subject Correlations 57
Independent Component Analysis 57
Results 58
SFS Identifies Task-Related Activations 58
Brain Areas Identified via ISC Analyses Match Those Found via SFS Analyses 63
ICA Points to Increased Engagement of Visual Networks During Movie-Watching, but no Individual IC Time-Courses Track the Emotional Contents of LOST 64
Discussion 66

Chapter 5 Modeling Dynamic State of Mind: Cybersecurity Study 71
Introduction 71
Methods 72
Task Description 72
Participants 73
MRI Data Acquisition Parameters and Preprocessing 74
Independent Component Analysis 74
Bayesian Solver – Optimal Strategy using Bayes' Rule 77
Predictive Modeling of Subjects' Behavior 78
Logistic Regression 83
Feature Selection 84
Results and Discussion 84
Brain Data are Predictive of Subjects' State of Mind 84
Feature Selection Identifies Most Informative Networks 88
Future Directions 89

List of Figures

Figure 2-1: Autocorrelation decay rates (ACF b) are altered close to presumed focal regions.... 17
Figure 2-2: Autocorrelation decay rates classify patients with epilepsy with 100% accuracy..... 19
Figure 2-3: Seed-to-voxel connectivity of the ACF-identified left temporal lobe cluster is significantly different in patients. 20
Figure 2-4: Abnormalities in functional connectivity correlate with patients' scores on the Logical Memory Delayed Recall task. 22
Figure 3-1: Dynamic phantom results show that dynamic fidelity positively correlates with signal fluctuation sensitivity (SFS) and negatively correlates with classical temporal signal to noise ratio (tSNR). 39
Figure 3-2: Local and long-range functional connectivity across the default mode network positively correlates with SFS and negatively correlates with tSNR. 42
Figure 3-3: SFS distributions across the brain illustrate qualitative differences in sensitivity between acquisition strategies. 43
Figure 4-1: SFS identifies regions active during MOVIE and TRUST. 60
Figure 4-2: SFS identifies regions active during LOST. 63
Figure 4-3: Intersubject correlations (ISCs) identify regions co-activated across subjects during MOVIE and LOST. 64
Figure 4-4: ICA and follow-up statistical tests on spatial maps of identified components show significant modification of resting-state networks by task. 67
Figure 5-1: Cybersecurity Enterprises Task 73
Figure 5-2: Accuracy at each trial for representative subjects with good and suboptimal performance, color-coded by their state of mind. 79
Figure 5-3: Bayesian Conviction for representative subjects with good and suboptimal performance, color-coded by their state of mind. 79
Figure 5-4: Subjects who make choices closer to those of the Bayesian solver perform better... 81
Figure 5-5:Individual-subject models predict state of mind from behavioral and brain data..... 86
Figure 5-6: Common model predicts state of mind from behavioral and brain data. 87
Figure 5-7:Univariate feature selection points to relative importance of features..... 88
Figure 5-8: Top three independent components predict state of mind at accuracy comparable to that achieved when using all components. 91

List of Tables

Table 2-1: Demographic and clinical information. 12
Table 2-2: List of regions showing significantly different values of ACF b in patients relative to controls. 18
Table 2-3: List of regions showing significantly different functional connectivity to the ACF-identified left temporal pole cluster. 21
Table 3-1: Acquisition parameters for the nine dynamic phantom scans. 32
Table 3-2: Dynamic fidelity for dynamic phantom scans. 38
Table 4-1: List of regions showing significantly different SFS values during task relative to rest for MOVIE and LOST tasks. 61
Table 4-2: List of regions showing significantly different SFS values during task relative to rest for the TRUST task. 62
Table 5-1: Description of components identified via ICA of CSE task. 76
Table 5-2: Summary of performance metrics for individual-subject and common classifiers. 85

List of Abbreviations

ACC	anterior cingulate cortex
ACF	autocorrelation function
ALFF	amplitude of low frequency fluctuations
ANOVA	analysis of variance
BA	Brodmann area
BOLD	blood oxygen level dependent
CBZ	carbamazepine
Ch	channel
CLB	clobazam
CNR	contrast to noise ratio
CSF	cerebrospinal fluid
CO	comorbid
CSE	cybersecurity enterprises
DCM	dynamic causal modeling
DMN	default mode network
ECoG	electrocorticography
EEG	electroencephalography
EPI	echo planar imaging
FWHM	full width at half maximum
FN	false negatives
FP	false positives
GAD	generalized anxiety disorder
GLM	general linear model
HA	hippocampal atrophy
HC	healthy controls
HRF	hemodynamic response function
HS	hippocampal sclerosis
ICA	independent component analysis
IEDs	interictal discharges

IFG	inferior frontal gyrus
ISC	inter subject correlation
fMRI	functional magnetic resonance imaging
LM-DR	logical memory – delayed recall
LLP	left lateral parietal cortex
LTG	lamotrigine
LTLE	left temporal lobe epilepsy
MCC	medial cingulate cortex
MDD	major depressive disorder
MDL	minimum description length
MEG	magnetoencephalography
MNI	Montreal Neurological Institute
mPFC	medial prefrontal cortex
MRI	magnetic resonance imaging
MTLE	mesial temporal lobe epilepsy
MU	monetary units
n.s.	not significant
OFC	orbitofrontal cortex
OT	oxytocin
OXC	oxcarbazepine
PB	phenobarbital
PCA	principal component analysis
PCC	posterior cingulate cortex
PET	positron emission tomography
PHT	phenytoin
PL	placebo
PSSI	power spectrum scale invariance
ReHo	regional homogeneity
RMS	root mean square
ROI	region of interest
RLP	right lateral parietal cortex

SD	standard deviation
SFS	signal fluctuation sensitivity
tSNR	temporal signal to noise ratio
TN	true negatives
TP	true positives
TPM	topiramate,
TR	repetition time
VPA	valproic acid

Acknowledgments

I would like to express my utmost gratitude to my advisor, Dr. Lilianne Mujica-Parodi, for introducing me to the field of functional neuroimaging and for her guidance, support and endless encouragement throughout the last six years. Her passion for scientific research has been an inspiration. I would also like to thank Dr. Helmut Strey, Dr. Paul Vaska and Dr. Jin Wang for taking the time to serve on my dissertation committee and for their guidance and valuable feedback. Thanks to Dr. Steven Skiena for discussions and suggestions regarding the modeling and implementation of machine learning techniques for the cybersecurity task.

Thanks to all the current members and numerous alumni of the Mujica-Parodi lab with whom I have crossed paths. Special thank you to Denis Rubin (for having the patience and will to teach me basics of fMRI and MATLAB when I was just starting), Dan DeDora (for collaboration on the SFS project), Jaime Ide (for providing the data and co-supervising the work that led to my first paper), and Anar Amgalan (for discussions about behavioral modeling and for implementation of the Bayesian Solver algorithm for the cybersecurity task). I have learned a lot from each one of you and this work would not have been possible without your contribution and friendship.

I will be forever grateful to my parents and friends for their love and support. Thanks to Anant Atyam and Sindhuja T. Govindarajan, for being there during some of the most stressful moments of this journey and believing in me even when I myself did not.

The text of this dissertation is in part a reprint of published materials. Specifically, Chapter 2 is a reprint of the manuscript titled '*Using network dynamic fMRI for detection of epileptogenic foci*' as it appears in BMC Neurology (Nedic et al., 2015). Chapter 3 is a partial reprint of the manuscript titled '*Signal fluctuation sensitivity: an improved metric for optimizing detection of resting-state fMRI networks*' as it appears in Frontiers in Neuroscience (DeDora et al., 2016). Finally, Chapter 4 is a reprint of the manuscript titled '*Signal fluctuation sensitivity identifies brain activity in naturalistic-task fMRI*', currently under review (Nedic and Mujica-Parodi, 2017).

Publications

1. **Nedic, S**., Stufflebeam, S.M., Rondinoni, C., Velasco, T.R., dos Santos, A.C., Leite, J.P., Gargaro, A.C., Mujica-Parodi, L.R., Ide, J.S., 2015. *Using Network Dynamic fMRI for Detection of Epileptogenic Foci*. BMC Neurology 15, 262.
2. DeDora, D.J.*, **Nedic, S.***, Katti, P., Arnab, S., Wald, L.L., Takahashi, A., Van Dijk, K.R., Strey, H.H., Mujica-Parodi, L.R., 2016. *Signal Fluctuation Sensitivity: An Improved Metric for Optimizing Detection of Resting-State fMRI Networks*. Frontiers in Neuroscience 10, 180. (*equally contributed)
3. Cha, J.*, DeDora, D.*, **Nedic, S.**, Ide, J., Greenberg, T., Hajcak, G., Mujica-Parodi, L.R., 2016. *Clinically Anxious Individuals Show Disrupted Feedback between Inferior Frontal Gyrus and Prefrontal-Limbic Control Circuit*. J Neuroscience 36, 4708-4718. (*equally contributed)
4. Ide, J. S., **Nedic, S.**, Wong, K.F., Strey, S.L., Lawson, E.A., Dickerson, B.C., Wald, L.L., La Camera, G., Mujica-Parodi, L.R., 2017. *Oxytocin Attenuates Trust as a Subset of More General Reinforcement Learning*. (under review)
5. **Nedic, S.**, Mujica-Parodi, L.R., 2017. *Signal Fluctuation Sensitivity Identifies Brain Activity in Naturalistic-Task fMRI*. (under review)

Chapter 1 General Introduction

Functional magnetic resonance imaging (fMRI) is a non-invasive neuroimaging modality used to measure brain activity in vivo, capable of providing three-dimensional coverage of the brain at a high spatial resolution. It measures brain activity indirectly, by detecting changes associated with blood flow. It relies on the fact that cerebral blood flow and neuronal activation are coupled – when neurons become active, local blood flow to those regions increases, resulting in oxygenated blood replacing deoxygenated blood. Since oxygenated and deoxygenated blood have different magnetic properties, this leads to changes in the magnetic resonance signal (blood-oxygen-level dependent (BOLD) contrast). In its early days, fMRI was proposed for a range of medical applications, from presurgical planning to treat epilepsy and tumors to evaluation after stroke and diagnosis of mental illness. However, since its inception in the early 1990s, its promise has been underexploited, especially in the area of mental illness where it still does not play a role in routine diagnosis, and in medical practice, where it is not widely adopted or routinely requested by neurosurgeons (Rosen and Savoy, 2012).

The underutilization of fMRI in psychiatric diagnosis and clinical practice may be due to low signal-to-noise ratios and simplistic analyses associated with standard neuroimaging approaches. To date, fMRI data have been examined predominantly in two ways: 1) by contrasting signal amplitudes during simple task stimuli with clear on/off conditions to localize "activations" and 2) by computing time-course cross-correlations between pairs of brain regions to infer the strength of functional "connectivity" between them. Research findings are typically averaged over many trials and/or subjects, usually culminating in statistical tests for differences between conditions across many subjects, or between groups of subjects, such as patients and healthy controls. On the other hand, clinical diagnostics are necessarily based upon a single subject, thus requiring methods with high sensitivity to abnormalities in network dynamics and limiting fMRI's potential for contribution in clinical settings.

Data analysis and interpretation have been complicated by the fact that the degree to which fMRI time-series preserve true neuronal signal dynamics (dynamic fidelity) is unclear since scanner and physiological noise may mask biologically relevant fluctuations of interest. However, an appropriate measure of dynamic fidelity does not exist. Furthermore, while fMRI time-series have traditionally been considered too short and with temporal resolution that was too low to

accurately capture temporal dynamics and permit application of most dynamical methods, introduction of advanced simultaneous multi-slice EPI sequences (allowing faster sampling rates/lower repetition time (TR)) in conjunction with ultra-high field MRI (compensating for reduced signal at low TR) has increased the (whole-brain) temporal resolution fivefold, from ~2.5s to ~500ms.

Finally, as our understanding of the brain has increased, so has the complexity of our questions. The last decade of fMRI research has seen an explosion of studies featuring more realistic (naturalistic) task paradigms and increased utilization of techniques aimed at not simply answering "where" and "how much," but also describing the dynamics by which information is transmitted between brain regions and, most recently, first mechanistic attempts at explaining how these lead to observable behaviors (Rigoux and Daunizeau, 2015). For example, complexity and network analyses of fMRI time-series, probing dysregulated negative feedback loops in brain circuits, have recently been applied to identify abnormalities in brain networks of patients with anxiety and schizophrenia (Cha et al., 2016; Radulescu et al., 2012), where they have been shown to be more sensitive to dysregulation than traditional amplitude-based methods. Clinical questions still require development of methods that move beyond simple amplitude and correlation-based analyses, which consider nodes and their connections in isolation and at a single point in time, to analyses which look at those nodes and connections as a dynamic system, evolving over time.

Research presented in this dissertation covers work aimed at addressing these issues. First, in Chapter 2, starting from the hypothesis that the most sensitive biomarker of dysregulation may not be the amplitude of activation or strength of connection between two nodes, but rather the complexity of the signal, reflecting the underlying (deviations) in dynamics, we introduce a new method for fMRI time-series dynamics analyses that can be used to identify dysregulation in brain networks. We propose to use the autocorrelation function (ACF) to quantify complexity (degree of order versus chaos) of fMRI time-series in the time-domain. The rate of decay of the autocorrelation function may be used as a compact measure of randomness of a time-series, and deviations towards either too much randomness or too much order may be useful diagnostically. We apply this method to identify foci in patients with medication-resistant focal epilepsy. Epilepsy is one of the most prevalent neurological disorders, affecting approximately 50 million people worldwide (Banerjee et al., 2009). It remains medically intractable for about one-third of patients

with focal epilepsy, for whom precise localization of the epileptogenic zone responsible for seizure initiation may be critical for successful surgery (Tellez-Zenteno et al., 2005).

We validate the method in a group of 19 patients with well-characterized foci (left temporal lobe epilepsy (LTLE)). We analyzed voxel-wise resting-state fMRI time-series using the autocorrelation function (ACF) and performed follow-up seed-to-voxel functional connectivity analysis. ACF analysis revealed constrained (less chaotic) functional dynamics in left temporal lobe epilepsy patients, primarily localized to ipsilateral temporal pole, proximal to presumed focal points. In a follow-up classification analysis, autocorrelation decay rates differentiated, with 100% accuracy, between patients and healthy controls on a subject-by-subject basis within a leave-one-subject out classification framework. Disruptions in connectivity of the region exhibiting abnormal dynamics were examined in relation to duration of epilepsy and patients' cognitive performance using a delayed verbal memory recall task. Constrained dynamics were linked with locally increased and long-range decreased connectivity that, in turn, correlated significantly with impaired memory and epilepsy duration. Graph-theoretical analyses showed that regions identified via ACF analysis formed a less efficient network in patients, as compared to controls.

Our current results suggest that data driven functional MRI methods that target network dynamics hold promise in providing clinically valuable tools for identification of epileptic regions. Future work is needed to test these at individual-subject level in patients with other forms of medically intractable epilepsy and difficult-to-localize foci. However, neurodiagnostics at a single-subject level impose stricter requirements on data quality and require that we are able to separate signal of interest from noise. In Chapter 3, we introduce a new quantitative measure – *signal fluctuation sensitivity* (*SFS*), to accurately assess the temporal integrity of resting-state fMRI time-series. SFS is defined specifically to dissociate signal of interest (thought to arise from true BOLD fluctuations) from scanner-induced noise. We define dynamic fidelity as the correlation between true underlying fluctuations and associated fMRI outputs and we use the dynamic phantom to provide the ground truth. We show that SFS correlates with dynamic fidelity in dynamic phantom scans as well as with our ability to detect local and long-range connectivity in human resting-state fMRI data.

In Chapter 4, we show that this measure may also be used to detect neural activity in complex unstructured/naturalistic fMRI task designs, which provide a more realistic representation of the real world compared to traditionally used simplistic block and event-related designs, but

represent a challenge from the data analysis perspective. We demonstrate the utility of SFS in identifying brain regions engaged by such tasks in three tasks of varying levels of complexity: a short movie consisting of silent scenes from a nature documentary, an episode of an emotionally engaging television drama series, and an iterative neuroeconomic game. Areas identified as having significantly higher SFS values during each task relative to resting state in same subjects were confirmed as corresponding to task-induced activations by comparison to existing literature on similar tasks, near-perfect correlation of the bilateral orbitofrontal cortex (OFC) with dynamic ratings of emotional arousal/valence, and by comparison to findings derived from inter-subject correlations (ISCs) and the independent component analysis (ICA). SFS can therefore be seen as a good alternative to existing approaches, such as ISCs and ICA, with the advantage of being assumptions-free, both in terms of not requiring a design matrix and not depending on an expected shape of hemodynamic response function, being applicable to tasks with a certain level of randomness (such as self-paced games) and being a simple measure of activation, easily generalizable to group analyses.

Finally, in Chapter 5, we move towards single-subject predictive modeling by combining high fidelity fMRI data with computational modeling and machine learning methods to predict subjects' dynamic state of mind from network dynamics of relevant brain networks (identified in a data-driven manner via independent component analyses of fMRI data). In the context of a complex dynamic self-paced cybersecurity game where subjects are expected to identify correct pattern while faced with ambiguous feedback, we show that brain fMRI time-series derived from relevant networks may be used to predict subjects' state of mind (*confident* versus *confused*) throughout the game at confidence levels beyond those expected by chance, in out-of-sample testing data, and at an individual-subject level. This work may be seen as a first step in demonstrating that high fidelity (brain) data may be used to make individual-level (state of mind) predictions. Future work may employ methods presented here, paired with more sophisticated machine learning algorithms, to isolate features of interest from a larger set of regions and do more detailed, circuit-level predictions of dynamics.

Chapter 2 Using Network Dynamic fMRI for Detection of Epileptogenic Foci

Modified from Nedic, S., Stufflebeam, S.M., Rondinoni, C., Velasco, T.R., dos Santos, A.C., Leite, J.P., Gargaro, A.C., Mujica-Parodi, L.R., Ide, J.S., 2015. *Using Network Dynamic fMRI for Detection of Epileptogenic Foci*. BMC Neurology 15, 262.

Abstract

Epilepsy is one of the most prevalent neurological disorders. It remains medically intractable for about one-third of patients with focal epilepsy, for whom precise localization of the epileptogenic zone responsible for seizure initiation may be critical for successful surgery. Existing fMRI literature points to widespread network disturbances in functional connectivity. Per previous scalp and intracranial EEG studies and consistent with excessive local synchronization during interictal discharges, we hypothesized that, relative to same regions in healthy controls, epileptogenic foci would exhibit less chaotic dynamics, identifiable via entropic analyses of resting state fMRI time series. In order to first validate this hypothesis on a cohort of patients with known ground truth, here we test individuals with well-defined epileptogenic foci (left mesial temporal lobe epilepsy (LTLE)). We analyzed voxel-wise resting-state fMRI time-series using the autocorrelation function (ACF), an entropic measure of regulation and feedback, and performed follow-up seed-to-voxel functional connectivity analysis. Disruptions in connectivity of the region exhibiting abnormal dynamics were examined in relation to duration of epilepsy and patients' cognitive performance using a delayed verbal memory recall task. ACF analysis revealed constrained (less chaotic) functional dynamics in left temporal lobe epilepsy patients, primarily localized to ipsilateral temporal pole, proximal to presumed focal points. Autocorrelation decay rates differentiated, with 100% accuracy, between patients and healthy controls on a subject-by-subject basis within a leave-one-subject out classification framework. Regions identified via ACF analysis formed a less efficient network in patients, as compared to controls. Constrained dynamics were linked with locally increased and long-range decreased connectivity that, in turn, correlated significantly with impaired memory (local left temporal connectivity) and epilepsy duration (left temporal – posterior cingulate cortex connectivity). Our current results suggest that data driven functional MRI methods that target network dynamics hold promise in providing clinically valuable tools for identification of epileptic regions.

Introduction

Epilepsy is one of the most prevalent neurological disorders, affecting approximately 50 million people worldwide (Banerjee et al., 2009). It is characterized by seizures, resulting from abnormal transient change in the synchronized firing of neurons (Lehnertz et al., 2009). For one-third of patients with focal epilepsy, debilitating seizures persist despite antiepileptic drug therapy, leaving surgical resection of the suspected epileptogenic focal region as the most effective treatment option (Kwan and Brodie, 2000; Tellez-Zenteno et al., 2005). Precise localization of the epileptogenic zone responsible for initiation and propagation of seizures, and its delineation from eloquent cortex, are crucial for successful surgery. However, current standard non-invasive surgical evaluation (looking for congruence of seizure semiology, abnormalities on structural magnetic resonance images (MRI) and spikes in scalp electroencephalographic (EEG) recordings) fails to identify an epileptic focus in approximately 40% of patients with drug resistant epilepsy (Wellmer et al., 2012). The current gold standard for localization of focal regions includes identification of an epileptogenic zone on intracranial EEG recordings combined with postoperative seizure freedom following its resection; however, invasive pre-surgical workup carries additional risks and has been associated with complications in about 23% of patients (Wellmer et al., 2012). Thus, the development of noninvasive techniques capable of accurately localizing epileptogenic regions on a subject-by-subject basis will be critical for improving surgical outcomes.

Multimodal studies, especially those utilizing simultaneous EEG-functional MRI (fMRI) recordings, increasingly have been used to provide complementary information in presurgical work-up. EEG-fMRI allows mapping of hemodynamic changes related to seizure-related events, such as interictal discharges (IEDs). Spikes are manually detected in EEG data and, in traditional "spike-correlated" analysis, they are treated as zero-duration events, convolved with canonical hemodynamic response function (HRF), and included as regressors of interest in a General Linear Model (GLM) along with simultaneously acquired blood-oxygen-level dependent (BOLD) time series as dependent variables. Functional MRI maps related to IEDs often show multiple regions or "networks," rather than focal singularities, and thus effective connectivity approaches such as Dynamic Causal Modeling (DCM) have been proposed to identify which brain regions drive the generation of seizures within the epileptic network (Klamer et al., 2015; Vaudano et al., 2013).

The EEG-fMRI approach suffers from a few potential drawbacks. First, a significant portion of subjects do not experience enough detectable IEDs during simultaneous recording. This problem is partially addressed by introduction of topography-related techniques, which, instead of requiring simultaneously recorded spikes, use subject-specific voltage maps based on long-term video monitoring (Grouiller et al., 2011). Second, epilepsy may alter the shape of the HRF, which could result in decreased sensitivity (Bagshaw et al., 2004). Third, in addition to setup time, EEG-fMRI requires on average 30 minutes of motionless cooperation from subjects, which may be problematic for certain patients, especially children. Fourth, the use of scalp EEG is inherently constrained by its limited sensitivity to deep activity. Despite this, sensitivity of topography-related EEG-fMRI in refractory focal epilepsy was found to be about 80% (Elshoff et al., 2012; Grouiller et al., 2011). However, measured sensitivity appears to be highly study-dependent. For example, a recent study proposing concurrent use of four different modalities found that topography-related EEG-fMRI method on its own showed clinically meaningful result in five out of twelve studied patients ((Grouiller et al., 2015)). Here we propose an alternative data-driven method utilizing only resting state fMRI data.

As a matter of general research strategy, any method with potential to identify seizure onset zones first needs to be validated with respect to a "ground truth." In the case of epilepsy, the most reasonable option is to use patients with clinically well-defined focal regions; after validation against these cases, one can then apply the method to more challenging cryptogenic cases. Mesial Temporal Lobe Epilepsy (MTLE) is the most prevalent and best-characterized subset of drug resistant focal epilepsy in adults, and thus is an ideal cohort for validation of novel methods aimed at identification and localization of epileptic foci and/or networks.

Brain regions involved in the onset and propagation of MTLE have been studied extensively, with the most commonly associated pathology being hippocampal sclerosis (HS). Seizures originating in the medial temporal region are known to rapidly spread to lateral temporal regions, the insula, the thalamus, and the contralateral temporal lobe (among other regions) (Hogan et al., 2006), suggesting that MTLE may be characterized by a network disturbance. Indeed, recent structural and functional MRI studies have revealed widespread abnormalities, with structural changes primarily involving atrophy of ipsilateral temporal pole and other temporolimbic structures (Assaf et al., 2003; Focke et al., 2008). Functional MRI (fMRI) studies have found changes in functional connectivity of the temporal region with other brain areas, along with

impaired resting state networks such as perceptual, attention and default mode networks (Bettus et al., 2010; Bettus et al., 2009; Liao et al., 2010; Liao et al., 2011; Maneshi et al., 2014; Pereira et al., 2010; Pittau et al., 2012; Tracy and Doucet, 2015; Zhang et al., 2009; Zhang et al., 2010).

Graph theoretical network analyses of brain networks use sets of nodes connected by edges in order to quantify general structural features of brain connectivity between regions. Numerous studies suggest that healthy brain networks show a high degree of *small-worldness* (for a review see (Bullmore and Sporns, 2009)), which provides a balance between local clustering (characteristic of highly ordered, *regular* networks) and long-range connections (characteristic of low order, *random* networks). This balance reflects the result of synaptic optimization over the efficiency of information transfer and the need for redundancy in case of injury. In individuals with focal temporal and extratemporal neocortical epilepsy, fMRI, EEG, magnetoencephalography (MEG), and intracerebral recordings suggest that this balance appears to be shifted towards predominantly local clustering (Bartolomei et al., 2013; Horstmann et al., 2010; Liao et al., 2010), which may predispose the network towards synchronized oscillations characteristic of seizures (Stam, 2014).

However, findings are not clear-cut. While many studies report decreases in functional connectivity localized near the suspected seizure onset zone (Bettus et al., 2010; Bettus et al., 2009; Pereira et al., 2010; Pittau et al., 2012), others show increases (Liao et al., 2010; Maccotta et al., 2013; Maneshi et al., 2014; Morgan et al., 2011; Stufflebeam et al., 2011), potentially due to differences in connectivity metrics used, as well as heterogeneity of patient populations and small sample sizes. It is important to note that, in spite of the benefits of considering epileptic networks, accurate localization is still clinically desirable as suggested by the relatively high success rate of surgical treatment for 'focal' epilepsies (about 66%) (Lehnertz et al., 2009). Yet most fMRI studies aimed at localization of the epileptogenic zone point to widespread abnormalities that are, at best, lateralized to one of the hemispheres.

Complex systems produce outputs that are balanced between overly chaotic and overly predictable dynamics; as such, they have the advantage of requiring a minimum of energy both to respond to inputs as well as to return to baseline (as required for allostasis). Complexity of brain activity has been observed and modeled on many levels, from neurotransmitter release (Lowen et al., 1997), neuronal spiking (Levina et al., 2007; Rubinov et al., 2011) and local field potentials (Bedard and Destexhe, 2009) to slow cortical potentials (He and Raichle, 2009),

electrocorticography (ECoG) (Lai et al., 2010) and EEG (Freyer et al., 2009), suggesting that scale-free behavior may be fundamental to efficient neural information processing. Deviations from optimal range of functioning in fMRI time series have been used diagnostically in identifying brain-based disease (Lai et al., 2010; Maxim et al., 2005; Radulescu et al., 2012). In the case of a disease as heterogeneous as epilepsy, fMRI's exploratory capability (simultaneously acquiring functional information over focal, hemispheric, and whole-brain neural networks) may provide a clinically valuable tool in guiding placement of intracranial EEG, as the process of seizure generation is not necessarily confined to a focal area and may involve distant or contralateral areas of the brain. Here we propose to use autocorrelation function (ACF) as a measure of complexity in resting-state fMRI time series, with the aim of localizing deviations from optimal dynamics in epilepsy.

Brain trauma increases risk for seizures. One possible mechanism suggested by animal models of epilepsy is the enhanced synaptic sprouting due to MMP-9 mediated matrix-degradation that occurs as a compensatory response to injury (Wilczynski et al., 2008). Alternatively, sensitivity to glucose fluctuations may impact of the brain's ability to use energy in creating long-range, but not short-range, connections, upsetting balance between the two. Thus, we hypothesized that the hippocampal sclerosis common to MTLE patients might result in hubs surrounded by more dense local connectivity. This can constrain dynamics within the hub either by increased density of inhibitory or excitatory inputs, both of which would result in less chaotic resting state fMRI time series. We expected abnormal dynamics to be identifiable through comparison of decay rates of the time series' ACF in patients and in healthy controls. This is consistent with previous findings from scalp and intracranial EEG studies (Bruzzo et al., 2008; Molteni et al., 2008; Monto et al., 2007; Protzner et al., 2010), as well as with excessive local synchronization during interictal discharges.

Less chaotic dynamics in focal region(s) may lead to increased local synchronization and transient seizures. Repeated seizures could in turn lead to damage in connections of this region with contralateral regions and major hubs in the brain. We therefore hypothesized that these disconnections would be detectable via seed-to-voxel functional connectivity analyses of fMRI time-series, using the region with abnormal dynamics (identified through ACF analyses) as a seed. Finally, we expected that abnormalities in connectivity would relate to duration of epilepsy and patients' cognitive performance on a verbal memory recall task. To determine whether group

differences achieving statistical significance continued to hold on the single-subject level (as required for individual neurodiagnostics of other types of epilepsy), we applied Gaussian Process Classification with leave-one-subject-out cross validation to ACF decay rates in regions with altered dynamics.

Methods

Participants

Nineteen patients (mean age = 40 years ± 13; 8 males, 11 females) with mesial left temporal lobe epilepsy (LTLE) were included in this study based on a clear clinical diagnosis of unilateral (left) temporal epileptic activity according to concordant clinical information. The inclusion criteria were: 1) seizure semiology consistent with MTLE, which included epigastric, autonomic, or psychic auras followed by behavioral arrest, progressive clouding of consciousness, oroalimentary and manual automatisms, and autonomic phenomena; 2) anterior and mesial temporal interictal spikes; 3) video-EEG monitoring with seizure onsets arising exclusively from the temporal lobe; 4) MRI with no other lesion than hippocampal atrophy and a hyperintense signal on T2-weighted sequences; and 5) medically refractory MTLE, defined as failure to respond to at least two antiepileptic drugs after adequate trials. For patients whose scalp ictal EEG recordings were inconclusive, foramen oval electrodes or depth electrodes were used to define lateralization of seizure foci. **Table 2-1** lists demographic and clinical characteristics of all patients studied here. Nineteen healthy controls (mean age = 41 years ± 12; 8 males, 11 females), age and sex-matched to patients (2-sample t test p=0.78), were scanned under the same protocol. Because temporal lobe epilepsy affects the hippocampus, and is associated with progressive memory deficits (Helmstaedter et al., 2003), in order to assess clinical symptoms patients were asked to complete the Logical Memory Delayed Recall (LM-DR) subtest of the Wechsler Memory Scale – Revised (Wechsler, 1987). This task requires subjects to recall specific details of information presented orally in a story format thirty minutes after a single exposure. The research protocol was approved by the local Ethical Committee of Clinics Hospital at Ribeirao Preto, São Paulo, Brazil. Written informed consent was obtained from the patient for publication of their individual details in this manuscript. All subjects were older than 18 years of age and were capable of providing full and informed consent.

Data Acquisition

All subjects were scanned using a Philips Achieva 3T scanner with an eight-channel head coil. Whole brain functional volumes were acquired under resting state using soft-tone sequences (repetition time (TR) = 2000ms, echo time (TE) = 30ms, 200 volumes, voxel dimensions: 3 × 3 × 4 mm, 32 slices, 0.5 mm gap, matrix size = 80 × 80, flip angle = 80°). Subjects were instructed to keep their eyes open and to refrain from falling asleep. The eyes open condition was used rather than eyes closed condition to ensure that subjects remained awake during scanning. T1-weighted anatomical images were acquired using a conventional 3D-T1 MPRAGE sequence (TR = 7.0, TE = 3.2, matrix size = 240 × 240, flip angle = 8°, 1 mm isotropic voxels).

fMRI Data Preprocessing

Functional MRI data were preprocessed by correcting for motion (rigid realignment, 6 degrees-of-freedom), slice-time correction, normalization to MNI space (affine registration followed by a nonlinear transformation between average fMRI and EPI template, and sync interpolation), and smoothing with an 8-mm full width at half maximum Gaussian kernel in SPM8 (www.fil.ion.ucl.ac.u/spm).

Patient	Gender	Age/ Onset	Frequency (month)	Febrile seizures	Seizure Type	Interictal EEG	Ictal EEG	MRI findings	Antiepileptic Medications	Surgical Outcome
1	F	44/18	30	No	Masticatory automatisms	Left temporal paroxysms	Bilateral theta rhythm, late left lateralization	Left HA	PHT, TPM	3
2	M	59/10	4	Yes	Complex partial	100% left temporal	Left temporal	Left HA	CBZ	1
3	F	27/13	4	No	Complex partial	70% left, 30% right temporal	Left temporal	Left HA	LTG, CLB, OXC	1
4	M	47/24	4	No	Lack of consciousness no aura	Left temporal sharp waves (89%, T1, T9)	Left temporal theta	Left HA	CBZ, LTG, CLB	1
5	F	32/19	0.5	No	Complex partial	Rare left temporal	Left temporal	Discrete left HA	CBZ, PB, CLB	1

6	F	34/25	4	No	Complex partial	53% left, 47% right temporal	Left temporal	Discrete left HA, normal volume	TPM, OXC, CLB	3
7	M	26/5	4	No	Complex partial	Normal	Left temporal delta rhythm	Left HA	VPA, OXC, CLB	1
8	F	44/9	4	No	Complex partial	70% left, 30% right temporal	Left temporal	Left HA	CBZ, TPM, CLN	3
9	F	47/17	4	No	Lack of consciousness, automatisms	Slow theta in left temporal	Bilateral theta activity followed by left temporal theta	Left HA	LTG, CBZ	1
10	M	37/2	2	No	Complex partial	95% left, 5% right temporal	Left temporal	Left HA	OXC, LTG	1
11	M	46/18	n/a	No	Complex partial	Slow waves in left temporal	Left hemisphere diffuse desynchronization	Left HA	PHT, PB	1
12	F	52/14	2	Yes	Complex partial	100% left temporal	Left temporal	Left HA	CBZ, TPM	2
13	F	22/19	3	Yes	Tonic-clonic secondarily generalized	Left spikes	Left temporal	Left HA	OXC, VPA, CLB	1
14	F	22/1	16	Yes	Complex partial	Left temporal	Left temporal	Left HA	TPM, OXC	1
15	F	49/15	1	No	Complex partial	100% left temporal	Left temporal	Left HA	CBZ, PB	1
16	M	59/53	1	No	Complex partial	100% left temporal	Left temporal	Left HA	PHT	3
17	M	20/4	30	Yes	Epigastric aura and lack of consciousness	Left temporal slow waves	Left temporal	Left HA	CBZ, VPA	1
18	F	30/10	30	No	Complex partial seizures preceded by sensitive auras	Left temporal theta rhythm	Complex partial seizure	Discrete HA + double cortex	LTG, CLB	n/a
19	M	19/8	8	No	Complex partial	100% left temporal	Left temporal	Left HA	TPM, CBZ, CLN	3

Table 2-1: Demographic and clinical information. Abbreviations: HA=hippocampal atrophy, PHT=Phenytoin, TPM = Topiramate, CBZ = Carbamazepine, LTG = Lamotrigine, CLB = Clobazam, OXC = Oxcarbazepine, PB = Phenobarbital, VPA = Valproic Acid, CLN = Clobazam. Surgical Outcome: 1 - seizure free, 2 - significant improvement, 3 - no improvement.

Autocorrelation Function (ACF) Method

An autocorrelation function (ACF) measures similarity (cross-correlation) of a signal with itself over different time lags, and can therefore be used to identify shifts towards chaos vs. order in the time domain, in a manner that is analogous to power spectral scale invariance (PSSI) analysis (Radulescu and Mujica-Parodi, 2014; Radulescu et al., 2012; Tolkunov et al., 2010) in the frequency domain. PSSI and ACF are related via the Wiener-Khinchin theorem, which states that Fourier transform of the ACF is the power spectral density ($P(f) = \int_{-\infty}^{\infty} ACF(t)e^{-2\pi ift}dt$).

PSSI of fMRI time series has already been used to quantify limbic dysregulation in trait anxious adults (Tolkunov et al., 2010) and effectively discriminate between normal and pathogenic network dynamics in schizophrenia (Radulescu et al., 2012) and generalized anxiety disorder (DeDora et al., under review). PSSI analysis is based on the finding that fMRI BOLD time series exhibit power spectral density that follows a power law (He, 2011) $P(f) \sim 1/f^{\beta}$, where β is the scaling exponent. The scaling exponent β then measures relative frequency content of the signal and is evaluated as the negative slope of a straight line fit to power spectral density as a function of frequency on log-log scale. Linear least squares method is employed. In contrast, the ACF of voxel-wise BOLD time series can be modeled as an exponential decay:

$$ACF(t) = a\, e^{-bt},$$

for which t is time lag in units of TR, and a and b are constants such that $b > 0$. The rate of this decay, which is proportional to the constant b, may be used as a compact measure of randomness of a time series, with higher b signifying faster decay (more randomness) and lower b signifying slower decay (more persistence). ACF b values are then related to the mean lifetime decay of a signal, τ (seconds), via the relation $\tau = 1/b \times TR$. Conceptually, τ represents the length of time that a signal maintains a high degree of association with its past values. A random time series (white noise) would have $\tau = 0$. Larger values of τ would imply longer memory in the signal.

ACF has several advantages as compared to PSSI. First, ACF decay times have physiologically intuitive meaning, understood as self-similarity over different lengths of time (in seconds). Second, ACF model fits for fMRI time-series are improved compared with PSSI, because ACF avoids the need to use linear least squares fitting in log-log space (Clauset et al., 2009).

Prior to whole brain voxel-wise computation of ACF b values, to remove potential effects of nuisance variables and improve signal to noise ratio, we performed further preprocessing of fMRI time series. The preprocessing procedure included detrending and regression of mean white matter and mean cerebrospinal fluid (CSF) signals, as well as regression of six degrees of motion. Motion parameters were derived from the realignment procedure, while global regressors were obtained from canonical masks for white matter and CSF included in the SPM8. To rule out head motion related artifacts on b values, we confirmed that there were no statistically significant differences in movement between the two subject groups using root mean square displacement (2 sample t-test: $p = 0.37$). Root mean square displacement was calculated as the square root of the sum of squares of all six motion parameters (Power et al., 2012).

The residual time series were band-pass filtered in the 0.01 - 0.1 Hz frequency range using 10th order Butterworth filter. Fitting was performed within a frequency range of 0.01-0.1 Hz since low frequency oscillations in this band show power-law behavior (He, 2011; Lai et al., 2010), making PSSI-related inferences valid in this range, and are furthermore of special interest in resting-state fMRI connectivity analyses since they have been shown to have neuronal basis (Biswal et al., 1995; Biswal et al., 1997; Clauset et al., 2009).

We estimated voxel-wise time series ACF using the Econometrics Toolbox implemented in MATLAB R2010a. We then fit an exponential function of the form $y = ae^{-bx}$ to the first 9 (lag = 8) points of each voxel's ACF using the nonlinear least-squares fitting method as implemented in the Curve Fitting Toolbox, also part of MATLAB R2010a. Lag of 8 (16.8 seconds at TR of 2 seconds) was determined as most appropriate based on considerations of goodness of fit of the exponential function and duration of canonical hemodynamic response (Miezin et al., 2000).

Group differences in voxel-wise b values were examined using a two sample t-test in SPM8. Clusters greater than 26 voxels with $p < 0.005$ were isolated and used in further analyses. Prior to voxel-wise t-tests, the Lilliefors goodness-of-fit test (as implemented in REST toolbox (Song et al., 2011)) was used to confirm that voxel-wise ACF-b values were normally distributed within each group of subjects. We found that the hypothesis of normality was supported by the vast majority (94%) of brain voxels in each group at the $p = 0.05$ level.

Classification

To verify that the group differences in b values were statistically significant and capable of differentiating between patients and healthy controls, even on a subject-by-subject basis, we conducted follow-up machine learning analyses on ACF b maps using Pattern Recognition for Neuroimaging Toolbox (PRoNTo) (Schrouff et al., 2013). We constrained the analyses to those regions that were identified as having different b values between the two groups using the 2-sample t-test in SPM8. We employed Binary Gaussian Process Classification with leave one subject out cross-validation. Follow-up permutation testing (with 2000 repetitions) was used to test whether the obtained overall and class accuracies were significantly above chance, and thus indicate whether the pattern of ACF decay times in those brain regions encodes sufficient information to diagnose (correctly classify) MTLE.

Functional Connectivity

In order to gain further understanding of the functional network features that might underlie abnormalities in fMRI signal dynamics, we used the cluster in the left anterior temporal pole identified as having most significantly different ACF b values in patients compared to controls (cluster extent = 59 voxels; **Figure 2-1A**) as a seed in seed-to-voxel functional connectivity analysis using CONN Toolbox (http://www.nitrc.org/projects/conn/; v 13.p). We examined the differences in seed-to-voxel connectivity between LTLE patients and healthy controls using one-sided 2 sample t-tests. Time series were extracted from spatially smoothed images. They were detrended, despiked (a hyperbolic tangent squashing function was applied to reduce the influence of potential outlier scans), and white matter, cerebrospinal fluid, and motion parameters from SPM's realignment step and their first derivatives were regressed out as confounds. Finally, the residual time series were band-pass filtered in the [0.01-0.1] Hz range. Correlation maps were computed from the seed to all voxels in the brain and transformed to Fisher-z values (to ensure normality) prior to performing t-tests to look at differences between the two groups. We identified clusters of voxels that were significantly differently connected to the region exhibiting constrained dynamics (identified via ACF analysis) in patients relative to controls. We then used correlation analysis to test whether connectivity of these clusters to the seed was related to duration of epilepsy and verbal memory as measured by the LM-DR task.

Graph-Theoretic Analyses

To determine whether complexity and connectivity results reflected global differences in network structure, we used the CONN Toolbox to investigate graph-theoretic characteristics of the network with nodes at clusters identified as having different ACF b values in patients compared to controls. Bivariate correlation of the mean time series was used as a measure of association between the nodes. For this 16-node network, we compared the two subject groups with respect to Global Efficiency, Local Efficiency, Betweenness-Centrality, Average Path Length, Clustering Coefficient, and Degree under a range of values of cost (0.1 – 0.3) (Achard and Bullmore, 2007; Latora and Marchiori, 2001).

Results

Left Temporal Lobe Epilepsy Patients Show Constrained Dynamics of Left Temporal Pole

Unbiased (exploratory) analyses identified the *superior left temporal pole* (peak MNI coordinate: (-36 2 -17), $p < 0.005$ uncorrected, cluster extent = 59 voxels, peak $T_{36} = 7.11$; **Figure 2-1**) as showing the greatest differences between LTLE patients and healthy controls; patients showed significantly decreased ACF b values (i.e., slower ACF decay, more constrained dynamics). In addition, 15 other regions, all exceeding 27 voxels, showed lowered ACF b values in patients at $p < 0.005$. Regions involved include portions of the *right inferior frontal gyrus*, *left thalamus*, *right precuneus*, *right caudate*, *bilateral heschl gyrus*, *bilateral inferior parietal and postcentral area*, and *bilateral insula*. These results are presented in **Table 2-2**. No regions showed increased ACF b values in patients compared to controls. We repeated the 2-sample t-test 38 times, each time leaving one subject out. Each time, a cluster at MNI (-36 2 -17) was found to be significantly different between the LTLE patients and healthy controls, confirming reliability across subjects, and the absence of outlier-effects. In addition, to probe the potential for single-subject analyses, we compared voxel-wise whole-brain individual patients' ACF b maps to the average healthy control ACF b map, and found that for 13 out of 19 patients there was a cluster (>6 voxels, median size = 32 voxels) at the identical coordinate (-36 2 -17) which had b values that were more than two standard deviations lower than those in the same region in the mean control map. Remaining patients had such clusters within the left temporal lobe.

Classification Analyses Achieve 100% Accuracy in Distinguishing Patients vs. Controls

To verify that the differences in ACF b values were not only statistically significant at the group level, but also capable of differentiating between patients and healthy controls even on a subject-by-subject basis, we conducted follow-up classification analyses on ACF b maps using Gaussian Process Classification with leave one subject out cross-validation. We used the mask consisting of 16 clusters identified as different between groups as a 2nd level mask in PRoNTo.

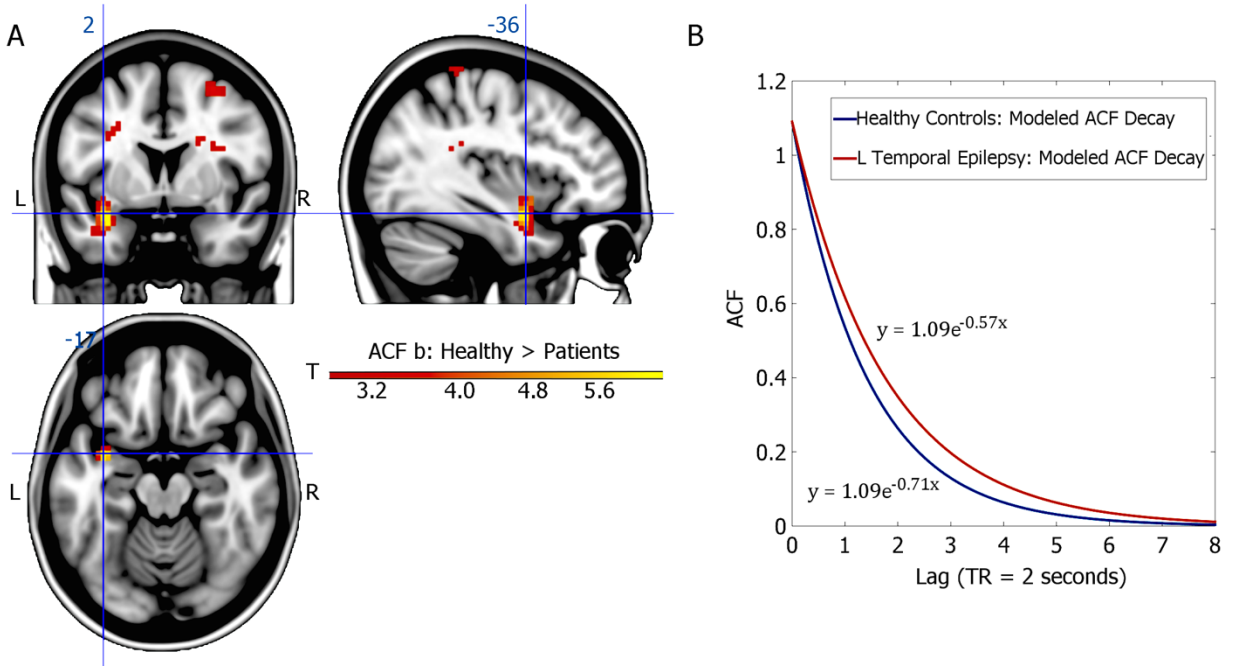

Figure 2-1: Autocorrelation decay rates (ACF b) are altered close to presumed focal regions. (A) Left Temporal Lobe Epilepsy (LTLE) patients exhibit lower ACF b values (slower decay of autocorrelation) relative to Healthy Controls (HC) in the Left Superior Temporal Pole (peak MNI coordinate [-36, 2, -17], cluster extent = 59 voxels, peak $p = 1.18 \times 10\text{-}8$, bHC(cluster) = 0.71±0.09, bLTLE(cluster) = 0.57 ±0.05)). **(B)** Modeled ACF decay for the left superior temporal pole cluster for HC and LTLE patients.

Every single subject was classified correctly, achieving 100% accuracy. Graph of prediction values and the associated density functions and weights map are shown in **Figure 2-2**. While it is the combination of all weights that defines the model and individual contributions of voxels in the 2nd level mask cannot be accessed directly, the weights map confirms that most discriminative voxels are the ones in the left temporal pole. Perfect accuracy implies that the b-values in these regions encode sufficient information for successful discrimination of the two groups.

Using only the top cluster, which showed most significant abnormality in patients according to the t-test, as a 2nd level mask, the accuracy went down, but remained highly

significant. Overall accuracy was 84.2%, with specificity and sensitivity of 84.2% (correctly classifying 16 out of 19 subjects in each group). Follow-up permutation testing (with 2000 repetitions) confirmed that both the overall accuracy (p = 0.005) and the class accuracies (p = 0.005; p = 0.005) were significantly above chance. Therefore, ACF b values from this part of brain alone contain sufficient information for significant discrimination between the two subject groups.

	Left TLE < Healthy Controls			
	Peak MNI	**Location Description (AAL)**	**Cluster Extent**	**t-test (peak-level T (p))**
1	**[-36, 2, -17]**	**L Superior Temporal Pole, Middle Temporal Pole, Insula, Amygdala**	**59**	**7.11 (1.18×10^{-8})**
2	[42, 23, 13]	R Inferior Frontal Gyrus, Pars Triangularis, Inferior Frontal Gyrus, Pars Opercularis	71	4.59 (2.61×10^{-5})
3	[-27, -7, 28]	L White Matter (Precentral)	43	4.57 (2.79×10^{-5})
4	[-12, -10, -2]	L Thalamus	33	4.56 (2.85×10^{-5})
5	[-45, -37, 43]	L Inferior Parietal Lobule, Postcentral Gyrus	69	4.40 (4.64×10^{-5})
6	[21, 8, 25]	R Caudate	69	4.31 (5.95×10^{-5})
7	[36, -22, 19]	R Insula, R Heschl	27	4.20 (8.37×10^{-5})
8	[30, -43, 52]	R Inferior Parietal Lobule	88	4.10 (1.13×10^{-4})
9	[15, -46, 7]	R Precuneus	34	4.07 (1.22×10^{-4})
10	**[-24, -34, 70]**	L Postcentral Gyrus, Paracentral Gyrus	60	3.99 (1.53×10^{-4})
11	**[30, 41, 1]**	R White Matter (Frontal)	42	3.89 (2.01×10^{-4})
12	[12, -112, -2]	L Calcarine	31	3.84 (2.41×10^{-4})
13	[-30, -43, 25]	L White Matter (Parietal)	31	3.68 (3.78×10^{-4})
14	[30, 2, 58]	R Middle Frontal Gyrus, Superior Frontal Gyrus	29	3.62 (4.46×10^{-4})
15	[-54, -10, 10]	L Heschl	29	3.46 (6.95×10^{-4})
16	[3, -91, 10]	L Calcarine	30	3.28 (1.20×10^{-3})

Table 2-2: List of regions showing significantly different values of ACF b in patients relative to controls. Two-sample t-test was performed in SPM8 ($p < 0.005$, $k \geq 27$).

As a control, we repeated the classification using the entire grey matter mask as a 2nd level mask. Gray matter mask was obtained from SPM8 and thresholded at 0.5. This resulted in reduced specificity of 53%, not significantly greater than the one expected by chance. This confirms that we discarded most of irrelevant information when constraining the analyses to either of the two 2nd level masks described above.

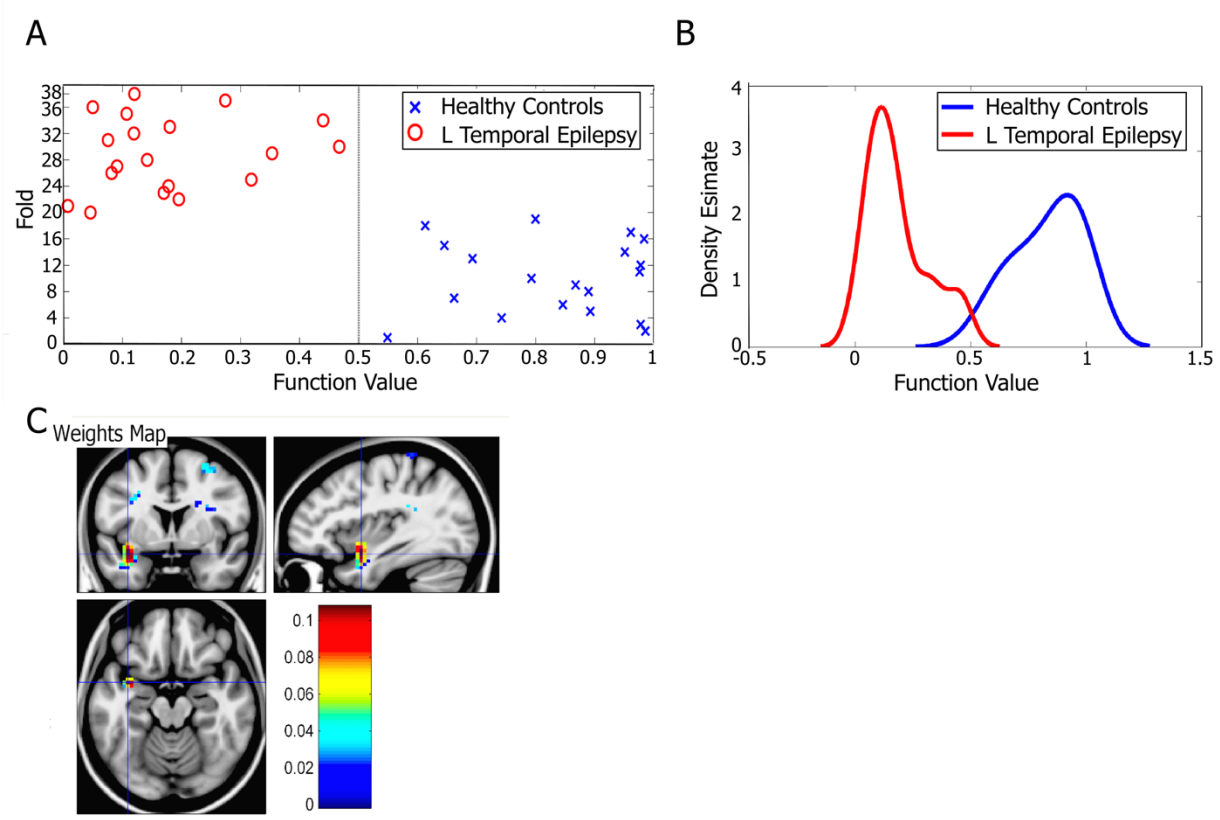

Figure 2-2: Autocorrelation decay rates classify patients with epilepsy with 100% accuracy. (A) Plot of prediction values at each level of the leave-one-subject-out cross-validation (fold) shows 100% accuracy when employing Gaussian Process Classification within Pattern Recognition for Neuroimaging Toolbox (PRoNTo) and using group differences in ACF b values as a 2nd level mask. **(B)** Density estimates of predicted function values for the two classes have a small overlap area, which is a sign of a good classifier. **(C)** Weights map shows that the left temporal lobe cluster carries most weight in the decision process.

Constrained Dynamics are Linked with Locally Dense/Long-Range Sparse Connectivity

Seed-to-voxel functional connectivity analysis revealed that LTLE patients show increase in connectivity of the most dynamically constrained cluster (ACF-identified cluster at MNI (-36 2 -17)) with neighboring *left temporal* and *frontal regions*, as well as decreases in connectivity of this cluster with parts of *bilateral dorsal posterior cingulate cortex* (PCC), *contralateral inferior temporal gyrus*, and *contralateral thalamus*, when compared to healthy controls ($p < 0.005$ uncorrected; cluster extent > 10 voxels), as shown in **Figure 2-3**. **Table 2-3** contains a complete list of significant seed-to-voxel connectivity differences.

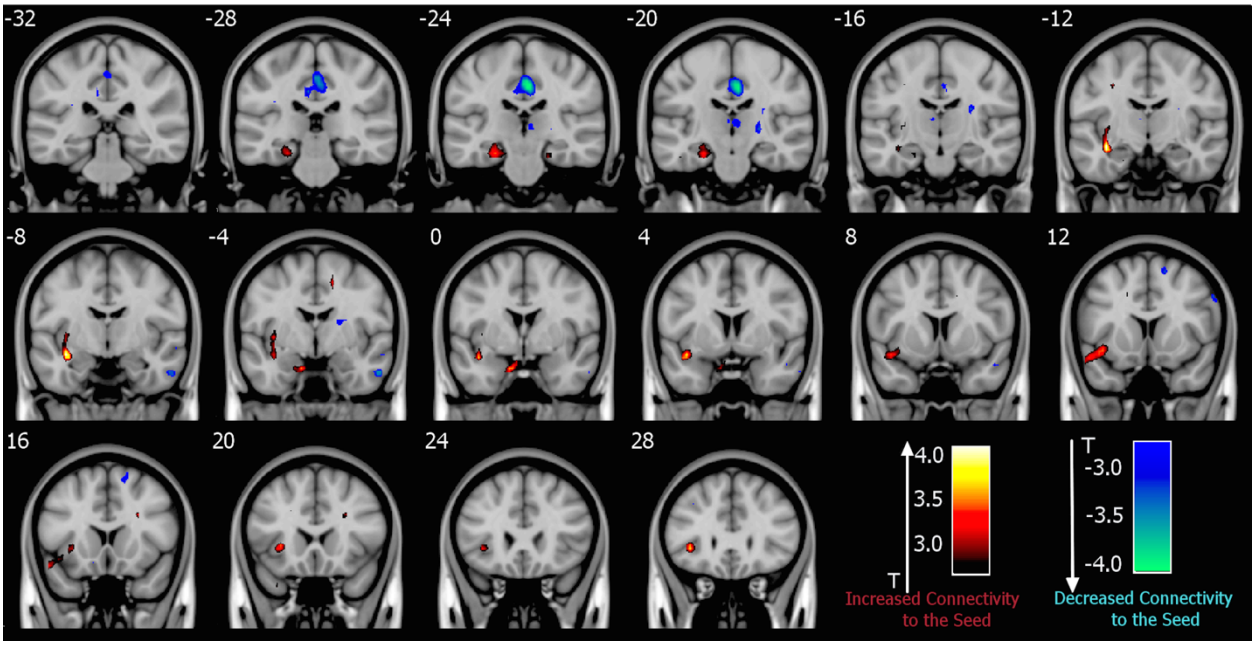

Figure 2-3: Seed-to-voxel connectivity of the ACF-identified left temporal lobe cluster is significantly different in patients. Relative to healthy controls, increases in connectivity are observed towards neighboring regions, while decreases are observed towards posterior cingulate cortex, thalamus, and the contralateral temporal lobe.

Connectivity Abnormalities Correlate with Epilepsy Duration

In linking neural and clinical features, for the latter we focused on duration rather than seizure frequency since our patient sample did not provide significant variance in the latter. We found a significant positive linear correlation (Pearson's r = 0.61, p = 0.005) between the mean connectivity of the cluster in PCC with the ACF-identified seed in left temporal pole and the duration of epilepsy. Therefore, while PCC exhibited overall decrease in connectivity with the seed in patients relative to controls, patients with longer duration of epilepsy had increased connectivity. On the other hand, for the cluster within the contralateral inferior temporal gyrus, there was a clear, but non-significant, trend towards negative correlation of this area's connectivity with the seed and duration of epilepsy (Pearson's r = -0.44, p = 0.060). For other areas that showed abnormal connectivity to the ACF-identified seed, connectivity with the seed did not exhibit linear relation to epilepsy duration.

Left TLE > Healthy Controls				
	Peak MNI	Location Description	Cluster Extent	t-test (peak level T (p))
1	[-36, -10, -14]	L Temporopolar Area (BA 38), Hippocampus, Inferior Prefrontal Gyrus (BA 47), Insular Cortex (BA 13)	115	4.23 (7.70×10^{-5})
2	[-24, -25, -20]	L Perirhinal Cortex (BA 35), Parahippocampal Cortex (BA 36)	40	3.34 (9.88×10^{-4})
3	[-36, 29, -2]	L Inferior Prefrontal Gyrus (BA 47)	27	3.67 (3.93×10^{-4})
4	[-33, -91, -2]	L Secondary Visual Cortex (BA 18)	19	3.35 (9.57×10^{-4})
5	[-27, -67, 31]	L Associative Visual Cortex (BA 19)	18	3.27 (1.20×10^{-3})

Left TLE < Healthy Controls				
	Peak MNI	Location Description	Cluster Extent	t-test (peak level T (p))
1	[6, -22, 40]	Bilateral Dorsal Posterior Cingulate Cortex (BA 31), L Ventral Anterior Cingulate Cortex (BA 24)	97	-4.13 (1.04×10^{-4})
2	[54, -7, -29]	R Inferior Temporal Gyrus (BA 20)	12	-3.61 (4.58×10^{-4})
3	[15, 14, 58]	R Premotor Cortex (BA 6)	11	-3.36 (9.27×10^{-4})
4	[6, -22, 4]	R Thalamus	11	-3.11 (1.80×10^{-3})

Table 2-3: List of regions showing significantly different functional connectivity to the ACF-identified left temporal pole cluster. Two-sample t-test was performed in CONN Toolbox ($p < 0.005$, $k \geq 10$ voxels).

Connectivity Abnormalities Correlate with Verbal Memory Task Performance

We found that disrupted local connectivity of the left temporal lobe ACF cluster correlated negatively with performance on the LM-DR task (Pearson's r = -0.50, $p = 0.03$, **Figure 2-4**); that is, patients who performed poorly on the verbal memory task exhibited higher local connectivity relative to those who did well. Greater severity of clinical symptoms was thus associated with higher local connectivity.

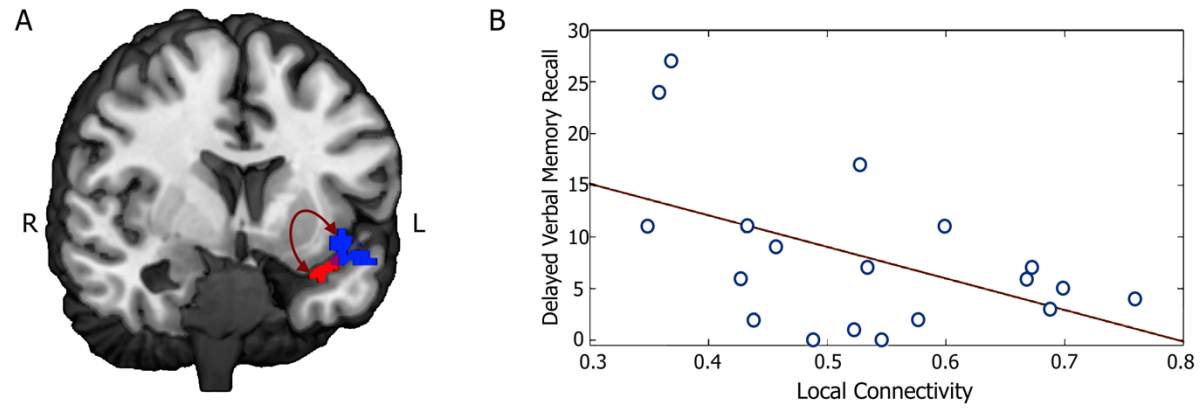

Figure 2-4: Abnormalities in functional connectivity correlate with patients' scores on the Logical Memory Delayed Recall task. (A) Connectivity of the dysregulated left temporal pole cluster (red) is increased with the neighboring temporopolar/insular/hippocampal region (blue) in patients compared to controls (**Table 2-3**, Cluster 1). **(B)** The strength of this local connection correlates negatively with patients' performance on the verbal memory task (r = -0.50, p = 0.030, N = 19).

Clusters with Constrained Dynamics Form a Less Efficient Network in Patients

Global efficiency of the 16-node network was significantly decreased in patients compared to controls, with one-sided 2-sample t-test $p < 0.05$ when varying over costs of 0.20, 0.25, and 0.3 (corresponding to 20, 25, and 30% of strongest connections kept; p = 0.011, p = 0.043, and p = 0.020, respectively). By thresholding at a certain cost we are in effect fixing the average degree of the network, so that the differences in graph measures presumably reflect changes in network topology. Nevertheless, it is important to note that there is no reliable and fully unbiased way of comparing networks, and that thresholding in this manner may convert non-significant values into edges for networks with low overall connectivity, and discard a number of significant connections for networks with high overall connectivity (van Wijk et al., 2010). We did not find significant between-group differences in other graph metrics tested.

Discussion

We found that patients with left TLE show slower time-series autocorrelation decay times in the left anterior temporal pole (proximal to the presumed epileptogenic zone) relative to decay times from the same region in healthy controls, indicating loss of complexity and more constrained functional dynamics. Decay time of the ACF discriminated successfully between patients and

healthy controls on a subject-by-subject basis in a purely data-driven manner, achieving accuracy of 100% in our sample of N = 19, and therefore showing potential for future validation as a neurodiagnostic tool for localization of epileptic foci.

Changes in BOLD time series complexity were accompanied by changes in local and global connectivity, with increased connectivity with neighboring temporo-frontal areas, and decreased connectivity with regions of the default mode network (DMN) and the contralateral temporal lobe. This result agrees with recent findings that complexity covaries with local connectivity (Anderson et al., 2014) as well as with recent independent component analysis-based findings that MTLE specific networks (which include temporal poles) show increased connectivity in patients, whereas the control-specific network (including thalamus and anterior cingulate cortex) shows decreased connectivity in patients (Maneshi et al., 2014).

Complexity of low frequency BOLD fluctuations has been shown to correlate significantly with local connectivity as measured by regional homogeneity (ReHo) (Anderson et al., 2014), implying that increased power spectrum scale invariance β (or, analogously, decreased autocorrelation function b values) may be a reflection of enhanced local synchronization. In addition, recent findings suggest that, relative to controls, unilateral MTLE patients show significantly increased regional homogeneity in the *ipsilateral parahippocampal gyrus*, but also in the *midbrain*, *insula*, *corpus callosum*, *bilateral sensorimotor cortex*, and *frontoparietal subcortical structures* (Zeng et al., 2013). This is in agreement with our findings of decreased ACF b values in a cluster within the *left temporal pole* and increased seed-to-voxel connectivity of this cluster towards neighboring areas, as well as with abnormal complexity found in the *inferior frontal gyrus*, *bilateral inferior parietal and postcentral area*, and *bilateral insula*.

The literature often reports structural changes in MTLE, which is most often accompanied by hippocampal sclerosis (HS), but also by (predominantly) ipsilateral atrophy of temporal pole and other temporolimbic structures (Coste et al., 2002). It is clinically well established that mesial temporal sclerosis may extend throughout the temporal lobe, and involve the cortex and the white matter, thus leading to extensive temporal lobe atrophy. Increased diffusion rate and decreased anisotropy have been observed in the epileptic focus, of TLE patients with unilateral HS (Assaf et al., 2003; Focke et al., 2008). Increased diffusion rate may be attributed to neuronal necrosis, gliosis, and expanded extracellular space, while the reduction in anisotropy may come from a loss of ordered structure, myelin degradation, and lowered cell density. Structural changes are often

non-localizing, and even non-lateralizing, including altered diffusion properties in the *contralateral temporal and inferior frontal lobes* (Focke et al., 2008) and widespread significant neocortical thinning in the *sensorimotor cortex* (Labate et al., 2011). Recurrent seizures and structural degeneration may lead to changes in functional connectivity as well: repair mechanisms (such as MMP-9) that degrade the matrix may facilitate local connections, while preventing long-range connections.

Out recent simulation studies show that power spectrum scale invariance varies as a function of both input type (excitatory versus inhibitory) and input density, with greater density of inhibitory or lower density of excitatory inputs producing constrained (less complex, more persistent) dynamics (Radulescu and Mujica-Parodi, 2014). Although epilepsy is often thought of as a hyper-excitatory disorder, this may not necessarily hold true during interictal periods (for example, it has been postulated that ictal epileptic neurphysiological activity can trigger local area neuronal network inhibition in attempt to stabilize the local neuronal network function (Tebartz van Elst et al., 2011)); constrained dynamics are, in fact, consistent with hubs with more inhibitory connections (Radulescu and Mujica-Parodi, 2014). Furthermore, it has been postulated that epileptogenesis may involve not just the creation of a hyperexcitable state, but also the existence of high connectivity state and non-Markovian recurrent loops (Hsu et al., 2007), in agreement with our finding that epileptogenic regions show higher local connectivity and exhibit longer time series memory (slower autocorrelation decay).

The *posterior cingulate cortex* (PCC) is a pivotal hub for integration and mediation of information in the brain (van den Heuvel and Sporns, 2011). It has been implicated in a range of functions, and shown to be a part of the *Default Mode Network* (DMN) and *Dorsal Attention Network*. It has strong reciprocal connections to *mesial temporal lobe* memory-related structures (Maddock et al., 2001). Our ACF-identified cluster showed decreases in connectivity with PCC, in agreement with a couple of recent studies showing diminished connectivity between PCC and bilateral mesial temporal structures in left MTLE patients (James et al., 2013; Liao et al., 2011). In addition, our findings suggest that there is a linear relationship between left temporal pole connectivity with PCC and epilepsy duration, over which the connection is restored over time. However, this restoration seems to be accompanied by aggravated decrease in connectivity with the opposite temporal lobe.

The Wechsler Memory Scale is one of the most commonly used memory tests in patients with epilepsy, and is often a part of standard pre-surgical evaluation. Patients with temporal lobe epilepsy have been found to have lower scores when compared to healthy controls, but the tests on their own have been unable to lateralize temporal epilepsy successfully (Helmstaedter et al., 2009; Soble et al., 2014). We found that local increase in connectivity of the dynamically constrained cluster in patients correlated negatively with scores on the Logical Memory Delayed Recall task suggesting, as expected, that more severe symptoms were associated with higher local connectivity. Therefore, local connectivity of the left temporal lobe ACF-identified region was not only increased in patients compared to controls, but was also associated with severity of verbal memory impairment within the patient population. This is not surprising considering that the disconnected cluster included parts of affected hippocampus, structure known to be heavily involved in memory processing.

Limitations and Future Directions

The current gold standard for localization of focal regions includes identification of an epileptogenic zone on intracranial EEG recordings combined with postoperative seizure freedom following its resection. Due to invasive nature of intracranial recordings and the extensive temporal duration required to establish seizure freedom with confidence, data of such nature are more restricted. In this study, we utilized data from nineteen patients with concordant clinical findings, including results of long-term video EEG monitoring and structural MRI abnormalities confirmed by an experienced neurologist. While this group serves as a benchmark for the application of the technique developed here, and comparisons of individual ACF b maps to the mean control map point to clinically relevant region in 100% of subjects, future work will address its applicability in subjects with other forms of epilepsy, ideally with the epileptogenic zone confirmed via invasive recordings. The method presented here is an alternative to multimodal methods such as EEG-fMRI, which has the advantage of not requiring electrophysiological setups incompatible with some head-coils, avoids extensive set-up times, is completely fMRI data-driven (avoiding assumptions with respect to the shape of the hemodynamic response function and modeling of epileptic events), and utilizes only ~seven minutes of resting state data without active patient participation. Our aim is to provide a first step towards a non-invasive method that reliably detects focal regions in patients with drug resistant focal epilepsy.

Conclusions

We developed techniques for the interictal identification of epileptic foci through complexity and network analyses of fMRI time-series. In a completely non-invasive and data-driven manner, based on complexity values calculated from resting-state fMRI images alone, we were able to achieve 100% accuracy in distinguishing between 19 healthy controls and 19 epileptic patients with well-defined left temporal epileptic foci. Our method has shown high sensitivity and specificity in localizing focal points, while providing additional information about the underlying dynamics of epileptic brains. Since the method does not explicitly depend on existence of MRI-detectable structural abnormalities, it could eventually be applied to patients with epileptic foci that are inadequately defined or poorly localized based on current state of the art neuroimaging techniques. Functional MRI analytical methods that target network dynamics therefore hold promise in providing novel and clinically valuable tools for the identification and resection of epileptogenic foci.

Chapter 3 Signal Fluctuation Sensitivity: An Improved Metric for Optimizing Detection of Resting-State fMRI Networks

Modified from DeDora, D. J.*, Nedic, S.*, Katti, P., Arnab, S., Wald, L.L., Takahashi, A., Van Dijk, K.R., Strey, H.H., Mujica-Parodi, L.R., 2016. *Signal Fluctuation Sensitivity: An Improved Metric for Optimizing Detection of Resting-State fMRI Networks*. Frontiers in Neuroscience 10, 180;

*DeDora, D. J. and Nedic, S. contributed equally to this work

Abstract

Task-free connectivity analyses have emerged as a powerful tool in functional neuroimaging. Because the cross-correlations that underlie connectivity measures are sensitive to distortion of time-series, here we used a novel dynamic phantom to provide a ground truth for dynamic fidelity between *blood oxygen level dependent* (BOLD)-like inputs and fMRI outputs. We found that the *de facto* quality-metric for task-free fMRI, *temporal signal to noise ratio* (tSNR), correlated inversely with dynamic fidelity; thus, studies optimized for tSNR actually produced time-series that showed the greatest distortion of signal dynamics. Instead, the phantom showed that dynamic fidelity is reasonably approximated by a measure that, unlike tSNR, dissociates signal dynamics from scanner artifact. We then tested this measure, *signal fluctuation sensitivity* (SFS), against human resting-state data. As predicted by the phantom, SFS—and not tSNR—is associated with enhanced sensitivity to both local and long-range connectivity within the brain's default mode network.

Introduction

Unprecedented investment in functional neuroimaging has ushered in a new era of brain research, in which fMRI's original role in mapping the areas of the brain most "active" under a task, now includes task-free characterization of brain connections and circuits. This evolution implies a fundamental—and yet largely unacknowledged—shift in how we understand *signal* versus *noise*.

During fMRI's first decade, researchers almost exclusively used stimulus presentation to evoke *blood oxygen level dependent* (*BOLD*) activity in subjects. To identify the relationship between different brain regions and their functional roles, tasks included one or more experimental conditions (*tasks*), as well as a baseline measure absent of stimuli (*rest*). FMRI time-series were then fitted to the expected hemodynamic shape for each condition (*canonical hemodynamic response function*, or *HRF*). Once fitted, trials for each condition were averaged and used to statistically compare hemodynamic amplitudes for each condition (*contrasts*) across subjects. Contrasts that met statistical thresholds were then represented as activity, producing activation maps. Importantly, the fitting, averaging, and subtraction approach used to analyze task-based data was designed to distinguish between time-series fluctuations originating from two sources. On the one hand, it amplified *fluctuations of interest* corresponding to task-based activation and that therefore were correlated with the experiment's design matrix. On the other hand, it suppressed *fluctuations of nuisance* that corresponding to (scanner, physiological) artifact and that therefore were independent of the experiment's design matrix.

In the late 1990's several influential papers (Biswal et al., 1997; Greicius et al., 2003; Raichle et al., 2001; Salvador et al., 2005) showed for the first time that the brain showed strong and reliable correlations between fMRI time-series even in the absence of a well-defined task (*resting-state connectivity*); more recently, the relationship between correlation-derived networks, and the neuronal events that underlie them, has been identified using fMRI acquired simultaneously with electrophysiological recordings of local field potentials (Logothetis et al., 2012). The fMRI community quickly responded, and today task-free *connectivity* studies—which map connections between brain nodes as defined by correlations between their time-series—comprise over 20% of human neuroimaging studies published every year (Bandettini, 2014). Connectivity analyses include not only those obtained by correlations with a pre-defined region (*seed-based*) but also those that describe graph-theoretic features of the functional connectome

(*complex network analyses*) (Bullmore and Sporns, 2009). Together, connectivity studies have contributed a wealth of new human brain data on aging (Damoiseaux et al., 2008), psychiatric (Greicius et al., 2007) and neurological (Bettus et al., 2009) disorders, and injury (Mayer et al., 2011). Resting-state fMRI protocols are easily standardized, require minimal patient compliance, and permit exploratory analyses; as such, they would appear to be well positioned for both clinical neurodiagnostics as well as large-scale international bio-repositories established for epidemiological research.

However, the transition from *activation maps* to *connections between nodes* not only produced a conceptual shift with respect to the role of functional neuroimaging, but also increased dependence upon time-series power spectra. The standard measure for establishing the quality of task-based data has been the *contrast-to-noise ratio (CNR)*, defined as the contrast (mean activation level acquired during task minus the mean activation level acquired during rest) divided by the standard deviation of the residual time-series (Bandettini and Cox, 2000). For task-free designs however, CNR cannot be computed, and thus normally is replaced by the *temporal signal-to-noise ratio* (*tSNR*), defined as the mean of the time-series divided by its standard deviation (Kruger et al., 2001). Intuitively, both CNR and tSNR compare the amplitude of a signal against a background of undesired physiological, thermal, and scanner noise present in all fMRI studies. This manner of conceptualizing what is "signal" versus what is "noise" makes perfect sense within the context of activation maps, in which a task activates the brain reliably more under one condition (signal) than another (noise) (Murphy et al., 2007). However, for task-free analyses, the "baseline" fluctuations themselves also include the "signal." Thus, for most task-free analyses, tSNR would appear to do exactly the opposite of what one would wish, as it penalizes sensitivity to the fluctuations (i.e., the standard deviation of the time-series) upon which experimental results are also based. Indeed, several recent studies have reported little correspondence between resting-state tSNR and the detection of stable functional networks (Gonzalez-Castillo et al., 2014; Molloy et al., 2014; Smith et al., 2013; Welvaert and Rosseel, 2013).

For task-free analyses, rather than relegate time-series fluctuations to the category of noise as per tSNR, we want to—as with task-based analyses—functionally distinguish between fluctuations of interest that are *neurobiologically significant* (e.g., emanating from BOLD signal consequent to neuronal response) from fluctuations of nuisance that are *neurobiologically insignificant* (e.g., physiological, scanner, and motion artifact). The dissociation between the two

can be characterized by *signal fluctuation sensitivity (SFS)*, which we define at a single-voxel level as:

$$SFS_{voxel} = \frac{\mu_{voxel}}{<\mu_{global}>} \times \frac{\sigma_{voxel}}{<\sigma_{nuisance}>} \qquad \text{(Equation 1)}$$

In the first term, the numerator consists of the mean signal (μ) of a time-series acquired from a voxel in the *region of interest* (*ROI*). For the denominator, we average over all voxel-specific signal for the entire brain (*global*). The first term ensures that SFS decreases for regions with signal drop out, while remaining unit-less (as with tSNR). In the second factor, the numerator consists of the standard deviation (σ) of the time-series acquired from the voxel of interest. For the denominator, we average over all voxel-specific σ from a region in which BOLD signals are not expected, but in which physiological, scanner, and motion artifacts are still present (*nuisance*). Prior work suggests that time-series obtained from cerebrospinal fluid (CSF) meet criteria for the *nuisance* denominator (Wald, 2012). SFS for a region of interest is then computed by averaging voxel-specific SFS values over all voxels in the region ($SFS_{ROI} = < SFS_{voxel} >_{ROI}$). In order to more easily compare SFS with tSNR, we scale them comparably by multiplying SFS values by 100.

We define *dynamic fidelity* as the degree to which fMRI accurately captures true BOLD fluctuations. In order to test our hypothesis that SFS should reflect dynamic fidelity of time-series more accurately that tSNR, we first needed to know the "ground truth" for those fluctuations. To access that ground truth, we designed and constructed a *dynamic phantom*, which provides user-controlled—and thus known—dynamic BOLD-like inputs to which fMRI-derived outputs can be compared. We then tested the impact of dynamic fidelity, as defined by our phantom, in predicting detection sensitivity to functional connectivity in human data across three different sets of acquisition parameters, chosen to represent a breadth of realistic optimization strategies utilized within the neuroimaging field for human connectivity studies.

Methods

For detailed description of design and prototyping of the dynamic phantom, please refer to (DeDora et al., 2016) – this part is omitted here. To understand the work presented here it suffices to say that the dynamic phantom is a fully automated, MRI-compatible device, capable of

producing BOLD-like signal. The device consists of two concentric cylinders: the inner (rotating) cylinder containing four compartments, divided longitudinally, filled with two different concentrations of agarose gel (2.21 and 2.27%), and a stationary outer cylinder filled uniformly with 2.27% agarose gel. The basis for the signal is the fact that the magnetic susceptibility of agarose gels is concentration dependent (Olsrud et al., 2008), in which higher concentrations produce lower fMRI signal. By varying the concentration of agarose gel present within a voxel over time, the dynamic phantom produces changes in T2* that can be tuned to amplitudes typically seen with BOLD in humans; the phantom can be programmed to simulate both task-based and resting-state BOLD-like signals. With known inputs, the relationship between the signal produced (by the dynamic phantom) and the signal detected (by the fMRI scanner) can be rigorously quantified as a measure of dynamic fidelity.

Using the Dynamic Phantom to Test SFS and tSNR

Acquisition parameters: We scanned the dynamic phantom in three separate MRI scanners. Detailed scan parameters are listed in **Table 3-1**. The three scanners utilized in this phantom study represent the following: (i) a 3T Siemens MRI with 32-channel head-coil (McGovern Institute for Brain Research, Massachusetts Institute of Technology), (ii) a 3T Siemens MRI with 64-channel head-coil (Human Connectome Scanner—Martinos Center for Biomedical Engineering, Massachusetts General Hospital), and (iii) a 7T Siemens MRI with 32-channel head-coil (Martinos Center for Biomedical Engineering, Massachusetts General Hospital). For each scanner, we tested three sampling rates, representing typical time-resolution for fMRI studies (TR = 2000-2010ms), increased time-resolution acquired for the Human Connectome Project (TR = 1010-1080ms), and ultra-fast imaging paradigms (TR = 802-824ms). Thus, we performed a factorial study (three scanners and three sampling rates each) with the dynamic phantom, for a total of nine scans (**Table 3-1**), each 10 minutes long. For both 3T scanners, we performed standard shimming; due to dramatically increased susceptibility artifacts at 7T, we utilized a partial shim centered on the inner cylinder of the phantom. Visual inspection of the resulting images, as well as correlations between the dynamic phantom inputs and fMRI outputs, confirmed data quality.

Scan	Main Field	Head Coil	TR (ms)	TE (ms)	SMS	iPAT	Flip Angle	Bandwidth (Hz/Px)	Resolution (mm)	Slice Gap (mm)	Slices
1	3T	32 Ch	2000	30	3	2	75°	1860	2x2x2	0.2	69
2	3T	32 Ch	1080	30	4	2	60°	1860	2x2x2	0.2	60
3	3T	32 Ch	802	30	5	2	33°	1860	2x2x2	0.2	55
4	3T	64 Ch	2000	30	2	2	85°	2840	2x2x2	0	62
5	3T	64 Ch	1080	30	4	2	60°	2840	2x2x2	0	68
6	3T	64 Ch	824	30	5	2	55°	2840	2x2x2	0	65
7	7T	32 Ch	2010	20	2	2	33°	2264	2x2x1.5	0	86
8	7T	32 Ch	1010	20	4	2	55°	2264	2x2x1.5	0	84
9	7T	32 Ch	802	20	5	2	33°	2368	2x2x1.5	0	85

Table 3-1: Acquisition parameters for the nine dynamic phantom scans. We tested three scanners at three TRs with the dynamic phantom. Highlighted rows indicate scans for which we collected corresponding human data, in which Scan 1 corresponds to Acquisition A, Scan 5 corresponds to Acquisition B, and Scan 9 corresponds to Acquisition C. All sequences utilized interleaved acquisition.

Statistical analyses: While most human fMRI data undergoes significant preprocessing, for the dynamic phantom we used raw data after implementing only voxel-wise trend removal (linear and quadratic) to remove scanner drift, and no further temporal preprocessing, in order to characterize dynamic fidelity as transparently as possible. For the *region of interest (ROI)* fluctuations, we extracted the average time-series from the four quadrants of the inner cylinder (corresponding to the four chambers, with respect to the initial position of the phantom) with an automated masking procedure using MATLAB software developed in-house. We repeated this for six slices positioned in the center of the phantom (n = 24 time-series per scan). For the *nuisance* fluctuations, we extracted the time-series from the outer cylinder of the phantom, which does not activate. We then computed quadrant-wise SFS based on the definition:

$$SFS_{dynamic\ phantom\ quadrant} = \frac{< \mu_{inner\ cylinder} >_{quadrant}}{< \mu_{global} >} \times \frac{< \sigma_{inner\ cylinder} >_{quadrant}}{< \sigma_{outer\ cylinder} >}$$

In the first term, the numerator consists of the mean signal (μ) of an averaged time-series over each of the four dynamic phantom quadrants (*quadrant*). For the denominator, we average over signal for the entire phantom (*global*). The first term ensures that SFS decreases for regions with signal drop out, while remaining unit-less (as with tSNR). In the second term, the numerator consists of the mean standard deviation (σ) of an averaged time-series over each of the four dynamic phantom quadrants. For the denominator, we average over σ from a region in which signals are not expected, but in which scanner artifacts are still present. In this case, we use the

outer cylinder, which is static. In order to avoid biasing values for standard deviation due to differences in the number of voxels between inner quadrants and outer cylinder, we averaged time-series in the outer compartment over the same number of voxels used to average time-series in each of the inner quadrants. We computed standard deviations for each of these inner quadrant-sized (39 voxel) averaged time-series, and then averaged across those standard deviations to produce the standard deviation for the entire outer cylinder (i.e., the denominator of the second factor). In order to more easily compare SFS with tSNR, we scale them comparably by multiplying SFS values by 100. TSNR was computed as the mean for the averaged time-series over each of the four dynamic phantom quadrants, divided by its standard deviation (after detrending). Dynamic fidelity was computed as the correlation between inputs (dynamic phantom user-defined function) and outputs (fMRI time-series). We then computed the correlation between fidelity and both SFS and tSNR for each of the 24 time-series per scan.

Human Scanning

Acquisition: In an effort to represent a wide variety of task-free scanning paradigms, we analyzed three sets of human data (N = 12 subjects each) collected with the same acquisition parameters utilized for the phantom studies, but using only the time-resolutions previously optimized for each study (**Table 3-1**). Thus, *Acquisition A* refers to the 3T MRI with 32-channel head-coil and a TR = 2000ms; *Acquisition B* refers to the 3T MRI with a 64-channel head-coil and a TR = 1080ms, and *Acquisition C* represents the 7T MRI with a 32-channel head-coil with a TR = 802ms. *Acquisition A* lasted 5 minutes, while *Acquisition B* (originally 6.2 minutes) and *Acquisition C* (originally 10 minutes) data were truncated to match this duration. Anterior to posterior phase encoding and interleaved acquisition were used in all scans. For *Acquisition A*, we acquired whole-brain T1-weighted structural volumes using a conventional MPRAGE sequence with the following parameters: TR = 2530ms, TE = 3.39ms, TI = 1100ms, flip angle = 7°, voxel size = 1 x 1 x 1.3mm. Conventional B0 field maps derived from phase differences between gradient echo images acquired at TR = 4.22 and 6.68ms were also acquired (TR = 584ms, flip angle = 55°, voxel size = 2 x 2 x 2 mm, slice gap = 0.2mm, 69 slices). For *Acquisition B*, we also acquired whole-brain T1-weighted structural volumes using a conventional MPRAGE sequence with TR = 2530ms, TE = 1.15ms, TI = 1100ms, flip angle = 7°, 1mm isotropic voxel size. For *Acquisition C*, we acquired whole-brain T1-weighted structural volumes using a multi-echo MPRAGE

(MEMPRAGE) sequence with four echoes and the following protocol parameters: TR = 2530ms, TE1 = 1.61ms, TE2 = 3.47ms, TE3 = 5.33ms, TE4 = 7.19ms, TI = 1100ms, flip angle = 7°, 1mm isotropic voxel size. Conventional B0 field maps derived from phase differences between gradient echo images acquired at TE = 4.60 and 5.62ms were also acquired (TR = 723ms, flip angle = 36°, voxel size = 1.7 x 1.7 x 1.5 mm, 89 slices).

All human subject studies were approved by the Institutional Review Boards of institutions at which subjects were tested (Massachusetts Institute of Technology for *Acquisition A*, Massachusetts General Hospital for *Acquisitions B* and *C*). All subjects were healthy adults, had full capacity, and provided informed consent.

All subjects were age matched ($\mu_A = 25.6 \pm 3.7$; $\mu_B = 23.3 \pm 4.2$; $\mu_C = 25.6 \pm 3.4$, $p = 0.35$, Kruskall-Wallis test). There were no significant differences in motion across the three groups (maximum absolute translation $p = 0.60$, maximum absolute rotation $p = 0.96$, mean root mean square (RMS) motion $p = 0.10$, maximum RMS motion $p = 0.27$, Kruskall-Wallis test). All participants were instructed to lie quietly with eyes open in the scanner, orienting to a fixation cross, without moving for the duration of the scan. We removed the first ten seconds of data for all datasets.

Preprocessing: We followed the standard SPM8 (http://www.fil.ion.ucl.ac.uk/spm/) pipeline for realignment, co-registration to a structural image, and normalization to Montreal Neurological Institute (MNI) space. Co-registered structural images were segmented into probabilistic maps of gray matter, white matter, and CSF using SPM's New Segment tool. Where noted, we utilized a 4-mm (2 voxel) FWHM Gaussian smoothing kernel. As per standard practice for fMRI analyses, we performed slice time correction only on *Acquisition A* data, since the 2000ms sampling rate was considerably slower than those of the other two scanners. We performed field map correction on *Acquisitions A* and *C* (distortion correction scheme was performed on *Acquisition B* immediately following image acquisition). Scrubbing was performed to remove the influence of motion, with scan-to-scan global signal deviation from the mean > 3 and scan-to-scan composite motion > 0.5 mm as thresholds for removal (Power et al., 2012). The mean percentage of data points removed between all three groups was 1.97%, with no subjects having more than 9% of data scrubbed. To assess the impact of spatial smoothing, we computed all of our measures on both unsmoothed and smoothed data, both of which underwent each of the other preprocessing steps listed here.

Computation of SFS, tSNR, ALFF, ReHo and Long-Range (mPFC-PCC) Connectivity

We used MATLAB to compute voxel-wise SFS according to:

$$SFS_{voxel} = \frac{\mu_{default\ mode\ network\ ROI}}{<\mu_{global}>} \times \frac{\sigma_{default\ mode\ network\ ROI}}{<\sigma_{cerebrospinal\ fluid}>}$$

In the first term, the numerator consists of the mean signal (μ) of a time-series acquired from a voxel in the *region of interest (ROI)* in the default mode network, as defined below. For the denominator, we average over all voxel-specific signal for the entire brain (*global*). The first term ensures that SFS decreases for regions with signal drop out, while remaining unit-less (as with tSNR). In the second term, the numerator consists of the standard deviation (σ) of a time-series acquired from the voxel of interest in the default mode network, as defined below. For the denominator, we average over all voxel-specific σ from a region in which BOLD signals are not expected, but in which physiological, scanner, and motion artifacts are still present (*nuisance*). Prior work suggests that time-series obtained from cerebrospinal fluid (CSF) meet criteria for the *nuisance* denominator (Wald, 2012). SFS for a region of interest is then computed by averaging voxel-specific SFS values over all voxels in the region. We additionally computed voxel-wise tSNR as the mean for each voxel's time-series divided by its standard deviation. In order to more easily compare SFS with tSNR, we scale them comparably by multiplying SFS values by 100.

For SFS, standard deviations of the cerebrospinal fluid voxels (*nuisance fluctuations*) were computed using an eroded probabilistic map of CSF (SPM8 segmented map of CSF thresholded at 70%), to ensure minimal contributions from neural sources. To avoid distorting time-series dynamics by averaging them, standard deviations were computed for each voxel in the nuisance ROI, with voxel-based values averaged for the ROI. Mean global signal included the entire brain (conjunction of gray matter, white matter, and cerebrospinal fluid, thresholded at 70%). Mean values and standard deviations for each voxel were acquired before confound correction, but after SPM8 preprocessing and scrubbing.

Prior to functional connectivity analyses, we performed further regression of nuisance variables (confound-correction). This included detrending, regression of mean CSF and white matter signals (white matter map thresholded at 70%), and regression of six motion parameters from the realignment step. Finally, we performed temporal band-pass filtering in the 0.01-0.1 Hz range using 5th order Butterworth filter.

Both *amplitude of low frequency fluctuations (ALFF)* and local synchronization of neighboring voxels (*regional homogeneity* or *ReHo*: 27-voxel KCC-ReHo) were computed from confound-corrected data, using the REST toolbox (Song et al., 2011). Resulting subject-specific voxel-wise ReHo and ALFF maps were standardized by dividing each voxel's value by the mean value of the whole brain. To test whether SFS or tSNR were predictive of these established resting-state measures, we computed within-subject correlations between (i) SFS and ALFF, (ii) SFS and ReHo, (iii) tSNR and ALFF, and (iv) tSNR and ReHo for voxels belonging to the well-established *default mode network* (DMN) regions: *medial prefrontal cortex* (*mPFC*)*, posterior cingulate cortex* (*PCC*), and *left and right lateral parietal cortices* (*LLP* and *RLP*). These regions were defined as 10-mm radius spheres centered on previously established coordinates (Fox et al., 2005), intersected with an SPM8 brain mask to ensure only brain voxels were included. For the extraction of ROI-based SFS and tSNR values, we used the four aforementioned DMN masks, as well as a probabilistic gray matter mask from SPM8 ($P > 50\%$). We obtained subcortical ROI masks from bilateral regions included in FSL Harvard-Oxford subcortical atlas (thresholded at 50%).

As a measure of long-range mPFC-PCC connectivity strength we used Fisher-z transformed correlations coefficients between mean time series extracted for mPFC and PCC. To test whether SFS or tSNR were predictive of the mPFC-PCC connection strength, we computed between-subject correlations (N = 36) between the minimum SFS or tSNR for each mPFC-PCC pair and connectivity strength. The decision to use the SFS or tSNR value for the system as a whole based upon the minimum value is intuitively based upon the intuition that for networks that include two or more nodes, signal for the network as a whole can only be as strong as that of its weakest node. However, this intuition is not completely accurate; it is only a better solution than the next easiest option, which is to take the mean.

Results

Dynamic Phantom Assessment of SFS vs tSNR in Predicting Dynamic Integrity

The dynamic phantom was programmed to mimic resting-state oscillations observed in human fMRI (van den Heuvel et al., 2008) (**Figure 3-1A**), and scanned under three different sets of acquisition parameters. *Acquisition A* represents what would normally be considered the standard for typical resting-state studies, using a 3T scanner with 32-channel head coil and 2000ms

temporal-resolution (TR). *Acquisition B* uses a set of parameters that were specifically designed for resting-state connectivity analyses as part of the *Human Connectome Project.* These include a 3T scanner that increases the temporal-resolution to 1080ms to achieve greater sensitivity to fluctuation dynamics; to compensate for signal loss associated with accelerated scanning, *Acquisition B* uses a custom-built 64-channel head coil. *Acquisition C* pushes even further than *Acquisition B* in optimizing over temporal resolution (802ms). *Acquisition C* retains the 32-channel head coil, but compensates for signal loss associated with accelerated scanning by increasing the field strength to 7T. Scanners and scan parameters used for each session are described in **Table 3-1**. For human data, we also acquired T1-weighted structural images and B0 field maps for correction of EPI data.

We then computed dynamic fidelity, SFS, and tSNR on raw data acquired from the dynamic phantom. Standard deviations were computed after voxel-wise removal of linear and quadratic trends. The dynamic phantom is longitudinally divided into four chambers, and rotates about the long axis orthogonally to the main field. For our *region of interest*, we extracted the average time-series from each the four quadrants of the inner cylinder with an automated masking procedure, and repeated this for six slices positioned in the center of the dynamic phantom (N = 24 time-series per scan). *Dynamic fidelity* was defined as the correlation between user-defined *dynamic inputs*, provided by the phantom rotation, and *dynamic outputs* acquired from the scanner in the region of interest. To compute the *nuisance* term within SFS (analogous to CSF in humans), we extracted fluctuations acquired from the outer cylinder in these six slices, which includes only inactive voxels.

Dynamic fidelity *directly* correlated with SF*S* for each of the nine scans (**Figure 3-1B**; **Table 3-2**; median $r = 0.67$) and *inversely* correlated with tSNR for each of the nine scans (**Figure 3-1B**; **Table 3-2**; median $r = -0.63$). Thus, when the scanner was most sensitive in capturing dynamic inputs, SFS was maximized while tSNR was minimized, and vice-versa. Researchers typically optimize acquisition parameters for fMRI connectivity studies by trying to maximize tSNR. Yet doing so would appear to produce the greatest amount of distortion for the BOLD fluctuations upon which connectivity results are based. Thus, we tested the implications of our dynamic phantom results for human connectivity studies.

	TR (ms)	3T, 32 Ch	3T, 64 Ch	7T, 32 Ch
		Correlation with Dynamic Fidelity		
SFS	~2000	0.51 ($p = 0.010$)	0.69 ($p = 2.1 \times 10^{-4}$)	0.54 ($p = 6.6 \times 10^{-3}$)
	~1080	0.71 ($p = 1.1 \times 10^{-4}$)	0.76 ($p = 1.8 \times 10^{-5}$)	0.69 ($p = 1.9 \times 10^{-4}$)
	~802	0.67 ($p = 3.7 \times 10^{-4}$)	0.49 ($p = 0.014$)	0.63 ($p = 9.0 \times 10^{-4}$)
tSNR	~2000	–0.67 ($p = 3.2 \times 10^{-4}$)	–0.64 ($p = 7.0 \times 10^{-4}$)	–0.44 ($p = 0.030$)
	~1080	–0.87 ($p = 4.6 \times 10^{-8}$)	–0.72 ($p = 8.3 \times 10^{-5}$)	–0.58 ($p = 3.0 \times 10^{-3}$)
	~802	–0.63 ($p = 1.1 \times 10^{-3}$)	–0.27* ($p = 0.20$)	–0.54 ($p = 6.2 \times 10^{-3}$)

Table 3-2: Dynamic fidelity for dynamic phantom scans. Dynamic fidelity in all nine scans was positively correlated with SFS and negatively correlated with tSNR. *n.s.

Human Subjects Assessment of SFS vs. tSNR in Detecting Resting-State Connectivity

We calculated SFS and tSNR in human neuroimaging data acquired using *Acquisitions A*, *B*, and *C* (restricting our analyses to the *TR* originally, and independently, optimized for each scanner), and assessed the utility of each in predicting detection sensitivity to resting-state network features. Human data were preprocessed according to standard methods, including the SPM8 preprocessing pipeline; to gauge the impact of spatial smoothing, we calculated all values both with and without this step. After preprocessing, we used MATLAB to compute SFS and tSNR as per Equation (1). For resting-state connectivity, we computed three commonly used measures. The first was the between-voxel measure of local connectivity, *regional homogeneity* (*ReHo*) (Zang et al., 2004). The second was the within-voxel *amplitude of low-frequency fluctuations* (*ALFF*) (Zang et al., 2007), which is thought to underlie resting-state connectivity (Biswal et al., 1995). The third was *long-range connectivity* between two nodes of the default model network (Raichle, 2015): the *medial prefrontal cortex* and the *posterior cingulate cortex* (mPFC-PCC). DMN regions were defined as 10mm radius spheres centered upon previously established coordinates (Fox et al., 2005). Long-range connectivity forms the basis for graph theoretic/complex network analyses (Bullmore and Sporns, 2009) used within the fMRI field .

To test the degree to which SFS and tSNR were sensitive to well-established resting-state features, we computed correlations between SFS and ReHo, ALFF, and long-range connectivity; as well as tSNR and ReHo, ALFF, and long-range connectivity. ReHo and ALFF were computed for voxels within the well-established default mode network, comprised of the *medial prefrontal cortex*, *posterior cingulate cortex*, and *bilateral parietal cortices* (**Figure 3-2A**).

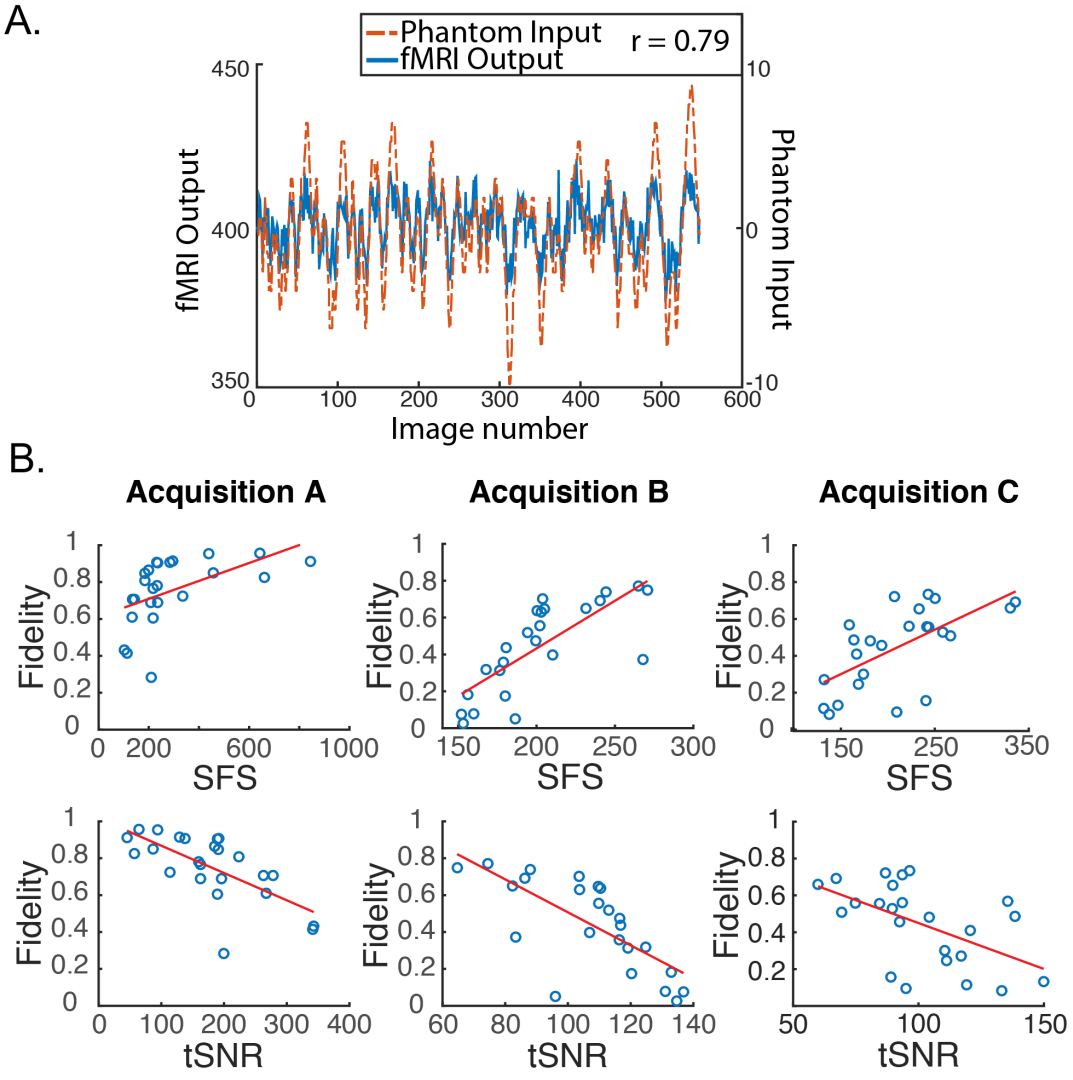

Figure 3-1: Dynamic phantom results show that dynamic fidelity positively correlates with signal fluctuation sensitivity (SFS) and negatively correlates with classical temporal signal to noise ratio (tSNR). (A) To accurately mimic human resting-state fluctuations in the dynamic phantom, we utilized a complex pink-noise waveform as shown by the dotted line. The 10-minute input function originated from our previous neuroimaging data and was subsequently programmed into the phantom. The dynamic phantom inputs are derived from position tracking during rotation. A representative output fMRI signal is superimposed (*fMRI Output* axis), as acquired under *Acquisition B*: 3T magnet, 64 Channel head-coil, at TR = 1080ms (see **Table 3-1**). This waveform input was used for all nine phantom fMRI scans. **(B)** Input-output fidelity was positively correlated with SFS (median r = 0.67, see **Table 3-2**) and negatively correlated with tSNR (median r = -0.63, see **Table 3-2**). Groups presented here match the scanning parameters presented in the subsequent human data: *Acquisition A* is a 3 Tesla magnet with a 32-channel headcoil (TR = 2000ms), *Acquisition B* is a 3 Tesla magnet with a 64-channel headcoil (TR = 1080ms), and *Acquisition C* is a 7 Tesla magnet with a 32-channel head coil (TR = 802ms). **Table 3-1** provides detailed acquisition parameters for each scan, while **Table 3-2** provides detailed results from all nine dynamic phantom scans.

Long-range connectivity focused upon the two-node MPFC-PCC connection, which we found to be reliable across subjects within our dataset (33 out of 36 subjects showed significant positive correlation between mean time series from these two regions). For networks that include two or more nodes, we used the minimum SFS or tSNR for each mPFC-PCC pair.

We first tested whether SFS and tSNR would predict local connectivity (ReHo) at a single-subject level. Without smoothing, region-specific correlations within the *default mode network* showed robust positive relationships between SFS and ReHo (median $r = 0.53$: 96% $p < 0.05$, 95% $p < 0.01$, 94% $p < 0.001$; by acquisition set: $r_A = 0.54$, $r_B = 0.51$, $r_C = 0.54$; see **Figure 3-2B** for median across subjects and default mode network regions). In contrast, the correlation between tSNR and ReHo was either non-significant or significant but negative within most subjects' default mode network regions (median $r = -0.24$: 80% $p < 0.05$, 76% $p < 0.01$, 68% $p < 0.001$—even using the most liberal threshold of $p < 0.05$, only 11% of all correlations were positive between tSNR and ReHo; by acquisition set: $r_A = -0.42$, $r_B = -0.20$, $r_C = -0.06$; see **Figure 3-2C** for median across subjects and default mode network regions). Smoothing only magnified this effect. After smoothing, SFS positively correlated with ReHo (median $r = 0.68$: 98% $p < 0.05$, 98% $p < 0.01$, 98% $p < 0.001$; by acquisition set: $r_A = 0.69$, $r_B = 0.72$, $r_C = 0.55$) and tSNR negatively correlated with ReHo (median $r = -0.62$: 97% $p < 0.05$, 97% $p < 0.01$, 97% $p < 0.001$; by acquisition set: $r_A = -0.72$, $r_B = -0.60$, $r_C = -0.57$). The same relationship was preserved when looking at the entire group ($N = 36$). The correlation between SFS and ReHo was $r = 0.39$, $p = 0.02$ (removing two outliers two *SD* ± the mean: $r = 0.52$, $p = 0.002$), while the correlation between tSNR and ReHo was $r = -0.04$, $p = 0.83$ (removing the same two outliers: $r = -0.03$, $p = 0.88$).

While ReHo is a measure of between-voxel local connectivity, ALFF is a single-voxel measure that estimates the total power of the low frequency component of an fMRI signal. Thus, we expected the relationship between ALFF and SFS (both single voxel measures) to be even more robust than the relationship between SFS and ReHo. Indeed, SFS strongly correlated with ALFF (median $r = 0.82$, all p's < 0.001; by acquisition set: $r_A = 0.90$, $r_B = 0.71$, $r_C = 0.77$), whereas tSNR was negatively correlated with ALFF (median $r = -0.70$, all p's < 0.001; by acquisition set: $r_A = -0.82$, $r_B = -0.65$, $r_C = -0.58$). Again, smoothing magnified this effect for both SFS (median $r = 0.93$, all p's $<< 0.001$; by acquisition set: $r_A = 0.94$, $r_B = 0.92$, $r_C = 0.93$), and tSNR (median $r =$

–0.84, all p's << 0.001; by acquisition set: r_A = –0.86, r_B = –0.83, r_C = –0.84). Again, the same relationship was preserved when looking at the entire group (N = 36). The correlation between SFS and ALFF was $r = 0.74$, $p = 0.03 \times 10^{-7}$, while the correlation between tSNR and ALFF was $r = -0.19$, p = 0.26.

As a measure of long-range connectivity, we tested SFS and tSNR against the default mode network's MPFC-PCC connection (Fisher-z normalized) across our three datasets (N = 36). Consistent with the other connectivity measures, SFS positively correlated with MPFC-PCC connectivity ($r_{A,B,C}$ = 0.61, $p = 8.65 \times 10^{-5}$) and tSNR negatively correlated with MPFC-PCC connectivity ($r_{A,B,C}$ = –0.73, $p = 4.46 \times 10^{-7}$). As with previous measures, smoothing did not qualitatively change the results for either SFS ($r_{A,B,C}$ = 0.40, p = 0.015) or tSNR ($r_{A,B,C}$ = –0.70, $p = 1.67 \times 10^{-6}$).

SFS and tSNR Values Between Acquisition Sets

The purpose of sensitivity metrics, for any measurement, is to provide accurate feedback by which parameters can be tuned to optimize performance, as well as to aid in the interpretation and artifact-correction of results. Our three representative acquisition strategies illustrate clearly the practical importance of using SFS rather than tSNR when optimizing fMRI studies for task-free analyses, and therefore dynamic fidelity. We compared SFS and tSNR values between acquisition paradigms for the default mode network, subcortical regions critical to the emotion and reward circuits, and global gray matter. Because human studies normally utilize smoothing, and because our previous analyses (above) showed comparable results for smoothed and unsmoothed results, **Figure 3-3** results include only 4-mm smoothed data. To directly compare SFS and tSNR values between acquisition sets, we extracted average values from the four regions of the *default mode network* and three subcortical regions (*amygdala*, *caudate*, *hippocampus)*, as well as *average subcortical* and *average gray matter*. Each subcortical region was defined from FSL Harvard-Oxford Subcortical Atlas and *average subcortical* includes *bilateral accumbens*, *amygdala*, *caudate*, *hippocampus*, *pallidum*, *putamen*, and *thalamus*. The *gray matter* mask was defined as SPM's probabilistic gray matter map thresholded at $P > 0.5$.

As shown in **Figure 3-3A-D**, SFS identifies advantages for dynamic fidelity in increasing temporal resolution, as well as the costs and benefits associated with increasing the number of head-coil channels vs. field strength to recover signal loss from accelerated acquisition. In general,

the ultra-dense head-coil strategy employed by *Acquisition B* optimizes dynamic fidelity in cortical regions, whereas the ultra-high-field strategy employed by *Acquisition C* optimizes dynamic fidelity in subcortical regions. TSNR provides a very different story: showing the greatest stability in *Acquisition A*, diminished performance in *Acquisition B*, and the worst performance in *Acquisition C*. Which strategy is ideal, for any particular study, therefore depends critically upon the scientific questions to be asked: not only with respect to the regions of interest implicated, but also the types of analyses to be performed.

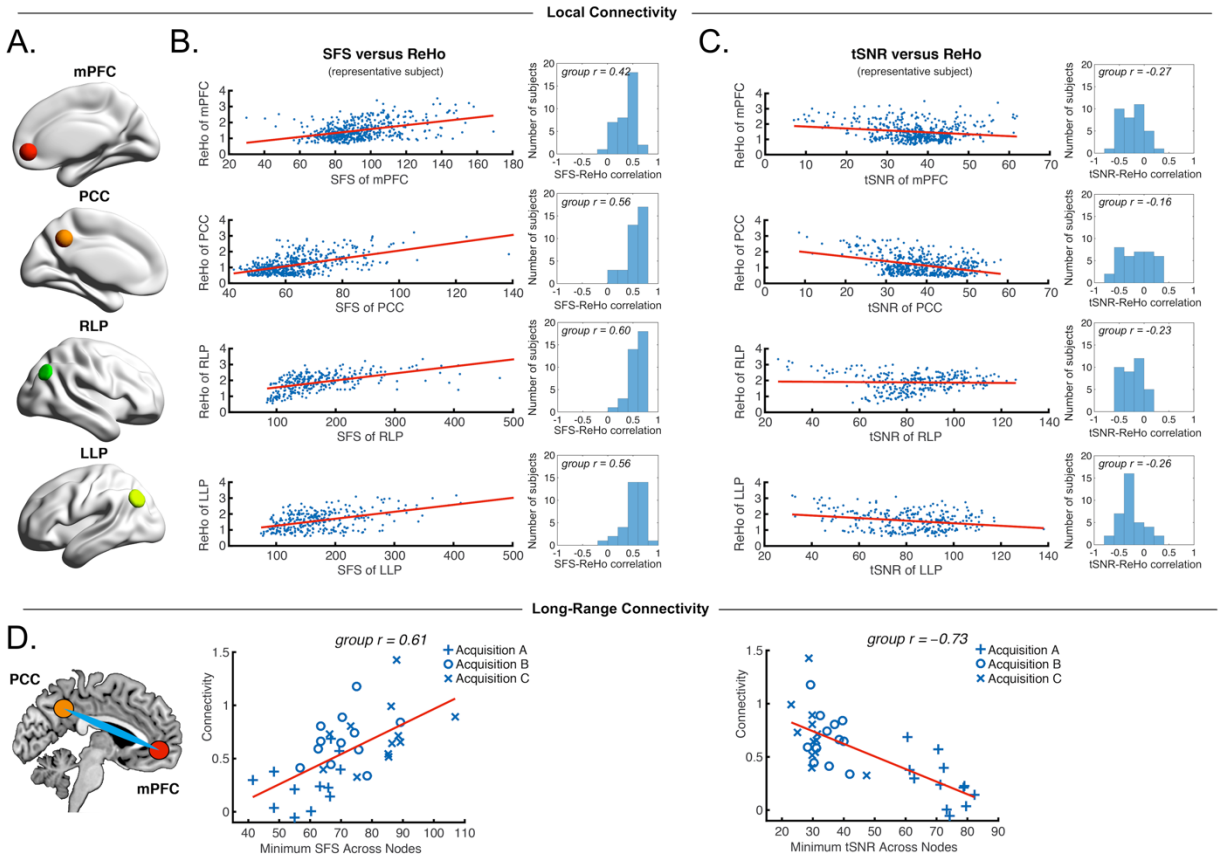

Figure 3-2: Local and long-range functional connectivity across the default mode network positively correlates with SFS and negatively correlates with tSNR. (A) We calculated SFS regional homogeneity (ReHo, a commonly used measure of neural synchrony in fMRI) for each individual subject across the *medial prefrontal cortex* (*mPFC*), *posterior cingulate cortex* (*PCC*), and *right* and *left lateral parietal lobes* (*RLP* and *LLP*). **(B,C)** Within-subject detection sensitivity for ReHo positively correlates with SFS and negatively correlates with tSNR (scatter plots shown for a single representative subject; group *r* for N = 36). **(D)** We see that the same pattern occurs for long-range connectivity between default mode network regions medial prefrontal cortex (*mPFC*) and posterior cingulate cortex (*PCC*) between subjects. As spatial smoothing artificially increases ReHo by producing correlations between contiguous voxels, shown data are unsmoothed.

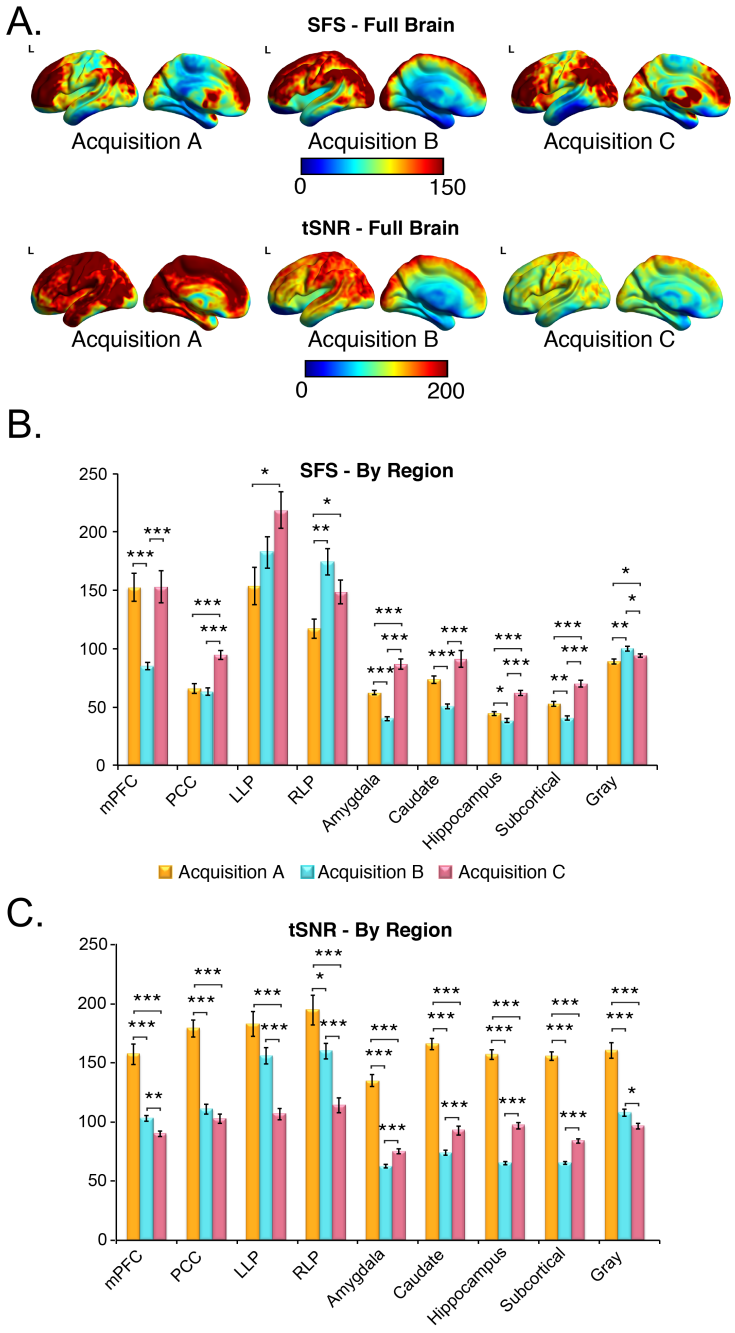

Figure 3-3: SFS distributions across the brain illustrate qualitative differences in sensitivity between acquisition strategies. As before, *Acquisition A* is a 3 Tesla magnet with a 32-channel head coil (TR = 2000ms), *Acquisition B* is a 3 Tesla magnet with a 64-channel head coil (TR = 1080ms), and *Acquisition C* is a 7 Tesla magnet with a 32-channel head coil (TR = 802ms). **(A)** Full brain SFS maps for each acquisition demonstrate that cortical (especially prefrontal and parietal/visual) SFSs are robust across all acquisitions. Acquisition B shows more uniform cortical SFS than A or C, while Acquisition C shows greater subcortical SFS than A or C. **(B)** SFS values across acquisition strategies averaged within several regions, including the default mode network, subcortical regions, and gray matter. In general, SFS was maximized in cortical regions for acquisition B and subcortical regions for acquisition C. **(C)** Acquisition A demonstrated the highest tSNR for all regions, followed by acquisition C and acquisition B. Values were derived from preprocessed and smoothed resting-state data (N = 12 per group, 5 min of data). *p < 0.05, **p < 0.01, ***p < 0.001 (Wilcoxson rank sum test).

Discussion

Functional neuroimaging has ushered in a new era of brain research, in which task-free fluctuations play an increasingly large role. As such, we need to reconsider whether fMRI optimization paradigms that rely solely on maximizing stability might actually be leading us astray, by failing to functionally dissociate fluctuations underlying signal versus those underlying noise. Here we propose a new measure—*Signal Fluctuation Sensitivity* (*SFS*)—that distinguishes between neurobiologically-relevant fluctuations of interest, and nuisance fluctuations due to physiological or scanner artifact. We demonstrate that SFS positively—and tSNR negatively—correlates with dynamic fidelity in a dynamic phantom, as well as with the detection power of local and long-range functional networks in humans, across three sets of representative acquisition parameters independently optimized for human fMRI studies. Future validation of SFS would benefit from a biological ground truth for measurement of dynamic fidelity, using simultaneous inputs recorded from local field potentials and their associated hemodynamic responses, combined with outputs obtained from fMRI time-series.

For dynamic analyses, the structure of the SFS equation reflects the equally important need to optimize over signal amplitude (provided by the mean) and signal change (provided by the standard deviation). In our datasets, we found that the relationship between SFS versus tSNR and long-range connectivity was driven primarily by the standard deviation component of each equation (including only the standard deviation ratio component of the SFS equation, correlations were $r_{A,B,C} = 0.68$, $p = 4.34 \times 10^{-6}$ for N=36; unsmoothed), while the mean signal component (including only the mean amplitude of signal or the ratio of the mean amplitude to global amplitude) showed no statistical relationship to long-range connectivity strength ($r_{A,B,C} = -0.18$, $p = 0.31$; $r_{A,B,C} = 0.02$, $p = 0.90$). However, our fMRI data had minimal signal drop out in regions of interest, which is not always the case. While the mean amplitude of the signal did not play a role in evaluating our data set, nevertheless this term of the SFS equation should be retained to avoid assigning high SFS to areas of the brain that show signal loss.

In developing SFS for humans, one important decision is the optimal location for the acquisition of *nuisance* fluctuations. We chose *cerebrospinal fluid*, rather than surrounding air, white matter, or whole brain, because time-series from the cerebrospinal fluid contain the greatest

proportion of nuisance variance of the three brain compartments (Wald, 2012), including motion, scanner variance, and some physiological effects. Moreover, unlike white matter (Gawryluk et al., 2014) and the global signal, the eroded CSF masks used here are unlikely to contain neurobiologically-relevant fluctuations of interest.

In extending our phantom results to the brain, we faced the problem of what to look for as a measure of validation, since we lacked the phantom's advantage of known inputs. Thus, we used highly conservative and well-replicated connections in order to evaluate detection sensitivity for resting-state data: a measure of local-connectivity (*regional homogeneity – ReHo (Zang et al., 2004)*), a single voxel measure of resting-state signals (*amplitude of low frequency fluctuations – ALFF* (Zang et al., 2007)), and the *long-range connection* between two nodes within the default mode network (*medial prefrontal cortex* and *posterior cingulate cortex* (Raichle, 2015)). Both ALFF and ReHo have been widely used to study resting-state brain activity, with clinical applications to Parkinson's disease (Wu et al., 2009), Alzheimer's disease (Liu et al., 2008), and psychiatric illnesses (Han et al., 2011). Likewise, identification of the default mode network via long-range connectivity represents a fundamental finding in neuroscience (Raichle, 2015), with direct implications for neurodevelopment and aging. Although the correlations for SFS and tSNR were both significant but of opposite sign, it is critical to note that they are not trivially inverses of one another. From a theoretical perspective, SFS and tSNR differ fundamentally in their dissociation of fluctuations of interest versus those of nuisance. From a practical perspective, **Figure 3-3** demonstrates that the two measures provide qualitatively different mapping of optimization over the brain. Thus, we demonstrate that, by optimizing for *dynamic fidelity* rather than the current standard of *dynamic stability*, SFS can have direct practical applications for markedly increasing detection sensitivity of clinical neuroimaging results.

Although we have emphasized the application of SFS to correlational analyses due to their increasing prevalence within the field, it is important to note that other types of task-free analyses will also be much better served by optimization to SFS than tSNR. This category of analyses includes those based upon power spectra and complexity (e.g., *ALFF*, *power spectrum scale invariance*, *entropic analyses*, *spectral dynamic causal modeling*), which also are more highly sensitive to subtle dynamic features of the time-series than are traditional contrast-based analyses. Consistent with these approaches, one additional area for future exploration is whether the principles underlying SFS can be applied not only for optimization, but also to identify neural

activity for task-free paradigms. The ability to dissociate signal fluctuations from noise fluctuations may be fruitful when the aim is to map the strength and location of task-free brain responses, rather than their connectivity.

Finally, while we have focused here on presenting limitations of CNR and tSNR, we wish to emphasize that both may still be useful and accurate measures in answering particular questions. Temporal SNR is a measure of signal stability that is proportional to field strength, voxel size, and sampling rate (Kruger et al., 2001; Triantafyllou et al., 2005); thus, in static phantoms, tSNR can be used to quantify and minimize scanner-related noise. If the primary aim of a study is to show contrast between two conditions then CNR, and not SFS, is correct. For task-free analyses, however, CNR is not directly measurable; thus, classical tSNR is normally cited as a surrogate (Smith et al., 2013; Van Dijk et al., 2012). It is in this case that using tSNR as guide will minimize, rather than maximize, detection sensitivity. As with so many zero-sum decisions in fMRI acquisition, it is important to realize that we optimize over one parameter at the expense of the other. Therefore, just as tuning of acquisition parameters benefits enormously from knowing *a priori* the region of interest to be targeted, knowing *a priori* the type of analysis to be performed will permit researchers decide whether to optimize for stability (tSNR) or for dynamics (SFS).

Chapter 4 Signal Fluctuation Sensitivity Identifies Brain Activity in Naturalistic-Task fMRI

Modified from Nedic, S. and Mujica-Parodi, L.R., 2017. *Signal Fluctuation Sensitivity Identifies Brain Activity in Naturalistic-Task fMRI* (under review)

Abstract

Neuroimaging during naturalistic tasks, such as watching a movie or navigation through virtual reality, allows more realistic simulation of real-world environments than do block or event-related designs. However, unstructured tasks represent a challenge from the data-analysis perspective, as they fail to provide knowledge of the design matrix (as required by general linear model-based methods) or consistent task trajectories across subjects (as required by inter-subject correlation-based methods). In the context of task-free designs, one method used to explore brain activity is the *amplitude of low-frequency fluctuations* (ALFF). Here we extend ALFF to naturalistic tasks using *signal fluctuation sensitivity* (SFS), a measure that dissociates functionally relevant signal dynamics from scanner-induced nuisance fluctuations. We show that it may be used as a data-driven technique to identify neural activity in naturalistic task paradigms by direct comparison with resting-state fMRI in same subjects. We find that, in three independent fMRI datasets employing three different highly complex naturalistic stimuli (scenes from a nature documentary, a television drama, and an iterative neuroeconomic game), SFS reliably identifies task-induced brain activity. Areas identified as having significantly higher SFS values during task relative to rest were confirmed as corresponding to task-induced activations by comparison to existing literature on similar tasks (similar content but with contrast-based designs), near-perfect correlation of the bilateral orbitofrontal cortex with dynamic ratings of emotional arousal/valence (r = 0.93), and by comparison to inter-subject correlations and the independent component analysis. Our results suggest that SFS functions as a natural extension to ALFF, and can therefore serve as a method capable of identifying brain areas activated in response to naturalistic tasks.

Introduction

Functional MRI experiments have historically used contrast-based designs. Experimental and control (baseline) conditions either alternate during longer-duration (~16-20s) "blocks," or present a baseline condition sporadically interspersed by experimental shorter-duration (~0.025-1s) "events." To localize task-activated brain responses, the most commonly-employed statistical method has been the General Linear Model (GLM) (Friston et al., 1995). In the GLM framework, voxel-wise fMRI time-series are modeled by fitting the experimental design matrix or regressor(s) of interest. The matrix defines the timing of each condition, which is then modeled via convolution of delta functions representing each onset with their expected hemodynamic responses. Hemodynamic amplitudes for each condition are then averaged across multiple trials and statistically compared across conditions (1st level analysis) and subjects (2nd level analysis). Thus, for any GLM analysis, the accuracy of obtained neurobiological results depends critically on the accuracy of the design matrix.

But what if the design matrix/regressor(s) are unknown or ill defined? While conventional block and event-related designs can achieve high experimental precision, and task-free "resting-state" studies have greatly expanded our knowledge of baseline brain functionality, their significant limitation is dependence upon experimental environments that lack the complex interactive dynamics encountered in the world outside the scanner. To counter this issue, there has been an increase in the use of naturalistic stimuli, such as movies (Bartels and Zeki, 2005; Carlson et al., 2016; Hasson et al., 2009; Hasson et al., 2004; Iidaka, 2016; Nummenmaa et al., 2012; Oren et al., 2016; Wang et al., 2017) and subject-initiated navigation within virtual reality environments (Calhoun et al., 2002; Guderian et al., 2015; Kaplan et al., 2014; Spiers and Maguire, 2006). In addition, while pharmacological studies of novel compounds provide a known time of bolus-injection, the subject-specific neurobiological pharmacokinetics that would normally be used to define regressors of interest are *a priori* unknown. Under these circumstances, analyses of neuroimaging data require a sliding-window measure of activation whose dynamics themselves *define*—rather than depend upon—the time-course of subject-specific "stimuli."

With burgeoning interest in resting-state, new analytic approaches were designed to be "stimulus blind" (Spiers and Maguire, 2007). The most common one uses *within-brain cross-correlations*, across region or voxel time-series, as a measure of functional "connectivity." A

second approach uses *across-brain cross-correlations*, to define areas most uniformly activated across subjects ("inter-subject correlation," ISC). The third approach, *independent components analysis* (ICA), minimizes mutual information to define areas of disparate activation. A fourth approach defines activation by the *amplitude of spontaneous fluctuations*, filtering for the low frequencies associated with resting-state networks (ALFF; the f/ALFF variant aims to correct for physiological noise by taking the ratio of amplitude over low frequencies over the amplitude of all frequencies (Yang et al., 2007; Zou et al., 2008)). Finally, a fifth approach uses *scale-free behavior* observed in brain signals to define activation as a function of shifts in relative time-series frequencies across the brain ("power spectrum scale invariance," PSSI (Radulescu et al., 2012; Tolkunov et al., 2010)). While each of these has strengths, collectively they also have important limitations to consider in the analyses of naturalistic, as opposed to resting-state, designs.

In a study using a free viewing of a long uninterrupted movie segment, ISCs were introduced to show that individual brains "tick together" when viewing the same complex dynamic scenes, revealing synchronization extending beyond the primary visual and auditory cortices and far exceeding the synchronization found during darkness (eyes-closed rest) (Hasson et al., 2004). The same group later found that these complex visual stimuli evoke highly reliable (within and between-subject) and functionally selective responses in many brain areas (Hasson et al., 2010). Multiple recent studies employing continuous stimuli have pointed to functional significance of ISC patterns by demonstrating their association with various subjective and objective measures of presented contents. For example, ISCs have been shown to correlate with subjects' ratings of pleasantness and arousal during viewing of movies depicting unpleasant, neutral and pleasant emotions (Nummenmaa et al., 2012), humor during comedy-watching (Iidaka, 2016), pleasantness and arousal elicited by music as well as the energy-related features in the music during attentive listening to classical music (Trost et al., 2015), stereoscopic depth and strength of the viewing experience when watching same movies in 3D versus 2D (Gaebler et al., 2014), and the degree of attentional load during a task that employed movies as the encoded stimuli and manipulated attentional load via a secondary task that was performed simultaneously with encoding (Oren et al., 2016). Individuals with clinical conditions, such as Down's Syndrome (Anderson et al., 2013), autism (Hasson et al., 2009; Salmi et al., 2013), and melancholic depression (Guo et al., 2015), show diagnostic population-consistent responses during natural movie viewing that are different from responses commonly observed within typical controls. Finally, one recent study found age-

related decreased synchrony during movie watching, associated with cognitive measures sensitive to attentional control (Campbell et al., 2015). Despite the above described functional, and potentially clinical, relevance of ISCs when applied to tasks that are time-locked across sessions and subjects, this method cannot be applied when there are subject or session-specific differences in the way the task is performed, such as when a subject is interacting with an environment at his or her own pace. In addition, while the ISCs may suggest potential processes underlying activation changes, higher ISCs need not mean higher activation: regions that are highly synchronized across individuals may be simultaneously deactivated.

Another commonly employed data-driven method is the Independent Component Analysis (ICA), which allows identification of signals of interest as well as signals of no interest by treating the fMRI signal as a linear mixture of unknown source signals (Calhoun et al., 2001). While both temporal and spatial ICA of fMRI data are possible, spatial ICA is usually preferred due to the higher plausibility of the underlying neurophysiological model and lower computational requirements (Cong et al., 2014). ICA identifies maximally spatially independent components (brain networks) without requiring any prior information about the task, making it, in theory, suitable for extracting components engaged by both task-free and naturalistic task paradigms. However, thus far, ICA has been applied primarily to resting state and block and event-related designs and rarely in naturalistic tasks (Cong et al., 2014). In resting state, it has been used to uncover robust temporally coherent fluctuations: *resting state networks*, such as the primary sensorimotor network, the visual network, a network consisting of bilateral temporal/insular and anterior cingulate cortex regions, left and right fronto-parietal networks and the Default Mode Network (van den Heuvel and Hulshoff Pol, 2010). However, these same networks (sometimes called *intrinsic networks*) have been found to be engaged during various cognitive tasks, and while they may be (spatially or temporally) modulated by the task, there is a considerable similarity in the networks identified during rest and during a task (Calhoun et al., 2008; Calhoun and Pearlson, 2012). Furthermore, when applied to naturalistic tasks (Cong et al., 2014; Malinen et al., 2007; Ylipaavalniemi et al., 2009), time-courses of the stimuli features are usually correlated to time-courses of identified spatial components, hence assuming significant prior knowledge of the task structure.

Finally, while the two frequency-based analyses: ALFF and PSSI, operationally depend upon neither known design matrix/regressors nor coherence between individuals, in fact they are

both strongly affected by the frequency characteristics of stimuli. In the case of ALFF, the reliance on a specific frequency band is optimized for resting-state networks, without a way to define other, more appropriate, frequency bands for naturalistic tasks. The advantage of PSSI is that it does not require defining a preferred frequency band. Yet, the complex frequency characteristics of naturalistic stimuli run the risk of affecting PSSI in ways that complicate interpretation of results. For this reason, PSSI often does better with block than event-related designs, as the former includes a simple preferred frequency, which can then be filtered out.

Our group recently introduced a new measure, *signal fluctuation sensitivity* (SFS), designed to dissociate functionally relevant signal dynamics from scanner-induced nuisance fluctuations (DeDora et al., 2016). Originally conceived to provide objective metrics by which to optimize fMRI acquisition parameters, we showed that SFS correlated with dynamic fidelity to known time-series produced with a dynamic phantom, and also with enhanced sensitivity to both local and long-range functional connectivity within the brain's Default Mode Network (DMN) in human resting-state scans, as well as with increased accuracy of PSSI values (DeDora et al., 2016). Although not its intended purpose, we realized early on that the method might also be applied to identify neural activity in task-free/naturalistic paradigms, since the ability to dissociate signal fluctuations from noise fluctuations may be fruitful when the aim is to map the strength and location of task-free brain responses, as well as their connectivity.

To test this hypothesis, we employed the following strategy. We compared voxel-wise SFS values from fMRI time-series obtained during a naturalistic task to those from pure resting state in same subjects without requiring *a priori* information regarding the task structure. For proof of concept, we did so in three separate datasets employing unstructured task designs of different levels of complexity, with known/expected functional neuroanatomical results from task-based experiments with similar context that could justify hypothesized activation. The first two tasks were movies, in which all subjects would experience the same stimuli; the last task was an interactive neuroeconomic game that was self-driven, and therefore varied for each subject in terms of timing. Of the two movies, the first was visual-only and non-emotional (nature scenes from a documentary); *we therefore expected activation of visual networks*. The second was both visual and auditory and had a dynamic arc of emotional engagement (a television drama), which we later had the same subjects rate for arousal and valence; *we therefore expected that activation of visual, auditory, and emotion networks would track self-reported emotional arousal/valence.*

The third task, in which subjects engage in serial economic exchanges, *we expected to activate the learning and reward networks*. For the two movies, presented stimuli were temporally consistent across subjects, which permitted additional validation of SFS using the ISC method. For all three tasks, we also performed ICA, to compare how that method's results related to findings with SFS results.

Methods

Overview

We compared voxel-wise SFS values from fMRI time-series obtained during a naturalistic task to those from pure resting state in three tasks of different levels of complexity: two movie-like tasks and an interactive neuroeconomic game. Each of the three datasets consisted of a resting-state session (eyes open with a white fixation cross displayed on a black background) as well as an additional task session (within-subject design). The tasks analyzed here included presentation of a short silent nature documentary movie showing wild animals in their natural habitat (MOVIE, Study 1), presentation of an emotionally-engaging pilot episode of the television drama series *Lost* (LOST, Study 2), and an iterative version of the Trust Game (TRUST, Study 3). MOVIE and LOST tasks were intended to provide complex/realistic design-free stimuli that standardize content across subjects (unlike the pure resting state) while being visually and emotionally engaging. For these two tasks, we compared the areas with increases in SFS values (relative to resting state) to areas displaying high levels of synchronization across subjects identified using inter-subject correlations. For the LOST task, a sliding-window approach was implemented and increases in SFS across windows were correlated with subjects' ratings of emotional content. We then extended the analysis to a third task where stimuli were not time-locked across participants and where ISCs could not be applied: an interactive neuroeconomic game. For each of the three tasks, we additionally performed ICA to identify components significantly modulated by task.

Data sets analyzed here were collected on two different MRI scanners: a Siemens Magnetom 7 Tesla scanner (Martinos Center for Biomedical Imaging at Massachusetts General Hospital (MGH)) and a Siemens Magnetom Trio 3 Tesla scanner (Social, Cognitive, and Affective Neuroscience (SCAN) Center at Stony Brook University), and utilized three independent groups of subjects.

Participants and Task Descriptions

Study 1 (MOVIE). Seventeen healthy adult subjects (N = 17, 6M/11F) participated in the study (mean age = 30.81 ± 13.6). All subjects underwent six minutes of eyes-open resting-state fMRI, immediately followed by six minutes of movie watching during which they were shown a continuous compilation of scenes from BBC's nature documentary TV-series "Planet Earth" showing wild animals in their natural habitat. The movie was stripped of all sound effects.

Study 2 (LOST). Eighty-two adult female subjects (N = 82) participated in this study (mean age = 22.94 ± 6.51). Participants included patients with generalized anxiety disorder (GAD, N = 22), major depressive disorder (MDD, N = 18), those comorbid for anxiety and depression (CO, N = 22) and healthy controls (HC, N = 20). Diagnoses of GAD, MDD, or comorbidity were confirmed via the Structured Clinical Interview for DSM-IV (Axis I Disorders—Patient Edition, Version 2) by trained clinical psychologists at Stony Brook University. All participants were free from psychotropic medications for at least six months prior to the time of the scan. The healthy control group had no diagnosable lifetime Axis I disorder and no history of neurological illness. Subjects underwent five minutes of eyes-open resting-state fMRI, immediately followed by an uninterrupted scanning session lasting 42 minutes during which they watched the entire pilot episode of ABC's drama TV-series *Lost*. Subjects whose data have been analyzed here represent a subset of individuals with minimal motion (< 3mm/deg. absolute translation/rotation) from a larger sample of subjects (N = 94). To minimize potential confounding effects of subject motion and allow inclusion of as many subjects' data as possible, here we only analyzed the first 20 minutes of *Lost*-viewing data. Immediately after watching the episode in the scanner, participants re-watched it outside of the scanner and rated its content on a nine-point scale in terms of valence ("How pleasant do you feel?", from 1 = negative to 9 = positive) and arousal ("How excited do you feel?", from 1 = low arousal to 9 high arousal). The episode was split into two hundred 10-15 second clips and ratings were obtained for each clip. For more details, see (Carlson et al., 2016).

Study 3 (TRUST). Sixteen healthy adult male subjects (N = 16, mean age 25 ± 3.61) participated in a study aimed at examining effects of the neuropeptide oxytocin on iterative social learning and trust. Each subject was scanned under placebo (PL) and oxytocin (OT) on two separate days (to allow for drug wash-off). During each of the two scanning sessions, subjects first participated in a neuroeconomic task ("Iterative Trust Game") lasting ten minutes, followed by a

ten-minute eyes-open resting-state scan. The task was an iterative version of the classic Trust Game (Berg et al., 1995), adapted from the two-player version used by (King-Casas et al., 2005). During each scan, the subject ("Investor") played 20 rounds with the same (fictional) opponent ("Trustee"). At the start of each round, the subject is given 20 monetary units (MU) and told to invest any amount between 0 and 20 into the Trustee. This invested amount is then tripled. The Trustee then repays some portion of the total (0 - 60 MU) back to the Investor. While the 'Trustee' is a computer-generated algorithm, subjects were told they were playing against a human and the deception was revealed only following completion of the study. To increase engagement, subjects were compensated for their participation in the amount proportional to the MUs they earned during the two games.

During resting state (all three studies) subjects were instructed to remain still, to keep their eyes open focusing on a fixation cross on the screen, and to let their minds wander without allowing themselves to rest upon any particular topic. The Institutional Review Boards of the institutions where subjects were scanned (Stony Brook University, Massachusetts General Hospital) approved all studies. All subjects provided written informed consent.

fMRI Acquisition Parameters and Data Preprocessing

Study 1 (MOVIE) and Study 3 (TRUST). Acquisition parameters (and data preprocessing) used for these two studies were identical and previously described (DeDora et al., 2016) as those optimized to preserve fMRI time-series dynamic fidelity. A Siemens Magnetom 7 Tesla scanner with a 32-channel head-coil (Martinos Center for Biomedical Imaging, MGH) was used to acquire 748 T2*-weighted EPI volumes per session with the following parameters: SMS acceleration factor = 5, GRAPPA acceleration = 2, TR = 802 ms, TE = 20 ms, flip angle = 33°, 2 x 2 x 1.5 mm voxel size, 85 slices, and interleaved slice acquisition. For Study 1, one resting-state and one movie session were acquired per subject. For Study 3, two resting state sessions and two Trust game sessions were acquired (on two different days) for each subject. Conventional B0 field map images derived from phase differences between gradient echo images at TE = 4.60 and 5.62ms were also acquired (TR = 723 ms, flip angle = 36°, voxel size = 1.7 x 1.7 x 1.5 mm, 89 slices) and used during preprocessing to correct for distortions in EPI images caused by magnetic field inhomogeneity. Whole-brain T1-weighted structural volumes were acquired using a conventional multi-echo MPRAGE (MEMPRAGE) sequence with 1 mm isotropic voxel size and four echoes

with the following parameters: TE1/TE2/TE3/TE4 = 1.61/3.47/5.33/7.19 ms, TR = 2530 ms, flip angle = 7°, slice gap = 0.5 mm, GRAPPA acceleration = 2.

Standard preprocessing procedures including realignment, coregistration and normalization of the structural image, normalization to 2 × 2 × 2 mm MNI space, and smoothing with a 6-mm full width at half-maximum Gaussian kernel were performed in SPM12 (http://www.fil.ion.ucl.ac.uk/spm/). Fieldmap correction was performed using *epidewarp.fsl* (https://surfer.nmr.mgh.harvard.edu/fswiki/epidewarp.fsl), following the realignment procedure in SPM. Coregistered structural images were segmented into probabilistic maps of gray matter, white matter, and CSF. Initial ten volumes of each functional scan were discarded prior to any further analyses.

Study 2 (LOST). A Siemens Magnetom Trio Tim 3 Tesla scanner equipped with a 12-channel head-coil (SCAN Center, Stony Brook University) was used to acquire 1333 T2*-weighted EPI volumes with the following parameters: TR = 2100 ms, TE = 23 ms, flip angle = 83°, 2.33 × 2.33 × 3.50 mm voxel size, 37 slices, and interleaved slice acquisition. Initial 143 volumes were acquired during pure resting-state. Standard whole-brain T1-weighted structural images were acquired using a conventional MPRAGE sequence with the following parameters: TR = 1900 ms, TE = 2.53 ms, flip angle = 9°, and voxel size = 1 × 0.98 × 0.98 mm.

Standard preprocessing procedures including slice-time correction, realignment, coregistration to a structural image, normalization to 2 × 2 × 2 mm MNI space, and smoothing with a 6-mm full width at half-maximum Gaussian kernel were performed in SPM8. Coregistered structural images were segmented into probabilistic maps of gray matter, white matter, and the cerebrospinal fluid (CSF). Initial five time points of resting-state scans were removed from all analyses to allow for steady-state imaging to be reached. In addition, the first nine volumes immediately following resting-state were removed since only the word “LOST” was shown on the screen during that time. Arousal and valence ratings data were resampled to TRs to match the length of the show, and a 3 second lag was added to account for the delay in the hemodynamic response. As previously reported (Carlson et al., 2016), ratings were averaged across subjects to eliminate noise from single subject ratings and provide a more robust measure of emotional content.

Computation of SFS, Sliding-Window SFS, and Statistical Analyses on SFS Maps

We used MATLAB 2016a to compute voxel-wise SFS from SPM-preprocessed fMRI time-series according to the following equation:

$$SFS_{vox} = \frac{\mu_{vox}}{\mu_{global}} \times \frac{\sigma_{vox}}{\sigma_{CSF}}$$

As previously described (DeDora et al., 2016), in the first term the mean signal of the voxel of interest (μ_{vox}) is scaled by the mean signal of the entire brain (μ_{global}) and in the second term the standard deviation of the time-series obtained from the voxel of interest (σ_{vox}) is scaled by the average standard deviation of all time-series of voxels in the cerebrospinal fluid (σ_{CSF}). Mean global signal was computed from all voxels included in the conjunction of gray matter, white matter, and cerebrospinal fluid maps. Voxel-wise time-series were detrended prior to computation of standard deviations. Standard deviations of the CSF voxels (nuisance fluctuations) were computed using an eroded probabilistic map of CSF (subject-specific segmented map of CSF thresholded at 70%) to ensure minimal contributions from other tissues which may contain relevant signal fluctuations. To avoid distorting time-series dynamics by averaging them, standard deviations were computed voxel-wise for each voxel in the CSF and then averaged across all voxels in the region.

Study 1 (MOVIE). We computed whole-brain voxel-wise SFS maps for each 10-minute fMRI session, resulting in two SFS maps per subject. SFS values for the two tasks (SFS_{MOVIE} vs. SFS_{REST}) were statistically compared using a paired-t test in SPM12. Mean absolute translation and mean absolute rotation were used as covariates of no interest, to account for possible differences in motion between the two sessions.

Study 2 (LOST). Due to much longer time-series acquired during LOST compared to resting state, we used a sliding-window approach: time-series were split into thirty-two overlapping windows (moving forward by 14 time-points ≈ half a minute) of equal length, each window thus exactly matching the duration of the resting-state time-series (138 time-points ≈ 5 minutes). We then computed thirty-two SFS maps for LOST to be compared with the SFS map for REST for each subject. For each window, a mixed-effects ANOVA was implemented in SPM12 with "group" (GAD, MDD, CO, and HC) as a between-subject factor and "task" (LOST or REST) as a within-subject factor. Motion parameters (mean absolute translation and mean absolute rotation during each task) were entered as confounding covariates to control for possible

differences in motion between the two tasks. Statistical contrasts were set up to look at main effects of task (SFS_{LOST} vs. SFS_{REST}) as well as to test for differences between groups and a possible interaction between task and group. Average arousal and valence ratings were down-sampled to the same time resolution by computing the average arousal and valence of each time-window. At this temporal resolution, average arousal ratings were essentially the inverse of average valence ratings (Pearson's r = -0.99).

Study 3 (TRUST). Due to the within-subject/crossover design of the study, four SFS maps were obtained per subject ($SFS^{PL}{}_{TRUST}$, $SFS^{PL}{}_{REST}$, $SFS^{OT}{}_{TRUST}$, $SFS^{OT}{}_{REST}$), corresponding to each 10-minute fMRI session. Repeated measures ANOVA was implemented in SPM12 with "drug" (PL or OT) and "task" (TRUST or REST) as factors and mean absolute translation and rotation as covariates of no interest. While we were primarily interested in main effects of task, we also performed statistical tests for the effects of drug and drug-task interactions.

Inter-Subject Correlations

As an alternate measure of activation to (MOVIE and LOST) tasks, we computed inter-subject correlations (ISC) (Hasson et al., 2004). Inter-subject correlations identify regions showing synchronized activity across subjects throughout the task. We obtained voxel-wise ISC maps by computing pairwise correlations between subjects' time-series for each voxel. Prior to computations of all (between-subjects) pairwise correlations, we performed voxel-wise time-series detrending, regression of six motion parameters from SPM's realignment step, regression of mean white matter and CSF signals, and high-pass filtering (at 0.01 Hz). Correlations were Fisher z-transformed and averaged across subjects to obtain task-specific ISC maps.

Independent Component Analysis

To identify functionally connected networks in a data-driven manner, we also performed group spatial ICA (Calhoun et al., 2001) using Group ICA/IVA of fMRI Toolbox (GIFT v 4.0a, http://mialab.mrn.org/software/gift/). For each dataset, the number of independent components (ICs) was estimated from the data using all of the subjects' data and the minimum description length (MDL) criteria (Li et al., 2007). We used ICASSO to analyze ten runs of the ICA to ensure component stability (Himberg et al., 2004). After canonical principal component analysis (PCA)

preprocessing (variance normalization), subject-specific PCA was first performed, followed by temporal concatenation and group-level PCA and noise-free ICA. Finally, subject-specific spatial maps and associated time courses were estimated using back-reconstruction (GICA) (Erhardt et al., 2011). We used the Infomax algorithm for ICA. Spatial maps were converted to Z values.

For all three studies, we first performed ICA on each task and rest session separately to see if there were any task-specific components that did not appear in resting state. This was achieved by computing spatial cross correlations/spatially sorting average resting-state components based on average task components (Calhoun et al., 2008). Finally, we performed ICA on task and resting-state sessions, of equal duration, within the same study, together. Artefactual components were manually determined and discarded. For each non-artefactual component, the resulting session-specific spatial maps were compared using paired t-tests (Study 1) or repeated measures ANOVAs (Study 2 and 3) in SPM12, after masking for voxels surviving one-sample t-test on ICA Z-scores. For Study 2, ICA was first performed using 20 minutes of LOST data, artefactual components were manually identified and discarded, and the remaining components were temporally sorted using average arousal ratings as a reference function, to identify task-relevant components. In addition, to compare the two tasks directly, we performed ICA on five minutes of LOST data (here we picked the time-window (#5) corresponding to the peak in arousal ratings and hence hypothesized to correspond to greatest deviation from resting state) and five minutes of REST data.

Results

SFS Identifies Task-Related Activations

In each of the complex task contexts described above, SFS identified significant activation consistent with the expected neurobiology.

Study 1 (MOVIE). For the MOVIE task, SFS identified activations in brain areas commonly associated with processing of visual stimuli. Paired-t test on SFS maps revealed significant activations during MOVIE primarily in the visual cortex: *bilateral calcarine/cuneus*, the *lingual gyrus*, *inferior/middle occipital* and *middle temporal* regions. During REST, we identified increases in SFS in the *bilateral precuneus* and in the *right postcentral gyrus* (**Figure 4-1A**). For a detailed list of activated regions, see **Table 4-1A**.

Study 2 (LOST). For the LOST task, in addition to visual regions identified for MOVIE, SFS analysis pointed to activations in the auditory network and in frontal regions associated with cognitive processing of decision-making as related to emotional stimuli. Mixed-effects ANOVA revealed significantly higher SFS values during LOST relative to REST primarily in visual and auditory networks - *calcarine/lingual gyrus/cuneus* and *superior and medial temporal and occipital* regions, an effect that was highly consistent across the thirty-two windows. On the other hand, SFS values were consistently significantly lower during LOST compared to REST in the main Default Mode Network (DMN) hub – *precuneus/posterior cingulate cortex (PCC),* and somewhat less consistently in other DMN regions – *medial prefrontal cortex* and *left* and *right parietal cortices,* as well as in the *supplementary motor area* (**Figure 4-2A**). For a detailed list of regions showing significant differences in SFS during one of the time-windows (window #5 - corresponding to the peak in arousal rating), see **Table 4-1B**.

When comparing the entire 20 minutes of LOST to (5 minutes) REST, in addition to these differences, we found a significant difference in the *bilateral superior frontal/orbitofrontal cortex (OFC)* ($SFS_{LOST} > SFS_{REST,}$ peak at MNI (18, 62, -4)). In fact, examining each 5-minute window individually (**Figure 4-2B**) bilateral OFC activation identified by SFS correlated extraordinarily tightly with arousal ratings: with Pearson's r = 0.93, $p = 4.9 \times 10^{-15}$ (**Figure 4-2C**). For other regions identified via the whole time-series analyses (and also consistently showing increased SFS across the five-minute windows), we found significant *negative* correlations of increases in SFS to arousal (*positive* correlations to valence) in *right inferior/middle occipital/temporal gyrus* (MNI (50, -70, 8), $r = -0.35$, $p = 0.05$), *left inferior/middle occipital/temporal gyrus* (MNI (-46, -72, 2), $r = -0.74$, $p = 1.3 \times 10^{-6}$), *right superior/middle temporal gyrus* (MNI (58, -22, -2), $r = -0.50$, $p = 0.003$), *left superior/middle temporal gyrus* (MNI (-58, -42, 6), $r = -0.51$, $p = 0.003$)), and in the *right fusiform* (MNI (42, -50, -22), $r = -0.74$, $p = 1.2 \times 10^{-6}$). We did not find any significant differences between the four subject groups or any interactions between task and group for any of the time-windows.

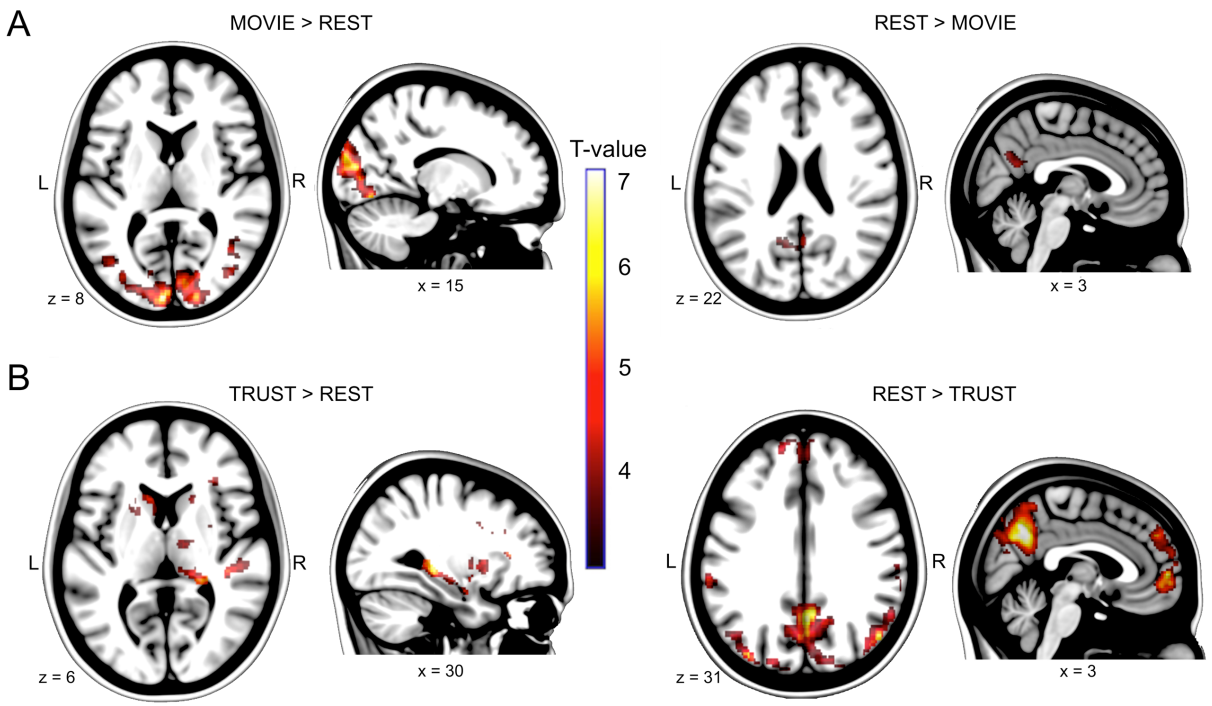

Figure 4-1: SFS identifies regions active during MOVIE and TRUST. (A) Visual regions including cuneus and inferior occipital regions have higher SFS values during MOVIE compared to REST (left). On the other hand, precuneus is less active during MOVIE compared to REST (right). **(B)** TRUST vs. REST comparison revealed areas associated with memory (hippocampus) and reward processing/reinforcement learning (caudate and putamen) as having significantly higher SFS values during TRUST (left). Default Mode Network regions (posterior cingulate, medial prefrontal cortex, and bilateral parietal cortices) showed higher SFS values during REST (right).

A)	MOVIE > REST				
	Peak MNI	*Location Description (AAL Atlas (Brodmann Area))*	*Cluster Extent*	*Cluster-level* $p_{FWE\text{-}corr}$	*Peak-level T-value*
1	[-6, -96, 8]	Bilateral Calcarine/Cuneus (BA 17/18)	1168	0	6.84
2	[-22, -70, -2]	L Lingual Gyrus (BA 19)	102	0.002	6.64
3	[-36, -82, 14]	L Mid. Occipital (BA 19)	194	6.4×10^{-6}	6.03
4	[42, -62, 12]	R Mid. Temporal (BA 37)	127	3.5×10^{-4}	5.26
		REST > MOVIE			
1	[-6, -56, 12]	Bilateral Precuneus (BA 23)	194	0.009	4.84
2	[50, -20, 54]	R Postcentral Gyrus (BA 3)	246	0.002	4.49
B)		LOST* > REST			
1	[-62, -20, 2]	L Middle/Superior Temporal Gyrus (BA 22/21)	3414	0	10.12
2	[50, -70, 10]	R Occipital/Mid. Temporal (BA 37/19/39)	1278	3.53×10^{-14}	9.33
3	[60, -22, 0]	R Middle/Superior Temporal Gyrus (BA 22/21)	1964	0	9.11
4	[-6, -84, -4]	Calcarine/Lingual Gyrus (BA 17)	418	2.79×10^{-6}	5.73
5	[42, -48, -22]	R Fusiform (BA 37)	190	2.30×10^{-3}	5.65
6	[16, 58, -14]	*R Frontal Med. Orbital (BA 11/10)*	381	7.47×10^{-6}	5.19
7	[-22, -8, 62]	L Superior Frontal Gyrus (BA 6)	98	0.071	4.86
8	[-30, -58, -8]	L Fusiform (BA 37)	143	0.012	4.70
9	[-14, 60, -6]	*L Frontal Med. Orbital (BA 11)*	138	0.015	4.57
10	[32, -48, 62]	R Superior Parietal (BA 2)	225	7.23×10^{-4}	4.47
11	[-12, -56, 74]	L Precuneus (BA 5)	165	5.50×10^{-3}	4.29
		REST > LOST*			
1	[6, -54, 24]	Bilateral Precuneus/PCC/Cuneus (BA 23/17/18)	5823	0	9.33
2	[-38, -74, 42]	L Angular Gyrus (BA 7/39)	1059	2.08×10^{-12}	6.76
3	[42, -60, 42]	R Angular Gyrus/Inferior Parietal (BA 39/40)	1835	0	5.62
4	[60, -50, -10]	R Middle/Inferior Temporal Gyrus	175	3.90×10^{-3}	5.56
5	[0, 50, -4]	Frontal Med. Orbital/Frontal Sup. Medial/ACC (BA 10/32)	863	1.02×10^{-10}	5.48
6	[-30, 18, 56]	L Mid. Frontal (BA 8)	451	1.19×10^{-6}	5.45
7	[0, 0, 64]	Supplementary Motor Area (BA 6)	1053	2.34×10^{-12}	5.40
8	[46, 16, 38]	R Inferior Frontal Operculum (BA 44)	568	6.70×10^{-8}	4.87
9	[54, 14, -6]	R Rolandic Operculum (BA 48)	201	1.60×10^{-3}	4.75

Table 4-1: List of regions showing significantly different SFS values during task relative to rest for MOVIE and LOST tasks. Location descriptions are based on the AAL atlas. *For LOST, shown are significant activations for a single five-minute window (#5).; $p < 0.05$, 3dClustSim-corrected (alpha = 0.05).

Study 3 (TRUST). For the TRUST task, SFS identified activations is regions commonly associated with memory and reward processing and in the primary motor network. We found significant effects of the TRUST task in the bilateral *hippocampus*, *caudate* and *putamen*, as well

as in the left *precentral gyrus*, right *middle frontal gyrus*, and the right *thalamus*. Regions identified as more active during REST compared to TRUST included bilateral *precuneus, middle occipital/angular gyrus (parietal cortices), medial prefrontal cortex*, *superior frontal gyrus,* and *middle temporal* regions (**Table 4-2** and **Figure 4-1B**). We found no significant differences between the placebo and oxytocin conditions and no interaction between drug and task (all neuroimaging statics are reported at $p < 0.05$, 3DClustSim-corrected).

	Peak MNI	*Location Description (AAL Atlas (Brodmann Area))*	*Cluster Extent*	*Cluster-level* $p_{FWE\text{-}corr}$	*Peak-level T-value*
TRUST > REST					
1	[28, -32, -2]	R Hippocampus (BA 37/27)	571	1.09×10^{-9}	6.32
2	[-34, -24, 52]	L Precentral/Postcentral (BA 4/3)	294	1.85×10^{-5}	5.38
3	[36, 10, 28]	R Inferior Frontal Operculum (BA 44/48)	189	3.67×10^{-4}	5.23
4	[48, -38, 18]	R Superior Temporal Gyrus (BA 41/48)	281	1.07×10^{-5}	5.11
5	[32, 30, 10]	R Insula (BA 48)	62	0.154	5.05
6	[-24, 16, 2]	L Putamen	83	0.049	5.01
7	[-8, 8, 12]	L Caudate	93	0.029	4.91
8	[32, 4, -2]	R Putamen (BA 48)	97	0.024	4.73
9	[10, -12, 4]	R Thalamus	99	0.022	4.56
10	[-36, -12, -14]	L Hippocampus (BA 20)	63	0.146	4.49
11	[20, 18, 2]	R Caudate	92	0.031	4.27
REST > TRUST					
1	[4, -60, 36]	Bilateral Precuneus	2724	0	7.66
2	[48, -72, 32]	R Angular Gyrus/Supramarginal (BA 39/BA 40)	1158	4.44×10^{-16}	6.70
3	[2, 56, 2]	Frontal Med. Orbital/Frontal Sup. Medial (BA 10)	1004	1.58×10^{-14}	6.45
4	[-36, -82, 30]	L Med. Occipital/L Angular Gyrus (BA 19/39)	336	1.56×10^{-6}	5.89
5	[-60, -26, 38]	L Supramarginal Gyrus (BA 40/2)	188	3.82×10^{-4}	5.07
6	[22, 60, 10]	R Superior Frontal Gyrus (BA 10)	84	0.047	4.68
7	[-54, -66, 10]	L Mid. Temporal Gyrus (BA 37)	117	0.009	4.60
8	[58, -62, 6]	R Mid. Temporal Gyrus (BA 37)	91	0.033	4.57
9	[-22, 50, 18]	L Mid. Frontal (BA 46)	71	0.094	4.26

Table 4-2: List of regions showing significantly different SFS values during task relative to rest for the TRUST task. Location descriptions are based on the AAL atlas. $p < 0.05$, 3dClustSim-corrected (alpha = 0.05).

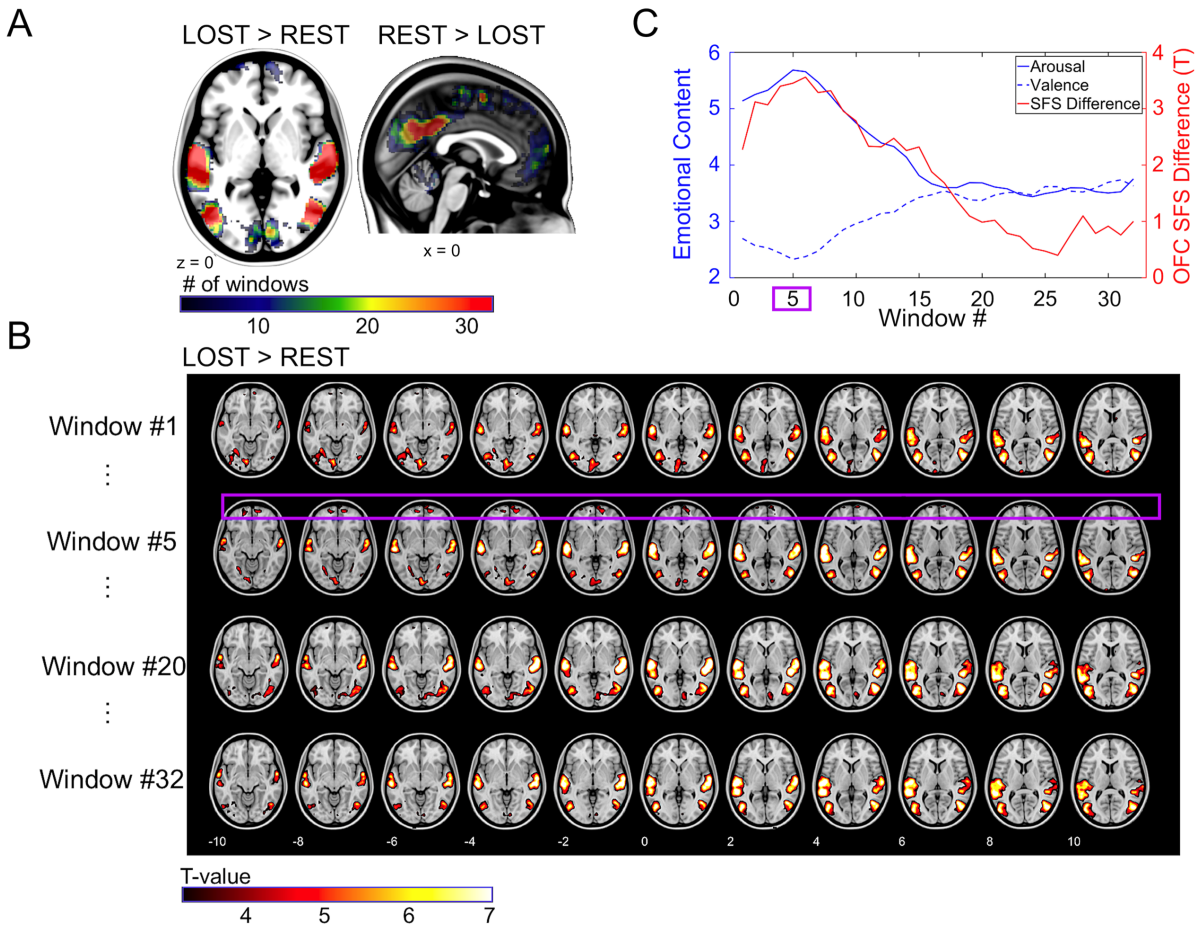

Figure 4-2: SFS identifies regions active during LOST. (A) Regions identified using SFS are consistent across different five-minute time-windows. Calcarine/lingual gyrus/cuneus and superior and medial temporal and occipital regions are active during LOST. On the other hand, posterior cingulate gyrus/precuneus, and somewhat less consistently supplementary motor area, medial prefrontal cortex, and bilateral parietal cortices are deactivated during LOST. **(B)** Bilateral orbitofrontal cortex (OFC) is active during some windows (peak activation during window #5, highlighted in purple), but not during others. **(C)** LOST – REST difference in SFS values in the OFC (red) is highly positively correlated with average arousal ratings (blue, Pearson's r = 0.93). At this temporal resolution, average valence ratings are almost perfectly negatively correlated with average arousal ratings (dashed blue, Pearson's r = –0.99).

Brain Areas Identified via ISC Analyses Match Those Found via SFS Analyses

To further validate the SFS-identified activations, we computed ISC maps for the two tasks utilizing temporally locked stimuli across subjects (MOVIE and LOST), and thresholded them to show regions co-activated across subjects at correlation levels beyond those expected by chance ($p < 0.05$, Bonferroni-corrected). For the MOVIE task, this resulted in identification of visual areas: *calcarine/lingual gyrus/cuneus* (Brodmann areas (BA) 17/18, peak at MNI (12, -89, 29)). For LOST, in addition to these primary visual regions (peak at MNI (10, -80, -4)), *bilateral medial*

temporal/occipital regions (BA 37, L/R peaks at MNI (-48, -75, 5) and (49, -69, 6) and *bilateral superior temporal* regions (BA 21/22, L/R peaks at MNI (-62, -19, 4) and (64, -11, -1)) showed high degree of synchronization across subjects (**Figure 4-3**), consistent with regions identified via the SFS analyses (**Figure 4-1A** and **Figure 4-2**).

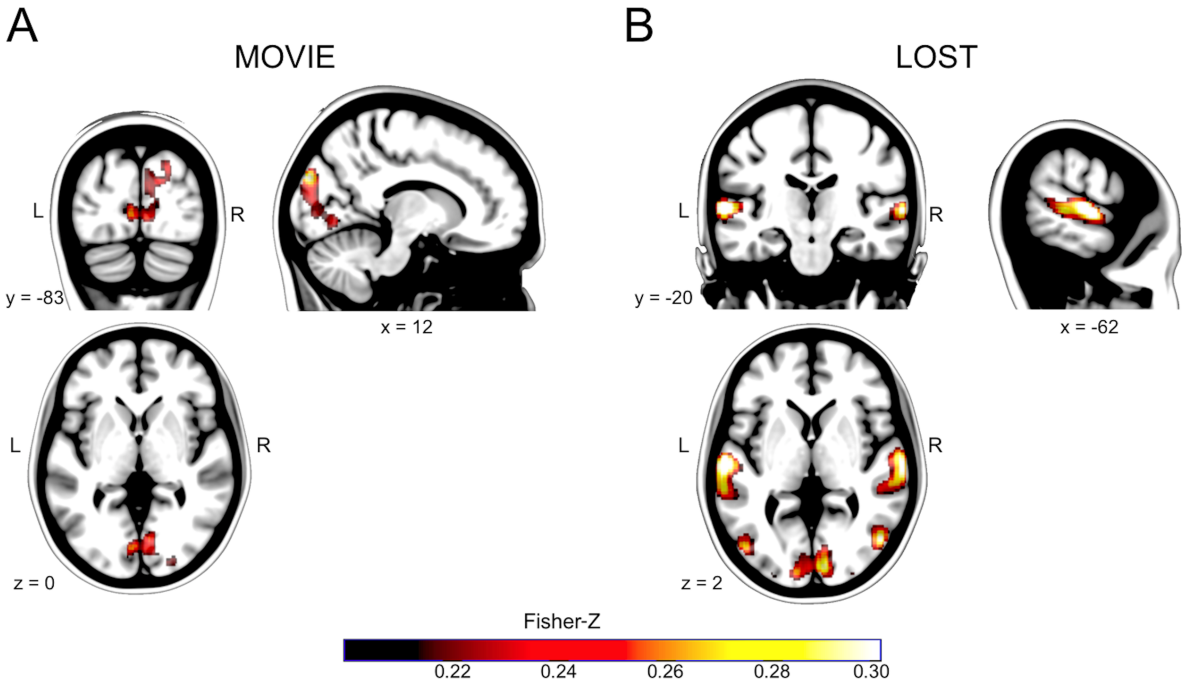

Figure 4-3: Intersubject correlations (ISCs) identify regions co-activated across subjects during MOVIE and LOST. While during the MOVIE task **(A)** (silent scenes from "Planet Earth" nature documentary) only the primary visual cortex shows highly synchronized activity across subjects (N = 17, 7T fMRI), a more engaging LOST task **(B)** (first half of the pilot episode of TV drama series Lost) with more complex visual and auditory stimuli additionally induces synchronized activity (N = 82, 3T fMRI) in bilateral medial and superior temporal regions - areas involved in complex visual functions and language and sound processing (Brodmann areas 37 and 21/22). These results are consistent with SFS findings (**Figure 4-1A** and **Figure 4-2**).

ICA Points to Increased Engagement of Visual Networks During Movie-Watching, but no Individual IC Time-Courses Track the Emotional Contents of LOST

Study 1 (MOVIE): ICA identified 40 spatially independent components, ten of which were manually labeled as noise because they were primarily containing edges and/or ventricles (after confirming, based on separate ICAs, that there were no entirely new components recruited during MOVIE vs. REST; spatial correlation r ranging from 0.21 to 0.89, median $r = 0.60$). The remaining components' spatial maps for the two sessions were compared using paired t-tests in SPM12. We

found increased recruitment of visual networks during MOVIE, while there were no statistically significant differences in the auditory network (**Figure 4-4A**), consistent with the SFS findings**.**

Study 2 (LOST): Independent component analysis in GIFT identified 31 independent components (ICs) for LOST task (20 minutes), eight of which were manually labeled as containing obvious artifacts (e.g., containing primarily edges or ventricles). ICA identified multiple components corresponding to commonly found resting-state networks (for example those described in (Roseman et al., 2014; Smith et al., 2009)), such as visual network (separate components containing medial, lateral, and occipital portions), auditory network, frontal executive control network, left and right fronto-parietal networks, default mode network, and sensorimotor network. To identify most task-relevant components, we sorted the mean group components temporally using correlation criteria with average arousal rating as a reference time-course. Component time-courses showed only weak correlations with arousal ratings, with a component containing *medial visual* regions identified as the most task-relevant (r = 0.19), followed by components encompassing bilateral *postcentral* (r = -0.19) and bilateral *superior frontal* regions (r = 0.19).

To compare the two tasks, we also performed ICA on time-window #5 of LOST task on its own. We picked the time-window corresponding to the peak in arousal ratings, where we expected to see the strongest differences relative to resting state. We identified 22 ICs, and for each non-artefactual component (17 of them) found the most spatially correlated component from REST (where 21 ICs were identified, six of which were artifact-driven). It was possible to establish correspondence (significant spatial correlation; r ranging from 0.20 to 0.78, median r = 0.55) between spatial maps of ICs from REST and LOST, suggesting that LOST task did not necessarily recruit an entirely distinct network of regions, but rather (potentially) modified the existing resting-state networks. To directly compare the tasks, we performed a single ICA with REST and LOST time-window #5 entered as two sessions for each subject. This resulted in identification of 21 components, five of which were manually identified as containing non-neural noise. A t-test for main effects of task, within a mixed-effects ANOVA design in SPM 12, on spatial maps of each of the remaining 16 components, identified significant differences in visual and auditory networks ($p < 0.05$ 3dClustSim-corrected), pointing to greater recruitment of these regions during LOST (**Figure 4-4B**). There was a significant spatial correspondence between visual and auditory

networks identified for the two datasets shown in **Figure 4-4** (r = 0.42 for Visual #1, r = 0.66 for Visual #2, and r = 0.54 for the auditory network).

Study 3 (TRUST): ICA on all 64 sessions (N = 16, 2 tasks × 2 drugs) identified 39 spatially independent components (after separate ICAs on TRUST and REST showed spatial correspondence between the identified components; spatial correlation r ranging from 0.22 to 0.89, median r = 0.69). Twelve of these components were manually labeled as containing non-neural noise (edges, ventricles, etc.). For each of the remaining 27 components, we performed a repeated-measures ANOVA on spatial maps, with three factors: "subject," "drug" (PL, OT) and "task" (TRUST, REST). Only one component showed significantly increased engagement during task - a component containing bilateral *precentral* areas (BA 4/ BA 3/ primary *motor cortex*), while the *precuneus/PCC* network and right *lingual gyrus/fusiform* areas showed increased engagement during REST. No interaction between drug and task was found for any of the components.

Discussion

We found that signal fluctuation sensitivity reliably identifies task-relevant activations in complex task designs which closely mimic realistic environments: for the MOVIE task this involved identification of primary and secondary visual areas, for the LOST task, in addition to those, we also found significant activations in the auditory cortex and the frontal/orbitofrontal regions (with near-perfect tracking of the dynamic emotional content of the stimuli), while the TRUST game engaged brain's reward and learning circuits. In all three tasks, the Default Mode Network regions showed increased SFS values under resting state.

For the MOVIE task (**Figure 4-1A**), identification of the primary and secondary visual cortex (BA 17/18), but not auditory and frontal areas, is consistent with the task being stripped of sound effects and being less structured and less emotionally engaging relative to the episode of TV drama *Lost* - while the LOST task depicts an exciting emotional story of a plane crash and its survivors, the MOVIE task simply consists of short non-emotional silent clips showing different wild animals in nature. The less pronounced differences in DMN (statistically significant only in its most prominent hub – the PCC) for the rest vs. task contrast could also be potentially explained by the lack of clear structure in this task.

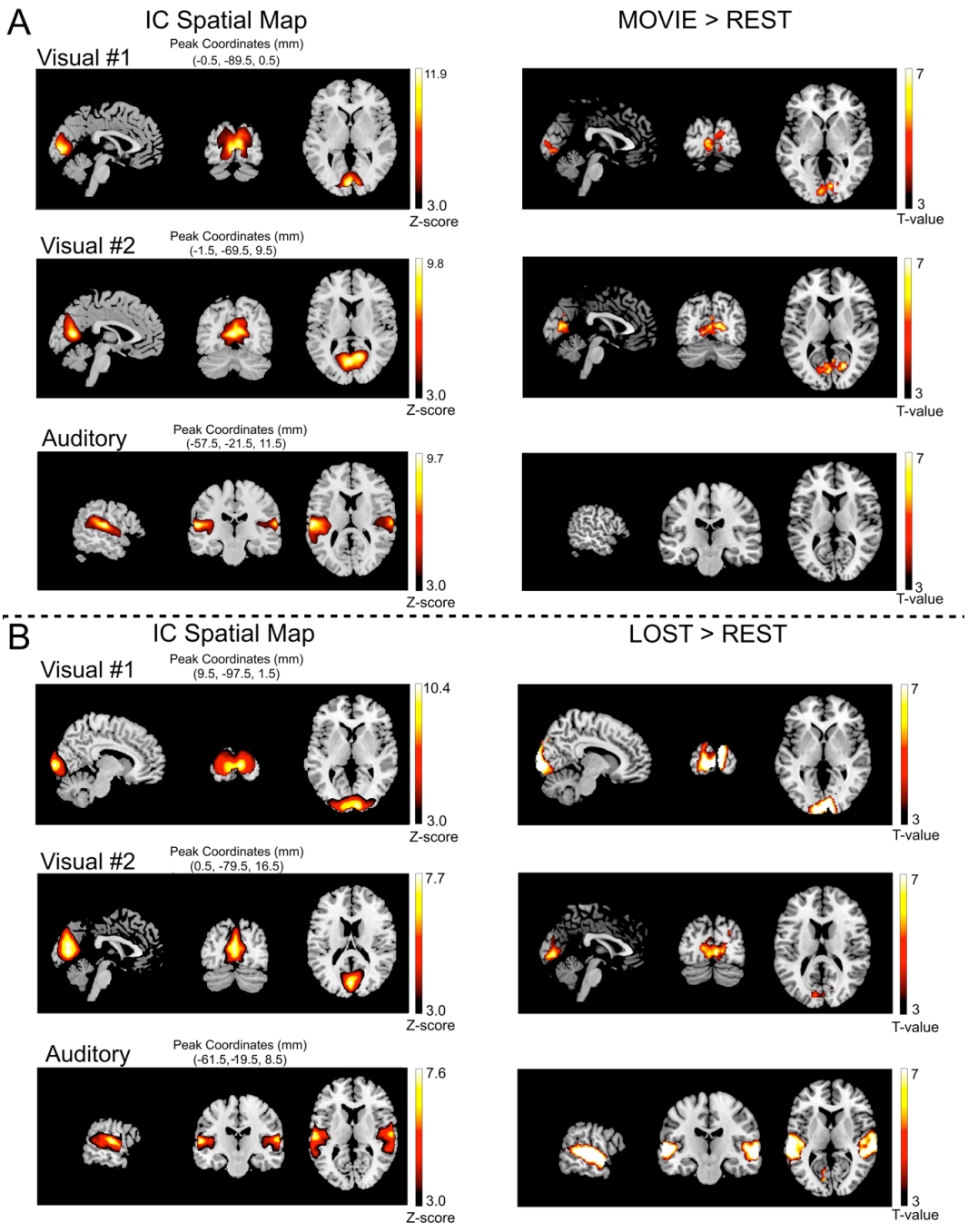

Figure 4-4: ICA and follow-up statistical tests on spatial maps of identified components show significant modification of resting-state networks by task. (A) There is a significantly increased recruitment of visual and auditory networks during LOST and **(B)** a significantly increased recruitment of visual, but not auditory networks during MOVIE.

For the LOST task (**Figure 4-2**), comparisons to resting state across thirty-two windows consistently revealed robust increases in SFS values in the primary visual cortex (Brodmann area (BA) 17), associative visual cortex/bilateral inferior occipital gyrus (BA 19 and 37), and the areas involved in processing of complex sounds - middle temporal gyrus (BA 21) and superior temporal gyrus (BA 22). On the other hand, Default Mode Network (DMN) regions (posterior cingulate cortex (PCC), medial prefrontal cortex (MPFC), and left and right parietal cortices) showed higher SFS during resting state. These findings agree with the nature of the task(s). For instance, Brodmann area 37 (bilateral inferior occipital gyrus) is involved in complex visual functions, such as face recognition (Blonder et al., 2004), structural judgment of familiar objects (Kellenbach et al., 2005), visual motion processing (Beer et al., 2002) and some memory circuitries when visual information is involved (Slotnick and Schacter, 2004), while Brodmann areas 21 and 22 (middle and superior temporal regions) are involved in complex language processing, processing of complex sounds (Mirz et al., 1999), as well as perception of emotions in facial stimuli (Dricu and Fruhholz, 2016). DMN is known to be engaged in initiating processes that support emotional processing (ventral MPFC), self-referential judgments (dorsal MPFC), and the recollection of prior experiences (posterior parts of DMN), and is thought to represent a highly active (resting-state) functional baseline that gets modified by certain tasks (Raichle, 2015).

Furthermore, the increase in SFS values during LOST was associated with changes in the emotional content of the episode, as reflected in the arousal (and valence) ratings, confirming that SFS is identifying regions active in response to the task. Specifically, activation in the bilateral superior frontal/orbitofrontal cortex (OFC, BA 10/11) was strongly associated with arousal ratings (**Figure 4-2C**). The orbitofrontal cortex has been implicated in sensory integration and in learning, prediction and decision-making especially as related to reward and emotional stimuli (Bechara et al., 2000; Kringelbach, 2005).

ISC maps may be used as an alternative to GLM to find brain regions active during a naturalistic task design. They are appropriate when brain responses due to the task can be assumed to be time-locked across sessions and subjects (the sequence of events in the task is the same every time it is performed), as is the case when watching a movie. ISC analyses for MOVIE and LOST tasks confirmed SFS findings – with visual (both tasks) and auditory areas (LOST task only) showing highest degree of synchronization across subjects (**Figure 4-3**). ISCs rely on capturing

the same temporal dynamics across many subjects and are therefore not applicable in cases when there is randomization, for example in a realistic game-task (such as TRUST) or during resting state. On the other hand, SFS, which relies on difference in dynamics between the task and resting state session of an individual subject, can be applied even when there is randomization, with group results depending on how similar the *overall* response to the task is across subjects. We therefore used the ISCs on movie-like tasks to validate the findings from SFS analyses, and then extended the SFS analyses to an interactive task for which ISCs are not applicable.

In this task (TRUST) (**Figure 4-1B**), SFS identified significant activations due to the interactive game in the bilateral *hippocampus, caudate, putamen,* left *precentral gyrus*, right *middle frontal gyrus*, and the right *thalamus*. Hippocampus has a well-established role in memory processing and learning, of immediate relevance in an iterative game where trust must be learned by encoding memories of recent interactions. Thalamus is a critical hub for relay of sensory information and the peaks of thalamic activation identified here belong to the sub-regions of thalamus having high probability of anatomical connections to the prefrontal cortex (Thalamic Connectivity Atlas), which is where activation peaks for the executive and memory tasks commonly fall (Johansen-Berg et al., 2005). A recent meta-analysis of multi-round investment games, aimed at identifying neural signatures of trust in reciprocity (Bellucci et al., 2017), found that trust decisions consistently activated ventral striatum (likely associated with reward processing during trust decisions) and dorsal striatum (likely related to social reinforcement learning). Regions identified as more active during resting state were again consistent with the Default Mode Network.

In agreement with the existing literature (Calhoun et al., 2008), our tasks did not engage entirely new task-relevant components, as seen from significant spatial correlations between resting-state and task networks. Follow-up statistical tests on spatial maps of identified ICs showed that MOVIE and LOST tasks required greater recruitment of visual and auditory networks (LOST only) (**Figure 4-4**), consistent with both SFS and ISC findings. However, no components' time-courses reflected the emotional content of LOST well (low time-course correlations with the average arousal ratings) and the only statistically significant spatial modification of identified brain networks due to TRUST task was in the left precentral gyrus (primary motor network, also identified via the SFS analysis). On the other hand, as presented above, differences in SFS in the bilateral *orbitofrontal cortex* (relative to resting-state) tightly tracked the evolving emotional

content of the episode, and increases due to TRUST were consistent with the existing literature on similar tasks, involving memory and reward-processing regions.

Despite being a powerful advanced data-driven method requiring little prior knowledge about the task, ICA does not generalize naturally to group analyses (resulting in many different approaches (Erhardt et al., 2011)) and its success may eventually depend on the researcher's ability to correctly classify the resulting components into signals of interest and signals of no interest, and into meaningful functional networks (such as visual, auditory, etc.), or on the ability to decompose the task into specific events whose features can then be correlated with the extracted components' time-courses. In fact, while the interpretation of independent components is not straightforward, ICA can be thought of as being a natural measure of functional connectivity (rather than activity) since component regions have similar temporal response. We were primarily interested in *localizing* functional *activity* due to task, and hence assessing how the components are modulated by the task spatially. Further analyses exploring the strengths of connections between different ICs under different conditions could reveal differences due to task (or drug) beyond simple spatial modifications of those networks.

We have demonstrated that SFS may be used as a quick data-driven approach to identify brain areas activated in response to continuous series of complex dynamic naturalistic stimuli. When it comes to complex naturalistic experiences, SFS may be a good alternative to existing methods, with the advantage of being assumptions-free (both in terms of the shape of the hemodynamic response function and the structure of the design matrix) compared to GLM, being applicable to tasks with a certain level of randomness compared to ISCs, and being a simpler measure of activation (rather than connectivity) that is easily generalizable to group analyses compared to ICA. Finally, while SFS looks at overall activity due to a complicated realistic task, other analyses methods, such as reverse correlation and multi-voxel pattern analysis (MVPA) may be appropriate when one is interested in decomposing neural activity due to specific events from the complex environment of which they may be a part (Spiers and Maguire, 2007).

Chapter 5 Modeling Dynamic State of Mind: Cybersecurity Study

Introduction

Nonlinear complexity analyses describe system-wide dynamics and perform well as a diagnostic tool since they provide information about the location of dysregulation. However, they do not explain the system structure, and are unable to provide models that predict future trajectories of the system. Development of tools that would do so would finally open doors to a new category of questions about the brain (beyond "where" and "how much"), while bridging the gap to single-subject clinical applications. The first step towards addressing this problem will be integration of high quality fMRI data with computational modeling, to provide a bridge between the dynamics of functional brain networks and the dynamics of human behavior.

Here, we make first steps towards creating single-subject models capable of predicting subjects' evolving behavior/state of mind from fMRI data. We combine machine learning methods with high fidelity fMRI data to show that subjects' dynamically changing state of mind may be inferred from time-courses of relevant functional brain networks in a very complex task design. We analyze fMRI data and associated behavioral outcomes from N = 26 healthy adult subjects who played four sessions of an engaging pattern detection game, the cybersecurity enterprises (CSE) task, while being scanned in a 7T MRI. In the context of a dynamic self-paced game where subjects are expected to identify correct pattern while being faced with ambiguous feedback, we employ three qualitatively distinct models to predict subjects' state of mind (*confident* = knowing the pattern versus *confused* = guessing/learning). The first model is the gold standard which uses probabilities assigned by an optimal Bayesian solver to predict subject's state of mind (behavior only). The second model uses only the brain data (fMRI time-series of networks identified via independent component analysis), while the third combines both behavioral and brain data. These models are compared against two baseline/control models where only class proportions of the training data are considered and random guesses are made on the testing data according to those class proportions. We find that brain fMRI time-series derived from only three relevant networks may be used to predict subjects' state of mind (*confident* versus *confused*) throughout the game,

and that they do so at levels beyond those expected by chance, in out-of-sample testing data, and at an individual-subject level.

Methods

Task Description

When studied in a controlled environment, decision-making often involves manipulated, deterministic variables. However, in the real world (including intelligence analysis), most decisions are made in conditions of uncertainty, where feedback may be ambiguous and unreliable. The Cybersecurity Enterprises (CSE) game task was designed to simulate a real cybersecurity monitoring system, where analysists are asked to identify patterns (indicating threat) in low signal-to-noise environments containing both relevant and irrelevant information. The task requires participants to select correct suspicious target (row) from a list of three communications, based on patterns with respect to their properties (**Figure 5-1**). The suspicious target must contain a unique feature (i.e., a feature that is not contained in any other row). To probe decision-making in conditions of uncertainty, after each selection (*trial*), subjects are given ambiguous feedback (*score*) between 0 and 100 indicating the probability of having selected the correct choice. Probabilistic feedback is sampled from two distributions depending on whether the answer is correct. We assume five ambiguity levels (from 1 to 5), and for each one of them we associate a triangular probability distribution with different level of overlap between the two distributions. The overlaps are 0, 0.11, 0.17, 0.22, and 0.27 for ambiguity levels 1-5, respectively. After several consecutive correct responses are made (3-5, pseudo-randomized, to avoid predictability), it is assumed the subject has identified the signature of the attack (*pattern*) and the pattern changes without warning. A complete *round* is defined as the entire sequence of trials before the change in pattern. The objective is to find as many patterns as possible within a set amount of time (10 minutes). To avoid performance outliers, a "hint" system is implemented, and is activated whenever the participant takes more than 60 seconds to identify the correct signature, with a box and an arrow appearing to indicate the property with the correct answer (a column to focus on).

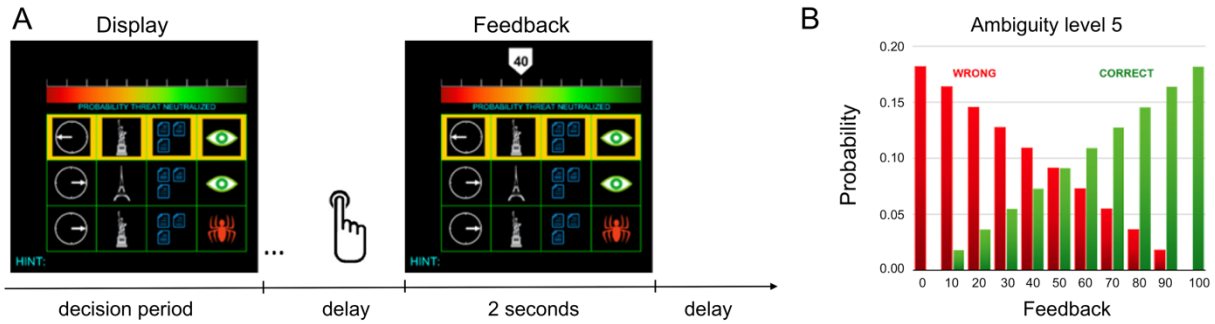

Figure 5-1: Cybersecurity Enterprises Task (**A**). Display with three choices is shown to the subject. Each communication (row) has four properties: *Time, Location*, *File Size*, and *Intrusion Type* (3 possible values per property). The pattern signature must be a unique feature (i.e., a feature not contained by any other row). After selection, and a random delay of 0.5 to 2 seconds, feedback between 0 and 100 appears indicating the probability of threat level. This feedback is presented for 2 seconds, followed by a crosshair that lasts for 0.5 to 2 seconds, before moving to the next trial. **(B)**. Probability distributions associated with the feedback generated for ambiguity level 5 (five different distributions were used, level 5 represents the highest ambiguity). For instance, if the selected answer is correct, there is a probability of 0.18 of receiving a feedback of 100. The overlap between these two distributions is 0.27, representing the percentage of false positives and false negatives.

Participants

Twenty-six healthy adult subjects (13M/13F, mean age = 26.7 ± 5.5) underwent 7T functional MRI while playing four 10-minute sessions of the CSE game. For standardization and to focus primarily on the pattern detection process, rather than the learning component, only participants with strong pattern detection skills were recruited to participate. This was achieved by screening subjects using an online version of the CSE task, followed by on-site training on the actual task. Subjects were screened using a deterministic online version of the task with accurate (unambiguous) feedback provided after each trial and required to achieve an average accuracy higher than 65% and average pattern identification time lower than 40 seconds to participate in the actual probabilistic version of the task in the MRI scanner. Recruited subjects were then extensively trained on the probabilistic version of the game. A research team member thoroughly explained the ambiguous feedback found in the game that the subject would be playing in the scanner. A short 3-minute version of the game was played by the study team member in front of the subject to demonstrate the probabilistic feedback mechanism. The subject was then familiarized and trained on his/her own 3-minute session. The subject replayed this session until he/she was confident with playing. Lastly, a 1-minute variant was played within the MRI scanner to ensure that the subject was trained with the MRI button box game controller. Finally, during the fMRI scan, subjects played four 10-minute sessions of the game, with short breaks between the

sessions, during which a research study member would make sure they were doing OK and remind them to stay still.

MRI Data Acquisition Parameters and Preprocessing

Scanning was performed using a 7T Siemens Magnetom MRI scanner with a 32-channel head-coil (Martinos Center for Biomedical Imaging, Massachusetts General Hospital). Each fMRI scan included four 10-minute task sessions (748 volumes). In addition to BOLD fMRI data, we acquired Field Map images (used to correct distortions in EPI BOLD data) and T1-weighted structural (MEMPRAGE) images (coregistered with functional images and used in segmentation and normalization procedures). Whole brain EPI BOLD data were acquired using parameters described in Chapter 3 as those optimized for dynamic fidelity (Acquisition C, row 9, **Table 3-1**). Field Map images were acquired using the following parameters: TR = 723ms, TE 1 = 4.60ms, TE 2 = 5.62ms, flip angle = 36°, voxel size = 1.7 × 1.7 × 1.5 mm, 89 slices. The whole-brain T1-weighted structural volumes were acquired using a conventional multi-echo MPRAGE (MEMPRAGE) sequence with 1 mm isotropic voxel size and four echoes with the following protocol parameters: TE1 = 1.61ms, TE2 = 3.47ms, TE3 = 5.33ms, TE4 = 7.19ms, TR = 2530ms, flip angle = 7°, with R = 2 acceleration in the primary phase encoding direction (32 reference lines) and online GRAPPA image reconstruction. Standard SPM12 preprocessing included realignment, coregistration and normalization of the structural image, normalization to 2 × 2 × 2 mm MNI space, and smoothing with a 6-mm full width at half-maximum Gaussian kernel. Fieldmap correction was performed using *epidewarp.fsl*, following the realignment procedure in SPM. Coregistered structural images were segmented into probabilistic maps of gray matter, white matter, and CSF. Initial ten volumes of each functional scan (session) were discarded prior to any further analyses.

Independent Component Analysis

We performed spatial independent component analysis (ICA) using Group ICA/IVA of fMRI Toolbox (GIFT v 4.0a) (N = 26, four sessions per subject) to identify functionally connected networks in an entirely data-driven manner. We used ICASSO to analyze ten runs of the ICA to confirm component stability. After canonical PCA preprocessing (variance normalization), subject-specific PCA was first performed, followed by temporal concatenation and group-level

PCA and noise-free ICA. Finally, subject-specific spatial maps and associated time courses were estimated using back-reconstruction (GICA). We used the Infomax algorithm for ICA. Number of independent components was estimated using all the subjects' data (N = 26, four 10-minute sessions per subject) and the minimum description length (MDL) criteria. ICA identified 35 components, 8 of which were manually selected as containing non-neural noise (CSF or motion-related artifacts/edges of the brain). For detailed descriptions of the remaining 27 components see **Table 5-1** below.

IC	Description
1	Bilateral Frontal Sup Medial (BA 8), R IFG/Frontal Mid./Precentral (BA 9/44), Superior Temporal Pole (BA 38)
2	R Calcarine/R Cuneus (BA 17/18) – Visual Occipital Network
3	Bilateral Paracentral/Postcentral Lobule (BA 4) – Primary Motor Cortex
4	Bilateral Calcarine/ L Cuneus (BA 17/18) – Visual Network (L > R)
5	R Postcentral (BA 3/2/4) – Primary Somatosensory Cortex (Touch)
6	Bilateral Lingual Gyrus/Calcarine (BA 17) – Visual Medial Network
7	L Postcentral (BA 3/2/4), Supplementary Motor Area (BA 6) – Primary Somatosensory Network (Touch)
8	Bilateral Postcentral (BA 4/3, 43, 48) – Motor/Gustatory Cortex
9	**Bilateral Occipital Mid/Lingual Gyrus (BA 18/19) – Visual Lateral Network**
10	L Parietal Inf./Angular Gyrus (BA 39/40), L Precentral (BA 9), L IFG (BA 46), R Parietal Inf. – L Frontoparietal Network
11	**Bilateral Precuneus (BA 7), Occipital Med/Superior, R Mid Frontal (BA 6) – Visuospatial Attention Network (R > L)**
12	Bilateral Frontal Sup Medial/ACC (BA 10/32), PCC/MCC (BA 23), L Angular Gyrus (BA 39) – closest match to DMN
13	Bilateral Precuneus, PCC, MCC (BA 23/7)
14	Bilateral Parietal Inf. (BA 2/40), IFG (48/45/44)
15	Bilateral Precuneus (BA 7)
16	Occipital Sup/Mid (BA 19) – Visual Network
17	**L Precuneus/Parietal Inf./Occipital Mid (BA 7/40/19), L Precentral/IFG (BA 6/44/48) – Visuospatial Attention Network (L > R)**
18	Bilateral Occipital Mid/Angular Gyrus (BA 39/19/7), Precuneus (BA 7/23)
19	R Parietal Inf. (BA 39/40/7), R Frontal Mid/Sup (BA 10), R Frontal Mid (BA 8) – R Frontoparietal Network ~ mirror image of IC 10
20	Bilateral Insula (BA 47/48), ACC/Sup Frontal (BA 34/32) – Anterior Salience Network
21	Bilateral Frontal Mid./Sup., Supplementary Motor, Precuneus (BA 9/10/46; 7, 24)
22	R Insula/Temporal (BA 42, 22, 48)
23	Bilateral Rolandic Operculum/Insula (R > L, BA 48), Supplementary Motor Area (BA 6)
24	Bilateral Temporal Mid./Supramarginal (BA 22), Precuneus
25	Bilateral Temporal Pole
26	Supplementary Motor Area, Bilateral Precentral (BA 6) – Motor Network
27	L Supplementary Motor Area (BA 6), L IFG (BA 45. 48. 44), L Temporal Mid. (BA 22)

Table 5-1: Description of components identified via ICA of CSE task. Regions were labeled via references to AAL and Brodmann atlases, after thresholding of mean component maps (averaged over all subjects and sessions) at Z = 3. Abbreviations: R = right, L = left, BA = Brodmann Area, IFG = Inferior Frontal Gyrus, ACC = Anterior Cingulate Cortex, PCC = Posterior Cingulate Cortex, MCC = Medial Cingulate Cortex, DMN = Default Mode Network. Bold font components (9, 11, and 17) are the ones identified as most relevant to prediction of state of mind via univariate feature selection.

Bayesian Solver – Optimal Strategy using Bayes' Rule

The optimal strategy of playing the game when ambiguity is present in the feedback is the one that follows a Bayesian approach:

1. At the start of a round, the player determines the set of unique items on screen and assigns a uniform prior to the probability of each of unique items being the signature of attack;
2. Player selects the communication that is the most likely to contain the signature element (at first trial, player picks the communication with highest number of unique items present since the prior is uniform; after that the choice depends on the exact probability that an item is the signature);
3. An ambiguous feedback between 0 and 100 is provided to player as described above;
4. Based on i) the feedback provided, ii) knowledge of the full probability density function of feedback conditioned on the ambiguity level of the round and the correctness of player's selection (P (*feedback* | *ambiguity*, *correctness*)) and iii) the prior previously calculated/assumed, the player makes a calculation of the posterior probability of the selection made being correct. Here we employ an application of the Bayes' theorem to incorporate the newly acquired knowledge of the feedback into the solver's estimate:

$$P_{post.}(correct|feed.) = \\ = \frac{P(feed.|correct) * P_{prior}(correct)}{P(feed.|correct) * P_{prior}(correct) + P(feed.|incorrect) * (1 - P_{prior}(correct))}$$

5. Based on the posterior probability of accuracy of selection made, solver then updates his belief about each of the unique items being the signature by multiplicative rescaling of the previous estimate, using maximum a posteriori criteria;
6. Player prunes the set of unique items he/she keeps track of based on the set of unique items in newly displayed communications and rescales the probabilities of each of them being the signature;
7. Player repeats steps 2 - 6 until the number of successive attacks identified correctly reaches a pre-specified integer (number of correct selections needed to identify the signature).

This implementation of game-theoretically "optimal" *Bayesian solver* works on the exact "screen"/visual that human subjects were given and attempts to solve the game in parallel to humans as if looking over the shoulder. This "on-line" solving of the exact game that humans are playing is intended to reveal what stage the subject's solving might be at. In attempting to solve the game, the solver produces and keeps track of probabilities of each choice containing the sought-after signature. We can then extract a quantity we refer to as *Bayesian Conviction* defined as the maximum of posterior probabilities that each of the three communications contains the signature:

$$Bayesian\ Conviction = \max\left(P_{post.}(signature\ in\ row\ i) : i \in \{1, 2, 3\}\right)$$

This is the probability based on which the solver makes selection and indicates its level of conviction about what the exact signature of the current round is. We make use of this solver-produced level of "conviction" to predict the state of mind (*confident* vs. *confused*) that human subjects are in (described in detail below).

Predictive Modeling of Subjects' Behavior

From the subject's (state of mind) perspective, the game can be split into two qualitatively distinct parts: trials during which the subject is confident about the signature of the attack (and is selecting correct rows consecutively in a streak) and the trials during which he/she is either picking an incorrect row or switching between the correct and incorrect decisions repeatedly. From here onward, we referrer to these states of mind as the subject being *confident* or the subject being *confused*, respectively. All consecutive trials that are a part of the streak leading to a change in pattern are therefore considered as examples of the *confident* state, and all other trials as examples of the *confused* state (could be due to subject's guessing or learning the pattern by process of elimination). Our goal is to be able to predict whether the subject is in a *confident* or a *confused* state of mind from the relevant brain data at each trial (or time point), rather than to predict simply whether they picked the correct row (accuracy) since in that case positive examples would invariably be contaminated by random guesses and would not necessarily reflect that the subject has detected the pattern. **Figure 5-2** below demonstrates how state of mind, as defined here, may

differ from subject's accuracy at each trial, for two representative subjects.

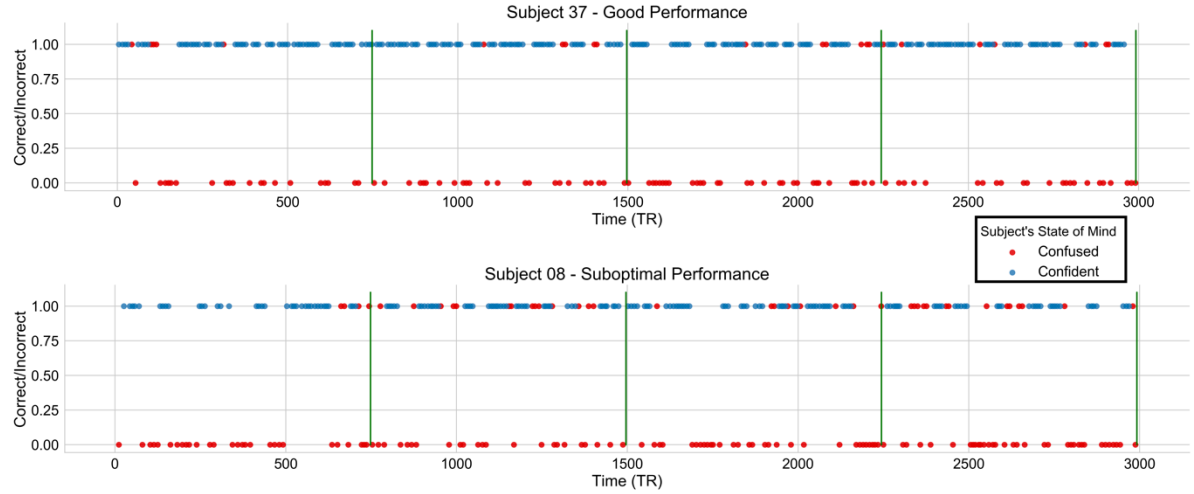

Figure 5-2: Accuracy at each trial for representative subjects with good and suboptimal performance, color-coded by their state of mind. Vertical green lines represent ends of each of the four (10-minute) sessions. Subject 37 (top) had average accuracy of 0.72 while subject 08 (bottom) had average accuracy of 0.63, across trials in all four sessions. All trials in which the subject made an incorrect choice are labeled as *confused* trials, while as some of the correct choice trials may be labeled as *confused* as well, due to them not being a part of the streak leading to a change in pattern.

Figure 5-3 below shows how Bayesian Conviction varies over time for a representative good performer and representative suboptimal performer (based on the average accuracy during the four sessions relative to the rest of the subjects), as a function of their state of mind.

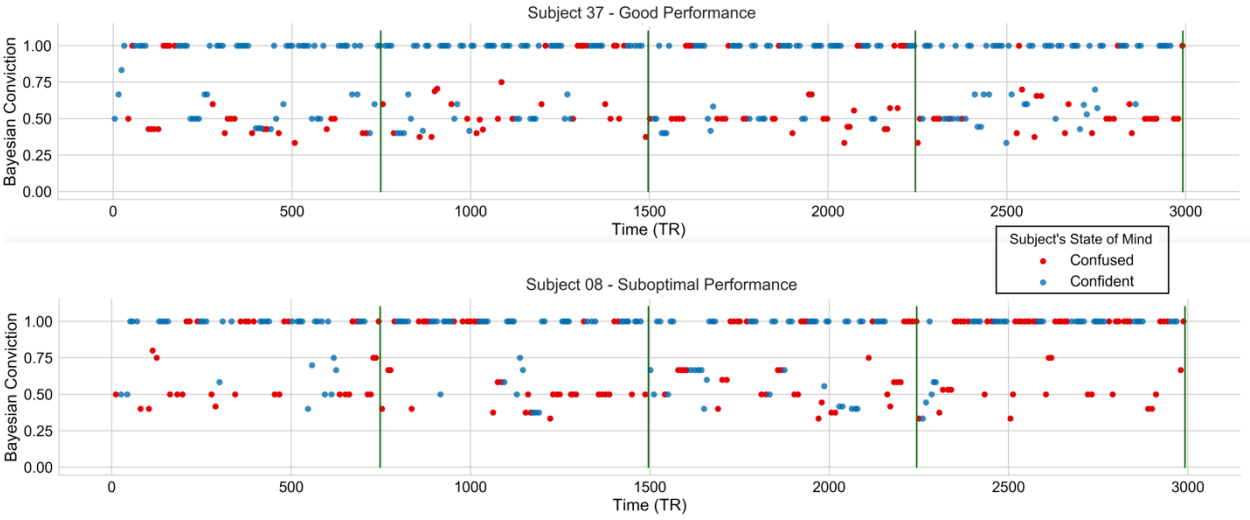

Figure 5-3: Bayesian Conviction for representative subjects with good and suboptimal performance, color-coded by their state of mind. Vertical green lines represent ends of each of the four (10-minute) sessions. Subject 37 (top) had average accuracy of 0.72 while subject 08 (bottom) had average accuracy of 0.63, across trials in all four sessions.

We expect that subjects who are good at detecting the pattern play in a close to Bayesian manner, and that Bayesian Conviction at each trial should be a good (in fact, *as good as theoretically possible*) predictor of the subjects' state-of-mind. In fact, as shown in **Figure 5-4** below, subjects with higher average accuracy made choices closer to those of the Bayesian solver (mean distance of the subject's pick from the Bayesian solver's pick in terms of the probability assigned by the Bayesian solver and the average accuracy of the subject's pick across 26 × 4 sessions were correlated highly positively with Pearson's $r = 0.73$, $p < 10^{-17}$; additionally, the standard deviation of the distance from the Bayesian Conviction and the average accuracy of the subject's pick across 26 × 4 sessions were correlated negatively with Pearson's $r = -0.67$, $p < 10^{-14}$). That is, sessions in which choices made by the subject were consistently closer to those made by the Bayesian solver, were the sessions where subjects achieved higher average accuracy. Furthermore, there were no cases where a subject played far from Bayesian solver while still achieving high accuracy.

We employ the following strategy to show that fMRI data may be used to predict subject's state of mind at an individual level at a higher than by chance accuracy. We start with a simple machine learning algorithm – logistic regression – and compare the following models:

1. Model 1 (behavior only): a single feature – Bayesian Conviction (BC) – is used to classify subject's state of mind as *confident* vs. *confused* – this is what we believe to be the gold standard (regardless of the machine learning algorithm used).
2. Model 2 (brain only): mean time-series extracted from relevant brain regions/networks are used as features to predict *confident* versus *confused* (e.g., time-courses (TCs) from the 27 Independent Components' listed in **Table 5-1**) – if fMRI data are informative of subject's state of mind, we expect this model to perform better than control/baseline models (4 and 5, below), but not as well as the gold standard (model 1).

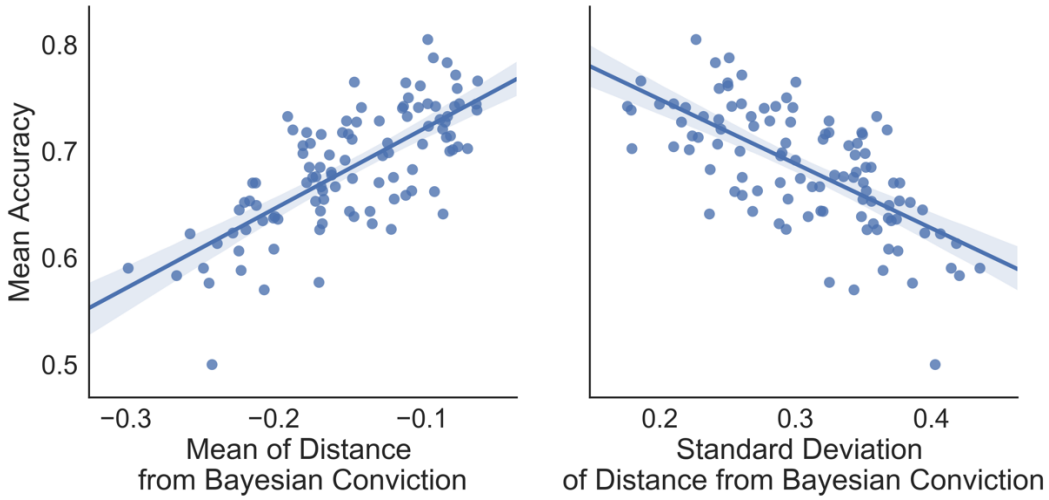

Figure 5-4: Subjects who make choices closer to those of the Bayesian solver perform better. Distance from Bayesian Conviction is defined as the difference between the probability assigned by the Bayesian solver to the row that was chosen by the subject and the Bayesian Conviction (i.e., the maximum posterior probability of the three rows at that trial). Each point represents an average across a session. Mean accuracy is defined as the number of correct choices divided by the total number of trials in a session. Left: Pearson's $r = 0.73$, $p < 10^{-17}$, Right: Pearson's r = −0.67, $p < 10^{-14}$.

3. Model 3 (brain + behavior): Bayesian Conviction and brain fMRI time-series are used to predict *confident* versus *confused*.
4. Model 4 (control 1): a simple classifier that always predicts either *confident* (1) or *confused* (0) based on the class that has more examples in the training data; i.e., if a subject was confident 70% of the time in training sessions, it will (naively) predict the subject to be *confident* at all trials in the testing set.
5. Model 5 (control 2): a slightly more sophisticated classifier that randomly assigns either 1 or 0 outcome to testing data proportional to the ratio of positive and negative examples it encounters in the training data – in the same situation from above, it would predict 70% of testing data outcomes to be 1 and 30% to be 0, with 1's and 0's randomly placed in time.

The two control models were motivated by imbalanced classes since for most subjects and sessions there were more examples of *confident* than *confused* state.

Since the fMRI data are sampled at a relatively fast rate of one data-point at each TR (0.802 seconds), but the time elapsed between successive answers (trials) varies based on the subject's decision time, which took a minimum of four TRs (mean = 8.59 ± 1.99 TRs), to convert behavioral data and outcome (Bayesian Conviction and state of mind) to the fMRI scale we make a simplistic assumption that the state of mind remains unchanged between subjects' successive picks/answers

within a session (and in-effect use all fMRI measurements between two trials to predict each trial's outcome). Alternatively, only a certain number (lag) of fMRI measurements may be averaged (by simple or weighted averaging) into one measurement that can then be used to predict each trial's behavioral outcome; i.e., instead of converting behavioral data to the fMRI time-scale by nearest neighbor interpolation, fMRI data may be down-sampled to the behavioral time-scale. Here, we present results from the fMRI time-scale, but we have found consistent results when down sampling fMRI data to behavioral scale by either averaging all the points between successive answers into one value or when averaging four points right before each answer. To account for the lag in the hemodynamic response function (HRF), we convolve all behavioral data/outcomes with canonical HRF and threshold the state of mind at 0.5 for classification purposes.

We split all available data into training and testing sets in two ways to build two types of predictive models:

1. Individual model for each subject (26 models): we use three sessions of *each* subject's data (N = 1) to train the logistic regression classifier, and the remaining session of that subject's data to make out-of-sample predictions (test); we repeat the process four times, with a different session left out for testing each time and average the performance metrics across the four runs.

2. One model for all subjects: we use three sessions of *all* subjects' data (N = 26) to train the logistic regression classifier, and the remaining session of each subject's data to make out-of-sample predictions (test); we repeat the process four times, with a different session left out for testing each time and average the performance metrics across the four runs.

It is important to note that a separate session of the game, rather than a random portion of data, is always used for testing due to intrinsic temporal dependence of data – a random split would risk leaking training data (or very close points) into the testing set. Procedure is repeated four times to avoid potential learning effects/differences between sessions biasing results – while we found no significant differences in average accuracy between the four sessions, there were significant differences in the total number of trials per session (with last session having significantly more trials compared to other sessions; paired-t test $p < 0.001$ – a difference that was a result of faster responses, rather than an overall improved accuracy).

Logistic Regression

Logistic regression is a simple classification method which may be used to produce binary predictions by using a sigmoid (logistic) function hypothesis representation $h_\theta(x) = \frac{1}{1+e^{-\theta^T x}}$, where $\theta^T x$ is a matrix notation for $\theta_0 + \theta_1 x_1 + \theta_2 x_2 + \theta_3 x_3 + \cdots + \theta_n x_n$. Logistic regression is solved by minimizing the following cost function:

$$J(\theta) = \frac{-1}{m} \sum_{i=1}^{m} [y^i \log\left(h_\theta\left(x^i\right)\right) + \left(1 - y^i\right) \log\left(1 - h_\theta\left(x^i\right)\right)]$$

where x^i denotes the i^{th} training input (feature), y^i denotes the corresponding output (class – 0 or 1), and *m* denotes the total number of training examples. We use *Scikit-learn* machine learning library in Python to implement *regularized* logistic regression, with default L2 regularization. L2 regularization adds the L2 norm penalty ($\frac{\lambda}{2m} \sum_{j=1}^{n} \theta_j^2$, where *n* denotes the number of features) to the cost function above in order to help avoid overfitting. This technique keeps all the features, but reduces the magnitudes of their coefficients. It works well when there are a lot of (potentially only) slightly useful features. An alternative would be to add the L1 norm penalty to the cost function ($\frac{\lambda}{2m} \sum_{j=1}^{n} |\theta_j|$); however, L1 regularized regression can be unstable, lead to very sparse solutions when the regularization parameter (λ) is increased, and the coefficients can vary significantly even on small data changes when there are correlated features in the data. On the other hand, L2 regularized models are more stable, less sparse, and ensure that that predictive features get non-zero coefficients and correlated features get similar coefficients. Increase in a coefficient of one feature/predictor, while keeping other features constant, may be interpreted as increase in the log-odds of class 1 relative to class 0. We perform an exhaustive grid search with cross validation within the training data to fine-tune the amount of regularization (using a wide range of *C* values: [0.001, 0.005, 0.01, 0.05, 0.1, 0.5, 1, 5, 10, 15, 100, 500, 1000, 5000, 10000], where *C* is the inverse of regularization strength). Finally, to ensure that imbalance in class sizes is not affecting model performance, we repeat both versions of analyses (individual and common model) after restricting the classification problem to classes of equal sizes in both training and testing data (each time picking all the examples from the minority class and restricting the majority class to a random subsample of matching size).

To evaluate the models, we use the following performance metrics (all calculated on testing data):

1. Accuracy – proportion of all test examples that are classified correctly
2. Precision – the number of true positives divided by the number of true positives plus the number of false positives (TP/ (TP + FP))
3. Recall – the number of true positives divided by the number of true positives plus the number of false negatives (TP/ (TP + FN))
4. F1 Score – harmonic mean of precision and recall (2 × (Precision × Recall) / (Precision + Recall))

Intuitively, precision measures the ability of the classifier not to label as positive a sample that is negative, while recall measures the ability of the classifier to find all positive samples.

Feature Selection

To elucidate the networks primarily responsible for predicting subjects' state of mind in this task, we perform feature selection to find the most important features. A simple way of doing this is by *univariate feature selection* – sequentially computing correlations between each of the input features (brain time-series) and the output on the training data and retaining only the features that have significant correlations with the output (after correction for multiple tests). We perform a very conservative pruning of features by requiring significant Pearson correlation ($p < 0.05$) between inputs and outputs on training data of each subject (for each of the four sessions used as a testing session, fully Bonferroni corrected for 27 comparisons).

Results and Discussion

Brain Data are Predictive of Subjects' State of Mind

Performance metrics show that the brain data are significantly more predictive of subjects' state of mind than what would be expected by chance (control models), and that this holds true both for the individual-subject models (**Figure 5-5**) and for the common model (**Figure 5-6**). Summary statistics for performance metrics are listed in **Table 5-2** below (averaged over 26 subjects). For individual-subject models, accuracy for model 1 (BC) was significantly greater than

for either of the control models (paired t-test $p = 1.02 \times 10^{-13}$ / $p = 8.62 \times 10^{-20}$), as was the case for model 2 (brain; paired t-test $p = 1.09 \times 10^{-12}$ / $p = 1.04 \times 10^{-20}$), and for model 3 (BC + brain; paired t-test $p = 1.35 \times 10^{-15}$ / $p = 1.92 \times 10^{-24}$). There were no significant differences in accuracy between models 1 and 2, and between models 1 and 3 ($p = 0.25$ and $p = 0.05$), while model 3 was significantly better than model 2 ($p = 7.65 \times 10^{-7}$). Similar ordering in terms of performance was observed for the common model, with very significant differences between model 2 (brain) and control models, but no significant differences between models 1 and 2. Training and testing on even classes (**Figure 5-5B** and **Figure 5-6B**) made the difference from the control model more apparent.

	Model	Accuracy	Precision	Recall	F1 Score
Individual-subject models	Bayesian Conviction	0.69 ± 0.03	0.71 ± 0.06	0.74 ± 0.03	0.72 ± 0.03
	Brain (27 IC TCs)	0.68 ± 0.03	0.73 ± 0.05	0.64 ± 0.04	0.68 ± 0.04
	Brain + Bayesian Conviction	0.70 ± 0.03	0.74 ± 0.05	0.70 ± 0.03	0.71 ± 0.03
	Control 1	0.52 ± 0.06	0.77 ± 0.32	0.41 ± 0.19	0.54 ± 0.24
	Control 2	0.50 ± 0.01	0.53 ± 0.04	0.54 ± 0.04	0.53 ± 0.04
Common Model	Bayesian Conviction	0.69 ± 0.03	0.71 ± 0.06	0.74 ± 0.04	0.72 ± 0.03
	Brain (27 IC TCs)	0.67 ± 0.03	0.72 ± 0.05	0.64 ± 0.03	0.68 ± 0.03
	Brain + Bayesian Conviction	0.70 ± 0.02	0.74 ± 0.05	0.72 ± 0.03	0.72 ± 0.02
	Control 1	0.54 ± 0.04	1	0.54 ± 0.04	0.70 ± 0.03
	Control 2	0.50 ± 0.01	0.54 ± 0.01	0.54 ± 0.04	0.53 ± 0.02

Table 5-2: Summary of performance metrics for individual-subject and common classifiers. Overall, brain-only model achieves significantly higher accuracy compared to control models, and not significantly different accuracy relative to the model including Bayesian Conviction only. Control 1 achieves precision of 1 (on the positive label) for the common model since, no matter which session is used as the testing session, when all subjects' three sessions-worth of data are concatenated, positive examples dominate, so this naïve classifier always predicts positive class. This is not the case for individual-subject models since for some subjects, depending on the testing session, there may be more negative examples. All values are averaged over four runs and N = 26 subjects, but models showed consistent results across individual subjects - for subject-level plots of performance metrics, refer to **Figure 5-5A** and **Figure 5-6A**. Number of training examples for individual models is 2214 (average number of examples of positive class is 1189), number of testing examples is 738 (average size of positive class is 396). Average number of training examples for the common model is 57564 (average number of examples of positive class is 30898), number of testing examples is 738 (average size of positive class is 396). *Precision and recall are shown for the positive label.

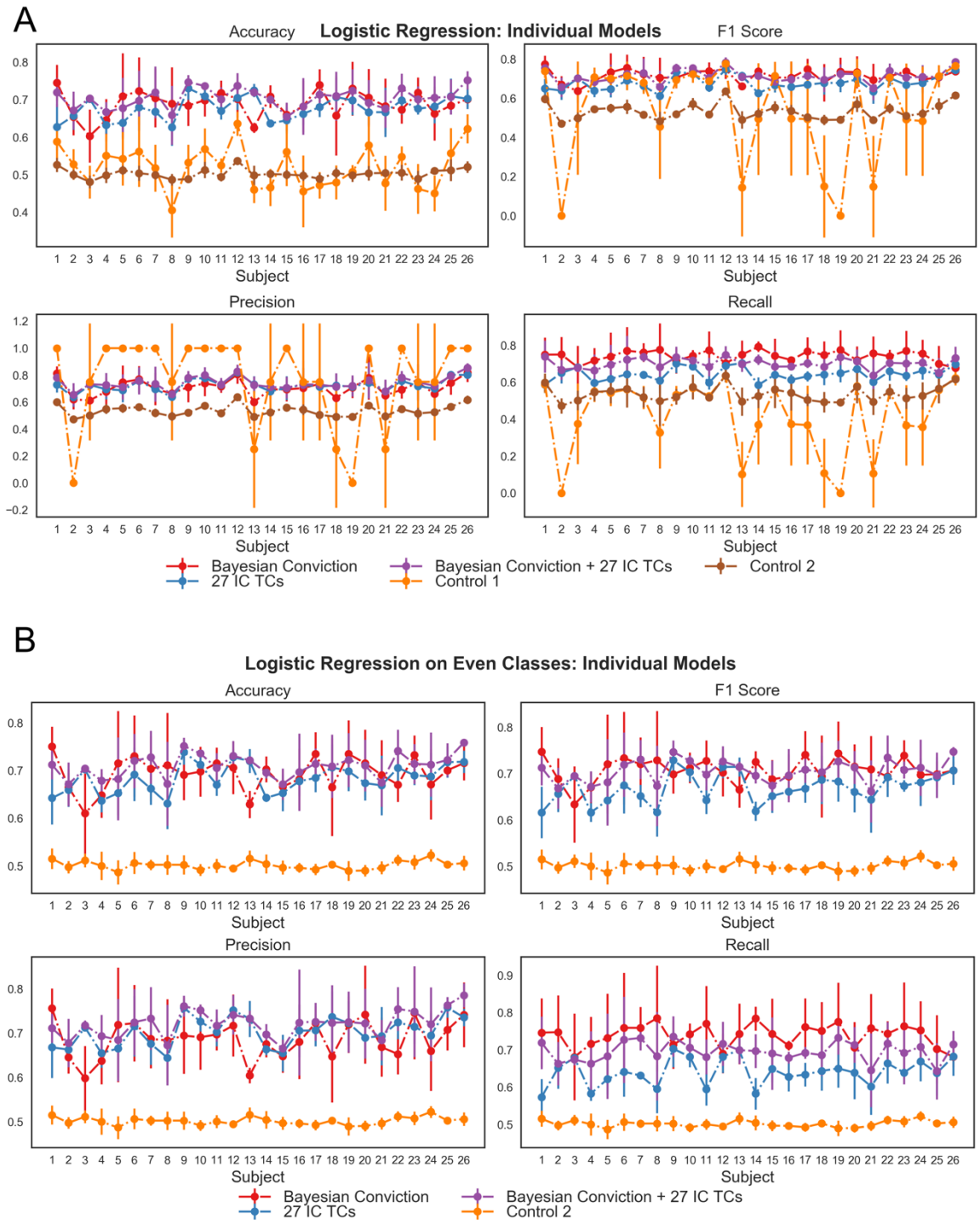

Figure 5-5: Individual-subject models predict state of mind from behavioral and brain data. Each classifier was trained on three sessions from one subject and tested on the fourth session of that subject. **(A)** Training and testing was performed on all examples. **(B)** Training and testing was performed on evenly-sized classes (a subset of majority class examples was chosen randomly to match in size the minority class. Error bars represent standard deviations across four runs (different session used for testing each time). *Precision and recall plots for the positive label are shown.

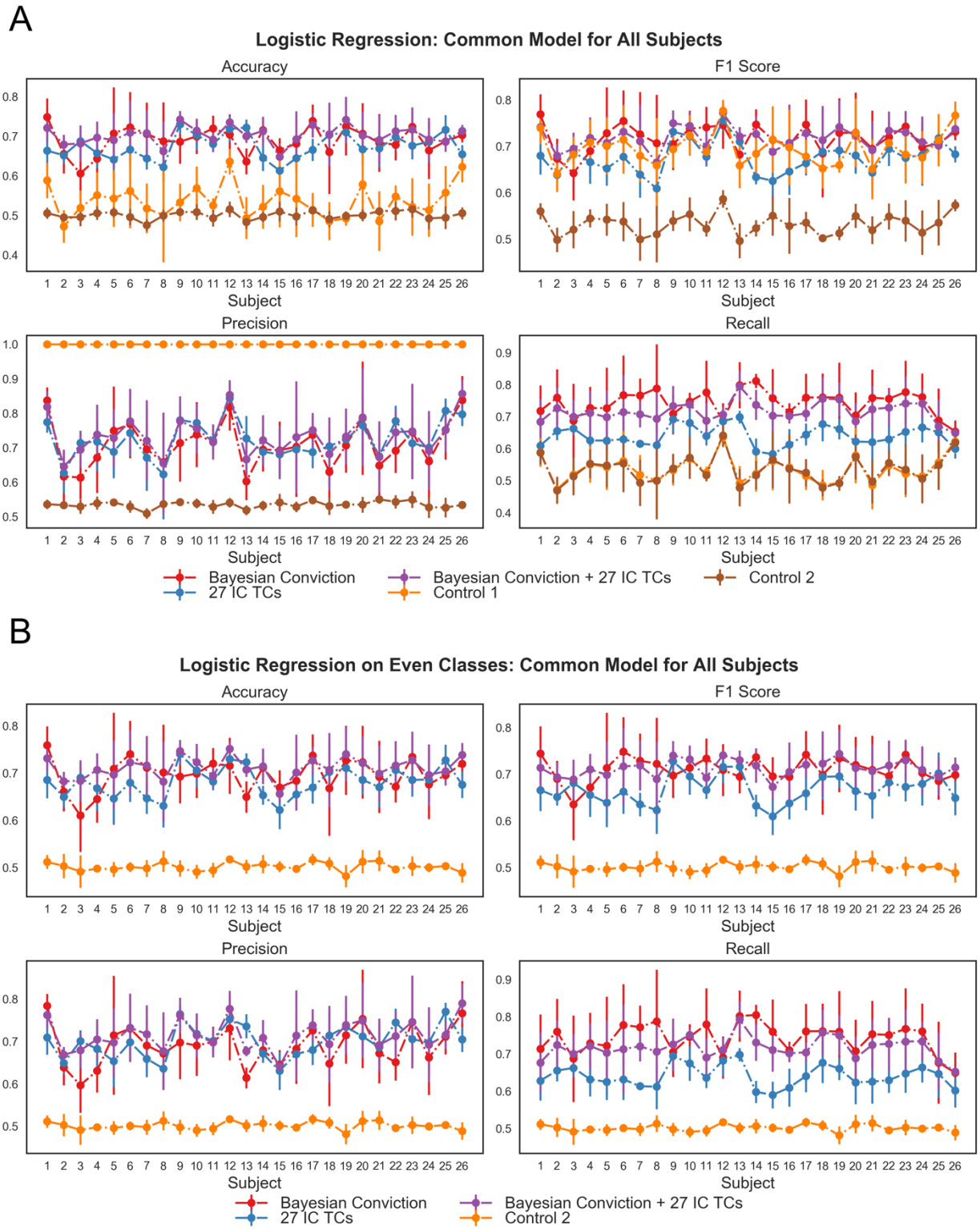

Figure 5-6: Common model predicts state of mind from behavioral and brain data. One classifier was trained on three sessions of all subjects and tested on the fourth session of each subject. **(A)** Training and testing was performed on all examples. **(B)** Training and testing was performed on evenly-sized classes. Error bars are standard deviations across four runs. *Precision and recall plots for the positive label are shown.

Feature Selection Identifies Most Informative Networks

We focus on individual models here (but equivalent analyses on the common model lead to similar results). We performed a very conservative pruning of features by requiring significant Pearson correlation ($p < 0.05$) between the inputs and outputs on training data of each subject (for each of the four sessions used as a testing session, fully Bonferroni corrected for 27 comparisons). This resulted in three independent components – 9, 11, and 17 remaining (the next in importance were components 21 and 12). See **Figure 5-7A** below for corresponding average F-values (from univariate linear regression) for all features (including Bayesian Conviction as feature #28, for reference). Spatial maps of components 9, 11, and 17 are shown in **Figure 5-7B**. IC 9 is a part of the *primary visual network*, while IC 11 and IC 17 most closely resemble the *visuospatial attention network* (lateralized to the right and to the left side, respectively), in agreement with the nature of the task.

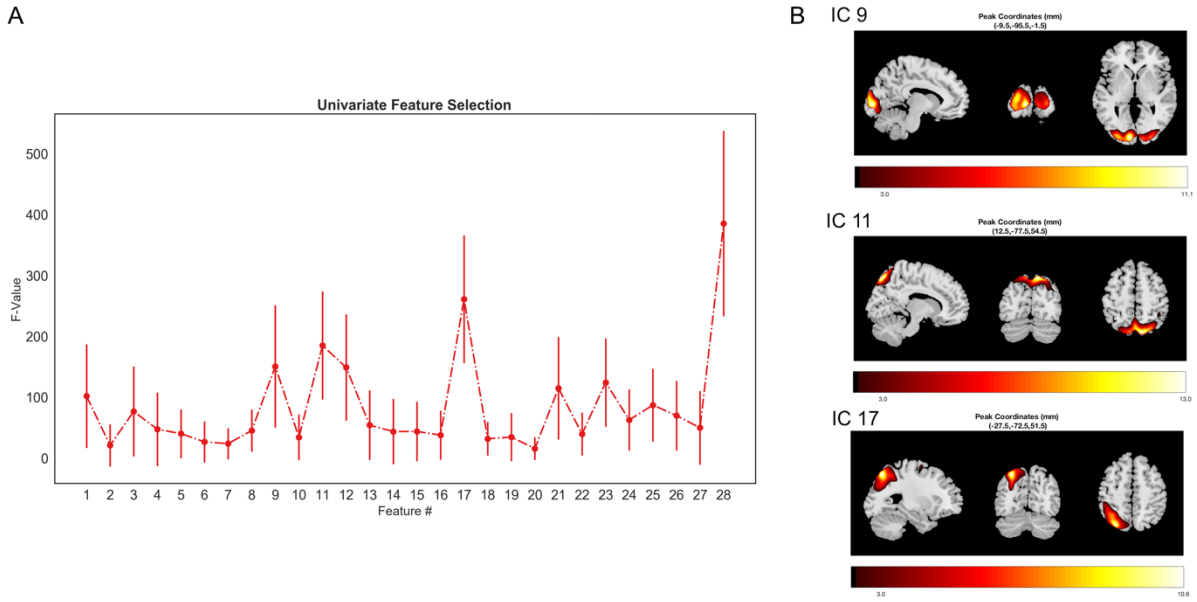

Figure 5-7:Univariate feature selection points to relative importance of features. (A) In addition to Bayesian Conviction (feature # 28) independent components 9, 11, and 17 show most significant correlations with the output. Error bars represent standard deviations across N = 26 subjects. **(B)** Spatial maps of "high-information" features.

Retraining the brain-only model with just these three features ("high-information features"), we achieve average performance close to performance achieved when utilizing all 27 features, and performance which is still significantly higher than the performance of the control model (**Figure 5-8** below, shown for both the individual models and the common model, even classes – for clarity). For further control, we also retrained the models using three features with

relatively low scores (ICs 5, 6, 7), referred to as "low-information features." As shown in **Figure 5-8,** these features resulted in a significantly lower accuracy compared to the "high-information features," but still higher accuracy compared to the control model. In all of the models, brain data alone were as predictive of subjects' state of mind as the Bayesian Conviction, and both brain alone and Bayesian Conviction alone were significantly more accurate than the control model(s).

Future Directions

The simple method presented here is a first step towards single-subject prediction of dynamic state of mind from fMRI time-series. The basic aim of showing that fMRI data are informative enough to predict human behavior/state of mind in a very complex task design has been achieved. We employed logistic regression due to its easy interpretability and could significantly reduce the number of features (brain regions under consideration) while retaining the overall accuracy by employing simple univariate feature selection. If, however, a higher accuracy is desired, more advanced machine learning techniques may be used, such as support vector machines and neural networks.

Another way to proceed would be to start with a larger set of smaller brain regions, use the methods described here to see which of them contribute to accurate predictions of state of mind, and then create more detailed circuit-level models to predict both dynamic behavioral outputs and fMRI time-series data by treating the problem as a time-series prediction problem rather than a classification problem. For example, one could use Simulink, a modeling platform built on MATLAB environment, to design, simulate, and predict dynamics of specific brain circuits and resulting behavior. Simulink can be used to model any system given the coefficients of its transfer function. Given time-varying experimental (task) inputs, BOLD signal from task-relevant nodes (e.g., those regions determined as informative using simpler techniques), and associated time-varying behavioral/state of mind outcomes, we could use transfer functions and a similar training – testing setup to build models that best describe interactions between the regions. We should, in theory, be able to predict each region's BOLD signal from experimental inputs and other regions' BOLD signal using transfer functions. All regions' predicted BOLD can then be used, in addition to experimental inputs (and, potentially, past behavior) to predict future behavior. Once an appropriate model is constructed based on real data, certain nodes and connections could

be artificially removed to simulate lesions and the consequences of such events could be quantified. In fact, by systematically removing links and nodes, we could determine which parts of the system are crucial for the observed dynamics of BOLD and behavior. Finally, input time-series can be modified to simulate disease, by, for example, altering their autocorrelation function signatures to make them more regular (as in epilepsy (Nedic et al., 2015)) or more random (as in generalized anxiety disorder (Cha et al., 2016)).

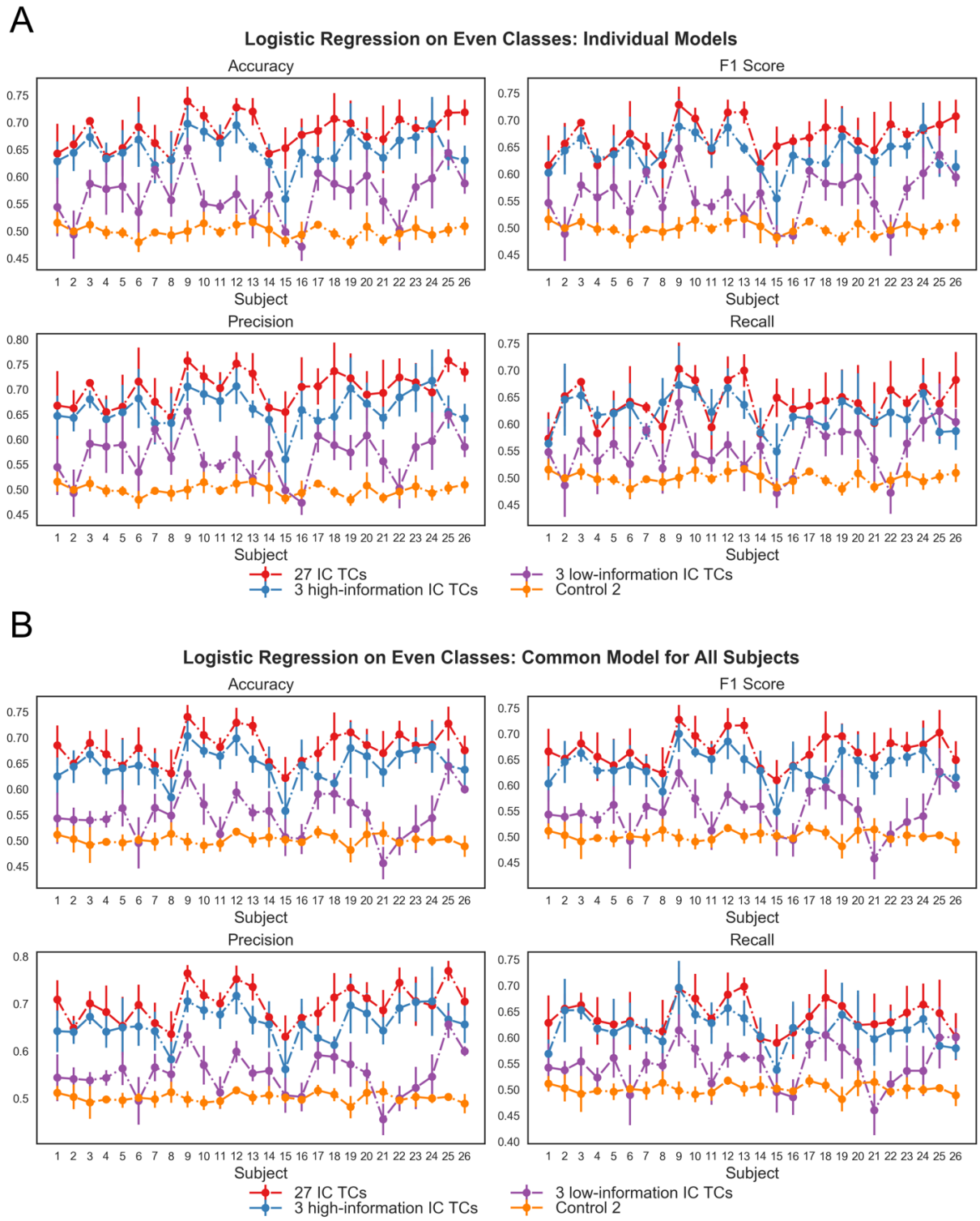

Figure 5-8: Top three independent components predict state of mind at accuracy comparable to that achieved when using all components. (A) Individual subject-level models result agrees with **(B)** common model result. Three high-information components lead to much better model performance compared to three low-information components, which in turn still do better than the control model. Error bars are standard deviations across four runs. *Precision and recall plots for the positive label are shown.

References

Achard, S., Bullmore, E., 2007. Efficiency and cost of economical brain functional networks. PLoS Comput Biol 3, e17.

Anderson, J.S., Nielsen, J.A., Ferguson, M.A., Burback, M.C., Cox, E.T., Dai, L., Gerig, G., Edgin, J.O., Korenberg, J.R., 2013. Abnormal brain synchrony in Down Syndrome. Neuroimage Clin 2, 703-715.

Anderson, J.S., Zielinski, B.A., Nielsen, J.A., Ferguson, M.A., 2014. Complexity of low-frequency blood oxygen level-dependent fluctuations covaries with local connectivity. Hum Brain Mapp 35, 1273-1283.

Assaf, B.A., Mohamed, F.B., Abou-Khaled, K.J., Williams, J.M., Yazeji, M.S., Haselgrove, J., Faro, S.H., 2003. Diffusion tensor imaging of the hippocampal formation in temporal lobe epilepsy. AJNR Am J Neuroradiol 24, 1857-1862.

Bagshaw, A.P., Aghakhani, Y., Benar, C.G., Kobayashi, E., Hawco, C., Dubeau, F., Pike, G.B., Gotman, J., 2004. EEG-fMRI of focal epileptic spikes: analysis with multiple haemodynamic functions and comparison with gadolinium-enhanced MR angiograms. Hum Brain Mapp 22, 179-192.

Bandettini, P.A., 2014. Neuronal or hemodynamic? Grappling with the functional MRI signal. Brain Connect 4, 487-498.

Bandettini, P.A., Cox, R.W., 2000. Event-related fMRI contrast when using constant interstimulus interval: theory and experiment. Magn Reson Med 43, 540-548.

Banerjee, P.N., Filippi, D., Allen Hauser, W., 2009. The descriptive epidemiology of epilepsy-a review. Epilepsy Res 85, 31-45.

Bartels, A., Zeki, S., 2005. Brain dynamics during natural viewing conditions--a new guide for mapping connectivity in vivo. Neuroimage 24, 339-349.

Bartolomei, F., Bettus, G., Stam, C.J., Guye, M., 2013. Interictal network properties in mesial temporal lobe epilepsy: a graph theoretical study from intracerebral recordings. Clin Neurophysiol 124, 2345-2353.

Bechara, A., Damasio, H., Damasio, A.R., 2000. Emotion, decision making and the orbitofrontal cortex. Cereb Cortex 10, 295-307.

Bedard, C., Destexhe, A., 2009. Macroscopic models of local field potentials and the apparent 1/f noise in brain activity. Biophys J 96, 2589-2603.

Beer, J., Blakemore, C., Previc, F.H., Liotti, M., 2002. Areas of the human brain activated by ambient visual motion, indicating three kinds of self-movement. Exp Brain Res 143, 78-88.

Bellucci, G., Chernyak, S.V., Goodyear, K., Eickhoff, S.B., Krueger, F., 2017. Neural signatures of trust in reciprocity: A coordinate-based meta-analysis. Hum Brain Mapp 38, 1233-1248.

Berg, J., Dickhaut, J., Mccabe, K., 1995. Trust, Reciprocity, and Social-History. Games and Economic Behavior 10, 122-142.

Bettus, G., Bartolomei, F., Confort-Gouny, S., Guedj, E., Chauvel, P., Cozzone, P.J., Ranjeva, J.P., Guye, M., 2010. Role of resting state functional connectivity MRI in presurgical investigation of mesial temporal lobe epilepsy. J Neurol Neurosurg Psychiatry 81, 1147-1154.

Bettus, G., Guedj, E., Joyeux, F., Confort-Gouny, S., Soulier, E., Laguitton, V., Cozzone, P.J., Chauvel, P., Ranjeva, J.P., Bartolomei, F., Guye, M., 2009. Decreased basal fMRI functional connectivity in epileptogenic networks and contralateral compensatory mechanisms. Hum Brain Mapp 30, 1580-1591.

Biswal, B., Yetkin, F.Z., Haughton, V.M., Hyde, J.S., 1995. Functional connectivity in the motor cortex of resting human brain using echo-planar MRI. Magn Reson Med 34, 537-541.

Biswal, B.B., Van Kylen, J., Hyde, J.S., 1997. Simultaneous assessment of flow and BOLD signals in resting-state functional connectivity maps. NMR Biomed 10, 165-170.

Blonder, L.X., Smith, C.D., Davis, C.E., Kesler-West, M.L., Garrity, T.F., Avison, M.J., Andersen, A.H., 2004. Regional brain response to faces of humans and dogs. Brain Res Cogn Brain Res 20, 384-394.

Bruzzo, A.A., Gesierich, B., Santi, M., Tassinari, C.A., Birbaumer, N., Rubboli, G., 2008. Permutation entropy to detect vigilance changes and preictal states from scalp EEG in epileptic patients. A preliminary study. Neurological Sciences 29, 3-9.

Bullmore, E., Sporns, O., 2009. Complex brain networks: graph theoretical analysis of structural and functional systems. Nat Rev Neurosci 10, 186-198.

Calhoun, V.D., Adali, T., Pearlson, G.D., Pekar, J.J., 2001. A method for making group inferences from functional MRI data using independent component analysis. Hum Brain Mapp 14, 140-151.

Calhoun, V.D., Kiehl, K.A., Pearlson, G.D., 2008. Modulation of temporally coherent brain networks estimated using ICA at rest and during cognitive tasks. Hum Brain Mapp 29, 828-838.

Calhoun, V.D., Pearlson, G.D., 2012. A selective review of simulated driving studies: Combining naturalistic and hybrid paradigms, analysis approaches, and future directions. Neuroimage 59, 25-35.

Calhoun, V.D., Pekar, J.J., McGinty, V.B., Adali, T., Watson, T.D., Pearlson, G.D., 2002. Different activation dynamics in multiple neural systems during simulated driving. Hum Brain Mapp 16, 158-167.

Campbell, K.L., Shafto, M.A., Wright, P., Tsvetanov, K.A., Geerligs, L., Cusack, R., Cambridge Centre for, A., Neuroscience, Tyler, L.K., 2015. Idiosyncratic responding during movie-watching predicted by age differences in attentional control. Neurobiol Aging 36, 3045-3055.

Carlson, J.M., Rubin, D., Mujica-Parodi, L.R., 2016. Lost emotion: Disrupted brain-based tracking of dynamic affective episodes in anxiety and depression. Psychiatry Res 260, 37-48.

Cha, J., DeDora, D., Nedic, S., Ide, J., Greenberg, T., Hajcak, G., Mujica-Parodi, L.R., 2016. Clinically Anxious Individuals Show Disrupted Feedback between Inferior Frontal Gyrus and Prefrontal-Limbic Control Circuit. J Neurosci 36, 4708-4718.

Clauset, A., Shalizi, C.R., Newman, M.E.J., 2009. Power-Law Distributions in Empirical Data. Siam Review 51, 661-703.

Cong, F., Puolivali, T., Alluri, V., Sipola, T., Burunat, I., Toiviainen, P., Nandi, A.K., Brattico, E., Ristaniemi, T., 2014. Key issues in decomposing fMRI during naturalistic and continuous music experience with independent component analysis. J Neurosci Methods 223, 74-84.

Coste, S., Ryvlin, P., Hermier, M., Ostrowsky, K., Adeleine, P., Froment, J.C., Mauguiere, F., 2002. Temporopolar changes in temporal lobe epilepsy: a quantitative MRI-based study. Neurology 59, 855-861.

Damoiseaux, J.S., Beckmann, C.F., Arigita, E.J., Barkhof, F., Scheltens, P., Stam, C.J., Smith, S.M., Rombouts, S.A., 2008. Reduced resting-state brain activity in the "default network" in normal aging. Cereb Cortex 18, 1856-1864.

DeDora, D.J., Nedic, S., Katti, P., Arnab, S., Wald, L.L., Takahashi, A., Van Dijk, K.R., Strey, H.H., Mujica-Parodi, L.R., 2016. Signal Fluctuation Sensitivity: An Improved Metric for Optimizing Detection of Resting-State fMRI Networks. Front Neurosci 10, 180.

Dricu, M., Fruhholz, S., 2016. Perceiving emotional expressions in others: Activation likelihood estimation meta-analyses of explicit evaluation, passive perception and incidental perception of emotions. Neurosci Biobehav Rev 71, 810-828.

Elshoff, L., Groening, K., Grouiller, F., Wiegand, G., Wolff, S., Michel, C., Stephani, U., Siniatchkin, M., 2012. The value of EEG-fMRI and EEG source analysis in the presurgical setup of children with refractory focal epilepsy. Epilepsia 53, 1597-1606.

Erhardt, E.B., Rachakonda, S., Bedrick, E.J., Allen, E.A., Adali, T., Calhoun, V.D., 2011. Comparison of multi-subject ICA methods for analysis of fMRI data. Hum Brain Mapp 32, 2075-2095.

Focke, N.K., Yogarajah, M., Bonelli, S.B., Bartlett, P.A., Symms, M.R., Duncan, J.S., 2008. Voxel-based diffusion tensor imaging in patients with mesial temporal lobe epilepsy and hippocampal sclerosis. Neuroimage 40, 728-737.

Fox, M.D., Snyder, A.Z., Vincent, J.L., Corbetta, M., Van Essen, D.C., Raichle, M.E., 2005. The human brain is intrinsically organized into dynamic, anticorrelated functional networks. Proc Natl Acad Sci U S A 102, 9673-9678.

Freyer, F., Aquino, K., Robinson, P.A., Ritter, P., Breakspear, M., 2009. Bistability and non-Gaussian fluctuations in spontaneous cortical activity. J Neurosci 29, 8512-8524.

Friston, K.J., Holmes, A.P., Poline, J.B., Grasby, P.J., Williams, S.C., Frackowiak, R.S., Turner, R., 1995. Analysis of fMRI time-series revisited. Neuroimage 2, 45-53.

Gaebler, M., Biessmann, F., Lamke, J.P., Muller, K.R., Walter, H., Hetzer, S., 2014. Stereoscopic depth increases intersubject correlations of brain networks. Neuroimage 100, 427-434.

Gawryluk, J.R., Mazerolle, E.L., D'Arcy, R.C., 2014. Does functional MRI detect activation in white matter? A review of emerging evidence, issues, and future directions. Front Neurosci 8, 239.

Gonzalez-Castillo, J., Handwerker, D.A., Robinson, M.E., Hoy, C.W., Buchanan, L.C., Saad, Z.S., Bandettini, P.A., 2014. The spatial structure of resting state connectivity stability on the scale of minutes. Front Neurosci 8, 138.

Greicius, M.D., Flores, B.H., Menon, V., Glover, G.H., Solvason, H.B., Kenna, H., Reiss, A.L., Schatzberg, A.F., 2007. Resting-state functional connectivity in major depression: abnormally increased contributions from subgenual cingulate cortex and thalamus. Biol Psychiatry 62, 429-437.

Greicius, M.D., Krasnow, B., Reiss, A.L., Menon, V., 2003. Functional connectivity in the resting brain: a network analysis of the default mode hypothesis. Proc Natl Acad Sci U S A 100, 253-258.

Grouiller, F., Delattre, B.M., Pittau, F., Heinzer, S., Lazeyras, F., Spinelli, L., Iannotti, G.R., Seeck, M., Ratib, O., Vargas, M.I., Garibotto, V., Vulliemoz, S., 2015. All-in-one interictal

presurgical imaging in patients with epilepsy: single-session EEG/PET/(f)MRI. Eur J Nucl Med Mol Imaging 42, 1133-1143.

Grouiller, F., Thornton, R.C., Groening, K., Spinelli, L., Duncan, J.S., Schaller, K., Siniatchkin, M., Lemieux, L., Seeck, M., Michel, C.M., Vulliemoz, S., 2011. With or without spikes: localization of focal epileptic activity by simultaneous electroencephalography and functional magnetic resonance imaging. Brain 134, 2867-2886.

Guderian, S., Dzieciol, A.M., Gadian, D.G., Jentschke, S., Doeller, C.F., Burgess, N., Mishkin, M., Vargha-Khadem, F., 2015. Hippocampal Volume Reduction in Humans Predicts Impaired Allocentric Spatial Memory in Virtual-Reality Navigation. J Neurosci 35, 14123-14131.

Guo, C.C., Nguyen, V.T., Hyett, M.P., Parker, G.B., Breakspear, M.J., 2015. Out-of-sync: disrupted neural activity in emotional circuitry during film viewing in melancholic depression. Sci Rep 5, 11605.

Han, Y., Wang, J., Zhao, Z., Min, B., Lu, J., Li, K., He, Y., Jia, J., 2011. Frequency-dependent changes in the amplitude of low-frequency fluctuations in amnestic mild cognitive impairment: a resting-state fMRI study. Neuroimage 55, 287-295.

Hasson, U., Avidan, G., Gelbard, H., Vallines, I., Harel, M., Minshew, N., Behrmann, M., 2009. Shared and idiosyncratic cortical activation patterns in autism revealed under continuous real-life viewing conditions. Autism Res 2, 220-231.

Hasson, U., Malach, R., Heeger, D.J., 2010. Reliability of cortical activity during natural stimulation. Trends Cogn Sci 14, 40-48.

Hasson, U., Nir, Y., Levy, I., Fuhrmann, G., Malach, R., 2004. Intersubject synchronization of cortical activity during natural vision. Science 303, 1634-1640.

He, B.J., 2011. Scale-free properties of the functional magnetic resonance imaging signal during rest and task. J Neurosci 31, 13786-13795.

He, B.J., Raichle, M.E., 2009. The fMRI signal, slow cortical potential and consciousness. Trends Cogn Sci 13, 302-309.

Helmstaedter, C., Kurthen, M., Lux, S., Reuber, M., Elger, C.E., 2003. Chronic epilepsy and cognition: a longitudinal study in temporal lobe epilepsy. Ann Neurol 54, 425-432.

Helmstaedter, C., Wietzke, J., Lutz, M.T., 2009. Unique and shared validity of the "Wechsler logical memory test", the "California verbal learning test", and the "verbal learning and memory test" in patients with epilepsy. Epilepsy Res 87, 203-212.

Himberg, J., Hyvarinen, A., Esposito, F., 2004. Validating the independent components of neuroimaging time series via clustering and visualization. Neuroimage 22, 1214-1222.

Hogan, R.E., Kaiboriboon, K., Bertrand, M.E., Rao, V., Acharya, J., 2006. Composite SISCOM perfusion patterns in right and left temporal seizures. Arch Neurol 63, 1419-1426.

Horstmann, M.T., Bialonski, S., Noennig, N., Mai, H., Prusseit, J., Wellmer, J., Hinrichs, H., Lehnertz, K., 2010. State dependent properties of epileptic brain networks: comparative graph-theoretical analyses of simultaneously recorded EEG and MEG. Clin Neurophysiol 121, 172-185.

Hsu, D., Tang, A., Hsu, M., Beggs, J.M., 2007. Simple spontaneously active Hebbian learning model: homeostasis of activity and connectivity, and consequences for learning and epileptogenesis. Phys Rev E Stat Nonlin Soft Matter Phys 76, 041909.

Iidaka, T., 2016. Humor Appreciation Involves Parametric and Synchronized Activity in the Medial Prefrontal Cortex and Hippocampus. Cereb Cortex.

James, G.A., Tripathi, S.P., Ojemann, J.G., Gross, R.E., Drane, D.L., 2013. Diminished default mode network recruitment of the hippocampus and parahippocampus in temporal lobe epilepsy. J Neurosurg 119, 288-300.

Johansen-Berg, H., Behrens, T.E., Sillery, E., Ciccarelli, O., Thompson, A.J., Smith, S.M., Matthews, P.M., 2005. Functional-anatomical validation and individual variation of diffusion tractography-based segmentation of the human thalamus. Cereb Cortex 15, 31-39.

Kaplan, R., Horner, A.J., Bandettini, P.A., Doeller, C.F., Burgess, N., 2014. Human hippocampal processing of environmental novelty during spatial navigation. Hippocampus 24, 740-750.

Kellenbach, M.L., Hovius, M., Patterson, K., 2005. A pet study of visual and semantic knowledge about objects. Cortex 41, 121-132.

King-Casas, B., Tomlin, D., Anen, C., Camerer, C.F., Quartz, S.R., Montague, P.R., 2005. Getting to know you: reputation and trust in a two-person economic exchange. Science 308, 78-83.

Klamer, S., Rona, S., Elshahabi, A., Lerche, H., Braun, C., Honegger, J., Erb, M., Focke, N.K., 2015. Multimodal effective connectivity analysis reveals seizure focus and propagation in musicogenic epilepsy. Neuroimage 113, 70-77.

Kringelbach, M.L., 2005. The human orbitofrontal cortex: linking reward to hedonic experience. Nat Rev Neurosci 6, 691-702.

Kruger, G., Kastrup, A., Glover, G.H., 2001. Neuroimaging at 1.5 T and 3.0 T: comparison of oxygenation-sensitive magnetic resonance imaging. Magn Reson Med 45, 595-604.

Kwan, P., Brodie, M.J., 2000. Early identification of refractory epilepsy. N Engl J Med 342, 314-319.

Labate, A., Cerasa, A., Aguglia, U., Mumoli, L., Quattrone, A., Gambardella, A., 2011. Neocortical thinning in "benign" mesial temporal lobe epilepsy. Epilepsia 52, 712-717.

Lai, M.C., Lombardo, M.V., Chakrabarti, B., Sadek, S.A., Pasco, G., Wheelwright, S.J., Bullmore, E.T., Baron-Cohen, S., Suckling, J., 2010. A shift to randomness of brain oscillations in people with autism. Biol Psychiatry 68, 1092-1099.

Latora, V., Marchiori, M., 2001. Efficient behavior of small-world networks. Physical Review Letters 87, 198701.

Lehnertz, K., Bialonski, S., Horstmann, M.T., Krug, D., Rothkegel, A., Staniek, M., Wagner, T., 2009. Synchronization phenomena in human epileptic brain networks. J Neurosci Methods 183, 42-48.

Levina, A., Herrmann, J.M., Geisel, T., 2007. Dynamical synapses causing self-organized criticality in neural networks. Nature Physics 3, 857-860.

Li, Y.O., Adali, T., Calhoun, V.D., 2007. Estimating the number of independent components for functional magnetic resonance imaging data. Hum Brain Mapp 28, 1251-1266.

Liao, W., Zhang, Z., Pan, Z., Mantini, D., Ding, J., Duan, X., Luo, C., Lu, G., Chen, H., 2010. Altered functional connectivity and small-world in mesial temporal lobe epilepsy. PLoS One 5, e8525.

Liao, W., Zhang, Z., Pan, Z., Mantini, D., Ding, J., Duan, X., Luo, C., Wang, Z., Tan, Q., Lu, G., Chen, H., 2011. Default mode network abnormalities in mesial temporal lobe epilepsy: a study combining fMRI and DTI. Hum Brain Mapp 32, 883-895.

Liu, Y., Wang, K., Yu, C., He, Y., Zhou, Y., Liang, M., Wang, L., Jiang, T., 2008. Regional homogeneity, functional connectivity and imaging markers of Alzheimer's disease: a review of resting-state fMRI studies. Neuropsychologia 46, 1648-1656.

Logothetis, N.K., Eschenko, O., Murayama, Y., Augath, M., Steudel, T., Evrard, H.C., Besserve, M., Oeltermann, A., 2012. Hippocampal-cortical interaction during periods of subcortical silence. Nature 491, 547-553.

Lowen, S.B., Cash, S.S., Poo, M., Teich, M.C., 1997. Quantal neurotransmitter secretion rate exhibits fractal behavior. J Neurosci 17, 5666-5677.

Maccotta, L., He, B.J., Snyder, A.Z., Eisenman, L.N., Benzinger, T.L., Ances, B.M., Corbetta, M., Hogan, R.E., 2013. Impaired and facilitated functional networks in temporal lobe epilepsy. Neuroimage Clin 2, 862-872.

Maddock, R.J., Garrett, A.S., Buonocore, M.H., 2001. Remembering familiar people: the posterior cingulate cortex and autobiographical memory retrieval. Neuroscience 104, 667-676.

Malinen, S., Hlushchuk, Y., Hari, R., 2007. Towards natural stimulation in fMRI--issues of data analysis. Neuroimage 35, 131-139.

Maneshi, M., Vahdat, S., Fahoum, F., Grova, C., Gotman, J., 2014. Specific resting-state brain networks in mesial temporal lobe epilepsy. Front Neurol 5, 127.

Maxim, V., Sendur, L., Fadili, J., Suckling, J., Gould, R., Howard, R., Bullmore, E., 2005. Fractional Gaussian noise, functional MRI and Alzheimer's disease. Neuroimage 25, 141-158.

Mayer, A.R., Mannell, M.V., Ling, J., Gasparovic, C., Yeo, R.A., 2011. Functional connectivity in mild traumatic brain injury. Hum Brain Mapp 32, 1825-1835.

Miezin, F.M., Maccotta, L., Ollinger, J.M., Petersen, S.E., Buckner, R.L., 2000. Characterizing the hemodynamic response: effects of presentation rate, sampling procedure, and the possibility of ordering brain activity based on relative timing. Neuroimage 11, 735-759.

Mirz, F., Ovesen, T., Ishizu, K., Johannsen, P., Madsen, S., Gjedde, A., Pedersen, C.B., 1999. Stimulus-dependent central processing of auditory stimuli: a PET study. Scand Audiol 28, 161-169.

Molloy, E.K., Meyerand, M.E., Birn, R.M., 2014. The influence of spatial resolution and smoothing on the detectability of resting-state and task fMRI. Neuroimage 86, 221-230.

Molteni, E., Perego, P., Zanotta, N., Reni, G., 2008. Entropy analysis on EEG signal in a case study of focal myoclonus. 2008 30th Annual International Conference of the IEEE Engineering in Medicine and Biology Society, Vols 1-8, 4724-4727.

Monto, S., Vanhatalo, S., Holmes, M.D., Palva, J.M., 2007. Epileptogenic neocortical networks are revealed by abnormal temporal dynamics in seizure-free subdural EEG. Cereb Cortex 17, 1386-1393.

Morgan, V.L., Rogers, B.P., Sonmezturk, H.H., Gore, J.C., Abou-Khalil, B., 2011. Cross hippocampal influence in mesial temporal lobe epilepsy measured with high temporal resolution functional magnetic resonance imaging. Epilepsia 52, 1741-1749.

Murphy, K., Bodurka, J., Bandettini, P.A., 2007. How long to scan? The relationship between fMRI temporal signal to noise ratio and necessary scan duration. Neuroimage 34, 565-574.

Nedic, S., Mujica-Parodi, L., 2017. Signal Fluctuation Sensitivity Identifies Brain Activity in Naturalistic-Task fMRI. under review.

Nedic, S., Stufflebeam, S.M., Rondinoni, C., Velasco, T.R., dos Santos, A.C., Leite, J.P., Gargaro, A.C., Mujica-Parodi, L.R., Ide, J.S., 2015. Using network dynamic fMRI for detection of epileptogenic foci. BMC Neurol 15, 262.

Nummenmaa, L., Glerean, E., Viinikainen, M., Jaaskelainen, I.P., Hari, R., Sams, M., 2012. Emotions promote social interaction by synchronizing brain activity across individuals. Proc Natl Acad Sci U S A 109, 9599-9604.

Oren, N., Shapira-Lichter, I., Lerner, Y., Tarrasch, R., Hendler, T., Giladi, N., Ash, E.L., 2016. How Attention Modulates Encoding of Dynamic Stimuli. Front Hum Neurosci 10, 507.

Pereira, F.R., Alessio, A., Sercheli, M.S., Pedro, T., Bilevicius, E., Rondina, J.M., Ozelo, H.F., Castellano, G., Covolan, R.J., Damasceno, B.P., Cendes, F., 2010. Asymmetrical hippocampal connectivity in mesial temporal lobe epilepsy: evidence from resting state fMRI. BMC Neurosci 11, 66.

Pittau, F., Grova, C., Moeller, F., Dubeau, F., Gotman, J., 2012. Patterns of altered functional connectivity in mesial temporal lobe epilepsy. Epilepsia 53, 1013-1023.

Power, J.D., Barnes, K.A., Snyder, A.Z., Schlaggar, B.L., Petersen, S.E., 2012. Spurious but systematic correlations in functional connectivity MRI networks arise from subject motion. Neuroimage 59, 2142-2154.

Protzner, A.B., Valiante, T.A., Kovacevic, N., McCormick, C., McAndrews, M.P., 2010. Hippocampal signal complexity in mesial temporal lobe epilepsy: a noisy brain is a healthy brain. Arch Ital Biol 148, 289-297.

Radulescu, A., Mujica-Parodi, L.R., 2014. Network connectivity modulates power spectrum scale invariance. Neuroimage 90, 436-448.

Radulescu, A.R., Rubin, D., Strey, H.H., Mujica-Parodi, L.R., 2012. Power spectrum scale invariance identifies prefrontal dysregulation in paranoid schizophrenia. Hum Brain Mapp 33, 1582-1593.

Raichle, M.E., 2015. The Brain's Default Mode Network. Annu Rev Neurosci 38, 433-447.

Raichle, M.E., MacLeod, A.M., Snyder, A.Z., Powers, W.J., Gusnard, D.A., Shulman, G.L., 2001. A default mode of brain function. Proc Natl Acad Sci U S A 98, 676-682.

Rigoux, L., Daunizeau, J., 2015. Dynamic causal modelling of brain-behaviour relationships. Neuroimage 117, 202-221.

Roseman, L., Leech, R., Feilding, A., Nutt, D.J., Carhart-Harris, R.L., 2014. The effects of psilocybin and MDMA on between-network resting state functional connectivity in healthy volunteers. Front Hum Neurosci 8, 204.

Rosen, B.R., Savoy, R.L., 2012. fMRI at 20: has it changed the world? Neuroimage 62, 1316-1324.

Rubinov, M., Sporns, O., Thivierge, J.P., Breakspear, M., 2011. Neurobiologically realistic determinants of self-organized criticality in networks of spiking neurons. PLoS Comput Biol 7, e1002038.

Salmi, J., Roine, U., Glerean, E., Lahnakoski, J., Nieminen-von Wendt, T., Tani, P., Leppamaki, S., Nummenmaa, L., Jaaskelainen, I.P., Carlson, S., Rintahaka, P., Sams, M., 2013. The brains of high functioning autistic individuals do not synchronize with those of others. Neuroimage Clin 3, 489-497.

Salvador, R., Suckling, J., Coleman, M.R., Pickard, J.D., Menon, D., Bullmore, E., 2005. Neurophysiological architecture of functional magnetic resonance images of human brain. Cereb Cortex 15, 1332-1342.

Schrouff, J., Rosa, M.J., Rondina, J.M., Marquand, A.F., Chu, C., Ashburner, J., Phillips, C., Richiardi, J., Mourao-Miranda, J., 2013. PRoNTo: pattern recognition for neuroimaging toolbox. Neuroinformatics 11, 319-337.

Slotnick, S.D., Schacter, D.L., 2004. A sensory signature that distinguishes true from false memories. Nat Neurosci 7, 664-672.

Smith, S.M., Beckmann, C.F., Andersson, J., Auerbach, E.J., Bijsterbosch, J., Douaud, G., Duff, E., Feinberg, D.A., Griffanti, L., Harms, M.P., Kelly, M., Laumann, T., Miller, K.L., Moeller, S., Petersen, S., Power, J., Salimi-Khorshidi, G., Snyder, A.Z., Vu, A.T., Woolrich, M.W., Xu, J., Yacoub, E., Ugurbil, K., Van Essen, D.C., Glasser, M.F., Consortium, W.U.-M.H., 2013. Resting-state fMRI in the Human Connectome Project. Neuroimage 80, 144-168.

Smith, S.M., Fox, P.T., Miller, K.L., Glahn, D.C., Fox, P.M., Mackay, C.E., Filippini, N., Watkins, K.E., Toro, R., Laird, A.R., Beckmann, C.F., 2009. Correspondence of the brain's functional architecture during activation and rest. Proc Natl Acad Sci U S A 106, 13040-13045.

Soble, J.R., Eichstaedt, K.E., Waseem, H., Mattingly, M.L., Benbadis, S.R., Bozorg, A.M., Vale, F.L., Schoenberg, M.R., 2014. Clinical utility of the Wechsler Memory Scale--Fourth Edition (WMS-IV) in predicting laterality of temporal lobe epilepsy among surgical candidates. Epilepsy Behav 41, 232-237.

Song, X.W., Dong, Z.Y., Long, X.Y., Li, S.F., Zuo, X.N., Zhu, C.Z., He, Y., Yan, C.G., Zang, Y.F., 2011. REST: a toolkit for resting-state functional magnetic resonance imaging data processing. PLoS One 6, e25031.

Spiers, H.J., Maguire, E.A., 2006. Thoughts, behaviour, and brain dynamics during navigation in the real world. Neuroimage 31, 1826-1840.

Spiers, H.J., Maguire, E.A., 2007. Decoding human brain activity during real-world experiences. Trends Cogn Sci 11, 356-365.

Stam, C.J., 2014. Modern network science of neurological disorders. Nat Rev Neurosci 15, 683-695.

Stufflebeam, S.M., Liu, H., Sepulcre, J., Tanaka, N., Buckner, R.L., Madsen, J.R., 2011. Localization of focal epileptic discharges using functional connectivity magnetic resonance imaging. J Neurosurg 114, 1693-1697.

Tebartz van Elst, L., Krishnamoorthy, E.S., Schulze-Bonhage, A., Altenmuller, D.M., Richter, H., Ebert, D., Feige, B., 2011. Local area network inhibition: a model of a potentially important paraepileptic pathomechanism in neuropsychiatric disorders. Epilepsy Behav 22, 231-239.

Tellez-Zenteno, J.F., Dhar, R., Wiebe, S., 2005. Long-term seizure outcomes following epilepsy surgery: a systematic review and meta-analysis. Brain 128, 1188-1198.

Tolkunov, D., Rubin, D., Mujica-Parodi, L., 2010. Power spectrum scale invariance quantifies limbic dysregulation in trait anxious adults using fMRI: adapting methods optimized for characterizing autonomic dysregulation to neural dynamic time series. Neuroimage 50, 72-80.

Tracy, J.I., Doucet, G.E., 2015. Resting-state functional connectivity in epilepsy: growing relevance for clinical decision making. Curr Opin Neurol 28, 158-165.

Triantafyllou, C., Hoge, R.D., Krueger, G., Wiggins, C.J., Potthast, A., Wiggins, G.C., Wald, L.L., 2005. Comparison of physiological noise at 1.5 T, 3 T and 7 T and optimization of fMRI acquisition parameters. Neuroimage 26, 243-250.

Trost, W., Fruhholz, S., Cochrane, T., Cojan, Y., Vuilleumier, P., 2015. Temporal dynamics of musical emotions examined through intersubject synchrony of brain activity. Soc Cogn Affect Neurosci 10, 1705-1721.

van den Heuvel, M.P., Hulshoff Pol, H.E., 2010. Exploring the brain network: a review on resting-state fMRI functional connectivity. Eur Neuropsychopharmacol 20, 519-534.

van den Heuvel, M.P., Sporns, O., 2011. Rich-club organization of the human connectome. J Neurosci 31, 15775-15786.

van den Heuvel, M.P., Stam, C.J., Boersma, M., Hulshoff Pol, H.E., 2008. Small-world and scale-free organization of voxel-based resting-state functional connectivity in the human brain. Neuroimage 43, 528-539.

Van Dijk, K.R., Sabuncu, M.R., Buckner, R.L., 2012. The influence of head motion on intrinsic functional connectivity MRI. Neuroimage 59, 431-438.

van Wijk, B.C., Stam, C.J., Daffertshofer, A., 2010. Comparing brain networks of different size and connectivity density using graph theory. PLoS One 5, e13701.

Vaudano, A.E., Avanzini, P., Tassi, L., Ruggieri, A., Cantalupo, G., Benuzzi, F., Nichelli, P., Lemieux, L., Meletti, S., 2013. Causality within the Epileptic Network: An EEG-fMRI Study Validated by Intracranial EEG. Front Neurol 4, 185.

Wald, L.L., 2012. The future of acquisition speed, coverage, sensitivity, and resolution. Neuroimage 62, 1221-1229.

Wang, J., Ren, Y., Hu, X., Nguyen, V.T., Guo, L., Han, J., Guo, C.C., 2017. Test-retest reliability of functional connectivity networks during naturalistic fMRI paradigms. Hum Brain Mapp.

Wechsler, D., 1987. Wechsler Memory Scale—Revised manual. San Antonio, TX: Psychological Corporation.

Wellmer, J., von der Groeben, F., Klarmann, U., Weber, C., Elger, C.E., Urbach, H., Clusmann, H., von Lehe, M., 2012. Risks and benefits of invasive epilepsy surgery workup with implanted subdural and depth electrodes. Epilepsia 53, 1322-1332.

Welvaert, M., Rosseel, Y., 2013. On the definition of signal-to-noise ratio and contrast-to-noise ratio for FMRI data. PLoS One 8, e77089.

Wilczynski, G.M., Konopacki, F.A., Wilczek, E., Lasiecka, Z., Gorlewicz, A., Michaluk, P., Wawrzyniak, M., Malinowska, M., Okulski, P., Kolodziej, L.R., Konopka, W., Duniec, K., Mioduszewska, B., Nikolaev, E., Walczak, A., Owczarek, D., Gorecki, D.C., Zuschratter, W., Ottersen, O.P., Kaczmarek, L., 2008. Important role of matrix metalloproteinase 9 in epileptogenesis. J Cell Biol 180, 1021-1035.

Wu, T., Long, X., Zang, Y., Wang, L., Hallett, M., Li, K., Chan, P., 2009. Regional homogeneity changes in patients with Parkinson's disease. Hum Brain Mapp 30, 1502-1510.

Yang, H., Long, X.Y., Yang, Y., Yan, H., Zhu, C.Z., Zhou, X.P., Zang, Y.F., Gong, Q.Y., 2007. Amplitude of low frequency fluctuation within visual areas revealed by resting-state functional MRI. Neuroimage 36, 144-152.

Ylipaavalniemi, J., Savia, E., Malinen, S., Hari, R., Vigario, R., Kaski, S., 2009. Dependencies between stimuli and spatially independent fMRI sources: towards brain correlates of natural stimuli. Neuroimage 48, 176-185.

Zang, Y., Jiang, T., Lu, Y., He, Y., Tian, L., 2004. Regional homogeneity approach to fMRI data analysis. Neuroimage 22, 394-400.

Zang, Y.-F., He, Y., Zhu, C.-Z., Cao, Q.-J., Sui, M.-Q., Liang, M., Tian, L.-X., Jiang, T.-Z., Wang, Y.-F., 2007. Altered baseline brain activity in children with ADHD revealed by resting-state functional MRI. Brain and Development 29, 83-91.

Zeng, H., Pizarro, R., Nair, V.A., La, C., Prabhakaran, V., 2013. Alterations in regional homogeneity of resting-state brain activity in mesial temporal lobe epilepsy. Epilepsia 54, 658-666.

Zhang, Z., Lu, G., Zhong, Y., Tan, Q., Liao, W., Chen, Z., Shi, J., Liu, Y., 2009. Impaired perceptual networks in temporal lobe epilepsy revealed by resting fMRI. J Neurol 256, 1705-1713.

Zhang, Z., Lu, G., Zhong, Y., Tan, Q., Liao, W., Wang, Z., Li, K., Chen, H., Liu, Y., 2010. Altered spontaneous neuronal activity of the default-mode network in mesial temporal lobe epilepsy. Brain Res 1323, 152-160.

Zou, Q.H., Zhu, C.Z., Yang, Y., Zuo, X.N., Long, X.Y., Cao, Q.J., Wang, Y.F., Zang, Y.F., 2008. An improved approach to detection of amplitude of low-frequency fluctuation (ALFF) for resting-state fMRI: fractional ALFF. J Neurosci Methods 172, 137-141.